Search for Atmospheric Neutrino Non-Standard Interaction in NOvA and DUNE

by
Muyuan He

A dissertation submitted to the Department of Physics,
College of Natural Sciences and Mathematics
in partial fulfillment of the requirements for the degree of

Doctor of Philosophy
in Physics

Chair of Committee: Lisa W. Koerner

Committee Member: Daniel Cherdack

Committee Member: Ioannis Pavlidis

Committee Member: Claudia Ratti

University of Houston
December 2025

DEDICATION/EPILOGUE

For Ou, Ziye and my dog Ariel

ACKNOWLEDGMENTS

I am profoundly grateful to my advisor, Dr. Lisa Whitehead Koerner, for her unwavering support throughout my doctoral journey. She has been more than an exceptional mentor - She has been a dream advisor to work with. Lisa consistently championed my ideas, built bridges that opened countless opportunities, and made the seemingly impossible possible. I could not have asked for a more supportive advisor, and I am deeply thankful for everything she has done to help me succeed.

This material is based upon work supported by the U.S. Department of Energy, Office of Science, Office of High Energy Physics under Award Number DE-SC-0021407.

I would like to thank my dissertation committee members for their guidance and support. I am especially grateful to Dr. Daniel Cherdack, whose expertise in detailed analysis techniques has been invaluable to my research. Our coffee conversations have been highlights of my graduate experience, blending technical discussions with genuine camaraderie. I also thank Dr. Claudia Ratti, Dr. Ioannis Pavlidis for their time, insights, and feedback throughout this process.

I owe special thanks to Dr. Jianming Bian, my undergraduate advisor at UC Irvine, whose mentorship and support during my undergraduate years opened the doors that led to this doctoral journey.

I am also grateful to Dr. Alex Himmel, whose tremendous passion for research has been both inspiring and motivating throughout my time in the neutrino physics community.

This work would not have been possible without the guidance and support of several postdoctoral researchers and collaborators. I owe special thanks to Dr. Travis Olson and Dr. Adam Lister. I am also grateful to Dr. Daniel Barrow, Dr. Joshua Barrow and Anne Christensen for their insights and collaboration.

Beyond the physics community, I owe an immeasurable debt to my father, whose sacrifice and vision made this entire journey possible. His decision to send me to the United States for my education, and the tremendous financial commitment he made to support that dream, has shaped my life in ways I can never fully repay. I am forever grateful for his belief in me.

To my wife, Ziye Guo: I can not imagine completing this journey without you by my side.

Your patience, love, and unwavering support have sustained me through every challenge these past 6.5 years. You are simply amazing, and I am immeasurably thankful for you.

Finally, I must acknowledge Ariel, the smartest dog and my most faithful companion, who provided comfort, joy and health.

ABSTRACT

This dissertation presents the first atmospheric neutrino analysis for NOvA and develops the framework for non-standard interaction (NSI) searches in both NOvA and DUNE experiments. Atmospheric neutrinos provide a unique probe for NSI physics through baselines ranging from 15 to 12,800 km – an L/E parameter space inaccessible to beam experiments. While NOvA's surface-level location presents significant cosmic ray challenges, this analysis establishes a baseline performance for atmospheric neutrino detection in NOvA, highlighting DUNE's advantage with its shielded underground position.

A complete atmospheric neutrino analysis for NOvA was developed, implementing Monte Carlo simulation with realistic cosmic overlay to evaluate trigger efficiency, reconstruction performance, and event selection. The neutron-antineutron oscillation trigger, though designed for different physics, achieved 11% efficiency for true atmospheric events while accepting only 0.81% of cosmic background. Event selection was optimized separately for ν_e and ν_μ channels based on their distinct topological signatures.

The NOvA analysis achieved selection efficiencies of 7.3% for ν_e and 32.6% for ν_μ charged-current interactions. However, overwhelming cosmic contamination limited signal purity to 3.1% for ν_e and 0.014% for ν_μ, making precision measurements extremely challenging. Reconstruction performance varied significantly: energy resolution reached 11% for ν_e and 33% for ν_μ at 2 GeV, while angular reconstruction revealed critical limitations –ν_e events achieved $\sigma(\Delta\cos\theta) = 0.287$, but ν_μ suffered severe directional bias with $\sigma(\Delta\cos\theta) = 0.666$ due to vertex reconstruction algorithms trained on beam rather than isotropic flux.

For DUNE, the 1,475-meter underground location will effectively eliminate cosmic backgrounds, enabling meaningful atmospheric NSI searches. My Bayesian analysis framework demonstrates that DUNE can constrain $|\varepsilon_{\mu\tau}| < 0.2$ at a 90% confidence level, with comparable sensitivities for $\varepsilon_{\mu\mu}$ and $\varepsilon_{\tau\tau}$ once beam data becomes available.

This pioneering work establishes the complete framework for atmospheric neutrino NSI searches at liquid argon detectors. Despite NOvA's purity limitations, the analysis provides critical insights: background rejection is paramount, and reconstruction algorithms must be optimized for isotropic flux. These lessons and frameworks position DUNE to fully exploit atmospheric neutrinos as a discovery tool for physics beyond the Standard Model.

TABLE OF CONTENTS

LIST OF TABLES

LIST OF FIGURES

Chapter 1

Introduction

Neutrinos are among the most abundant particles in the universe, about a hundred trillion pass through our bodies every second. However, because they don't have electric charge, and they interact only via the weak force, neutrinos are extremely difficult to detect. Due to this elusiveness, scientists sometimes call them "ghost particles."

Neutrinos are generated from both natural and artificial sources. The Sun and supernovae are major astrophysical neutrino sources, and cosmic ray interactions in Earth's atmosphere produce atmospheric neutrinos. Particle accelerators, like Fermilab's NuMI beam, also produce neutrinos under controlled conditions for neutrino studies. These diverse sources allow us to explore neutrino properties across a wide range of energies and distances. Despite their ghostly nature, neutrinos are believed to be the key to the universe's deepest secrets, including the matter-antimatter asymmetry and physics beyond the Standard Model (BSM).

At the beginning, neutrinos were thought to be massless in the Standard Model (SM) of particle physics, but the discovery of neutrino oscillations provided evidence that they have mass. By studying these oscillations, we can probe the neutrino mass hierarchy and further our understanding of fundamental physics.

One of the most significant breakthroughs in neutrino physics was the resolution of two long-standing problems: the solar neutrino puzzle and the atmospheric neutrino deficit. They played a major role in discovering neutrino oscillation.

The solar neutrino puzzle refers to the discrepancy between the predicted and observed flux of electron neutrinos ν_e from the Sun. The Standard Solar Model predicted a higher number of solar neutrinos than those observed experimentally. Early detectors, such as the Homestake experiment [1], measured only one-third to one-half of the expected flux. This deficit was later confirmed by experiments such as Kamiokande [2], Super-Kamiokande [3], and SAGE [4]. The puzzle remained unsolved until 2002, when the Sudbury Neutrino Observatory (SNO) provided direct evidence that neutrinos were changing flavors as they traveled from the Sun to Earth [5] [6]. SNO was able to measure the neutral current flux which is sensitive to all three flavors (ν_e, ν_μ, ν_τ), and confirmed that the total neutrino flux matched Standard Solar Model predictions. This proved that electron neutrinos were oscillating into muon and tau neutrinos, providing the first definitive evidence of neutrino oscillations.

A similar anomaly was later observed in atmospheric neutrinos, which are produced when cosmic rays interact with the Earth's atmosphere. The original Kamiokande experiment[7] first reported a muon neutrino deficit in the late 1980s, but the effect was not statistically conclusive. The breakthrough came with the Super-Kamiokande experiment in 1998 [3], which observed a large deficit of upward going muon neutrinos compared to the downward going ones, while the electron neutrino sample matched expectations. Subsequent zenith angle studies showed that neutrinos traveling longer distances through the Earth undergo a larger disappearance probability, providing strong evidence for $\nu_\mu \rightarrow \nu_e$ oscillations by Super-Kamiokande analysis in 2004 [8].

The discovery of neutrino oscillations provided compelling evidence that neutrinos have mass and experience flavor mixing [3], challenging the Standard Model's original assumptions. With all oscillation parameters now measured to within 5% precision, except for the CP-violating phase δ_{CP}, this high level of precision enables the study of sub-leading effects that could signal new

physics. One such avenue is the study of non-standard neutrino interactions (NSI), which may provide insight into physics beyond the Standard Model and offer alternative explanations for unresolved neutrino anomalies. NOvA and DUNE, with their high-statistics data sets and long-baseline configurations, are well positioned to probe NSI effects and further our understanding of neutrino interactions.

Chapter 2

Neutrino Physics

2.1 Atmospheric Neutrinos

Atmospheric neutrinos are typically produced about 15 km above Earth's surface when high-energy cosmic rays, primarily protons, collide with nuclei in the Earth's atmosphere. These collisions start a cascade of secondary particles, including short-lived mesons. Mesons, such as pions and kaons, primarily decay into muons and muon neutrinos. The resulting muons further decay into electrons, electron antineutrinos, and muon neutrinos. The full production and decay chain is given by:

$$\begin{aligned} p + N_{\text{air}} \rightarrow \pi^+, K^+ + X + \gamma + \ldots \\ \downarrow \quad \mu^+ + \nu_\mu \\ \downarrow \quad e^+ + \nu_e + \bar{\nu}_\mu \end{aligned} \tag{2.1}$$

Where π^+ and K^+ decay into μ^+ and ν_μ, μ^+ can further decay into e^+, ν_e and $\bar{\nu_\mu}$. This procedure produces roughly $(\nu_\mu + \bar{\nu}_\mu)$ to $(\nu_e + \bar{\nu}_e)$ at a ratio of 2:1.

2.2 Neutrino Oscillation

There are three flavors of neutrinos, ν_e, ν_μ, ν_τ, each of which is a quantum superposition of mass eigenstates $|\nu_1\rangle, |\nu_2\rangle, |\nu_3\rangle$. Neutrinos are produced and detected as flavor eigenstates via the weak interaction, but they propagate as mass eigenstates due to the Schrödinger-like evolution governed by the free Hamiltonian.

The relationship between flavor and mass eigenstates is given by the unitary Pontecorvo–Maki–Nakagawa–Sakata (PMNS) matrix [9] [10], U, which defines the change of basis between the two:

$$|\nu_\alpha\rangle = \sum_{i=1}^{3} U_{\alpha i} |\nu_i\rangle , \tag{2.2}$$

where $\alpha = e, \mu, \tau$, and $i = 1, 2, 3$. For the 3 flavor neutrino in the Standard Model of particle physics, the mixing can be represented in

$$\begin{pmatrix} |\nu_e\rangle \\ |\nu_\mu\rangle \\ |\nu_\tau\rangle \end{pmatrix} \doteq \begin{pmatrix} U_{e1} & U_{e2} & U_{e3} \\ U_{\mu 1} & U_{\mu 2} & U_{\mu 3} \\ U_{\tau 1} & U_{\tau 2} & U_{\tau 3} \end{pmatrix} \begin{pmatrix} |\nu_1\rangle \\ |\nu_2\rangle \\ |\nu_3\rangle \end{pmatrix} , \tag{2.3}$$

The PMNS matrix can also be parameterized as the product of three rotation matrices:

$$U_{\text{PMNS}} = \begin{pmatrix} 1 & 0 & 0 \\ 0 & c_{23} & s_{23} \\ 0 & -s_{23} & c_{23} \end{pmatrix} \begin{pmatrix} c_{13} & 0 & s_{13} e^{-i\delta_{\text{CP}}} \\ 0 & 1 & 0 \\ -s_{13} e^{i\delta_{\text{CP}}} & 0 & c_{13} \end{pmatrix} \begin{pmatrix} c_{12} & s_{12} & 0 \\ -s_{12} & c_{12} & 0 \\ 0 & 0 & 1 \end{pmatrix} , \tag{2.4}$$

where:

$$c_{ij} = \cos\theta_{ij}, \quad s_{ij} = \sin\theta_{ij},$$

δ_{CP} is the CP-violating phase.

The PMNS matrix is written in 3 blocks of unitary matrix because of elementary rotations, with 3 mixing angles: θ_{12}, θ_{23} and θ_{13}, together with one CP-violating phase δ_{CP}, similar to 3D geometry or quantum spin systems. Also, physically, each angle is tied to different neutrino phenomena. The rotation R_{23} is the "atmospheric block" that are dominant by $\nu_\mu \to \nu_\tau$, and mainly studied in atmospheric neutrinos and accelerator experiments at high-E, rotation R_{13} is the "reactor + CP block" that are dominated by $\nu_e \to \nu_\tau$, and mainly studied by reactor experiments. The rotation block R_{12} is the "solar block" that's dominated by $\nu_e \to \nu_\mu$ at low-E. This decomposition allows us to understand how experiments probe different parts of the matrix, it also allows us to comprehend interference effects like CP violation clearly. It also allows us to fit the parameters more systematically.

2.3 Neutrino Oscillation in Vacuum

Neutrino production and detection are determined by their flavor eigenstates; however, their propagation are governed by mass eigenstates. The time evolution of neutrino propagation can be described using the Schrödinger equation.

$$i\frac{\partial}{\partial t}\Psi(\mathbf{r},t) = \hat{H}\Psi(\mathbf{r},t) \tag{2.5}$$

Where the $\hat{H}$ is the Hamiltonian of the system. In the mass basis, the vacuum Hamiltonian is diagonal,

$$\hat{H}_0 \doteq \begin{pmatrix} E_1 & \cdots & 0 \\ \vdots & \ddots & \vdots \\ 0 & \cdots & E_i \end{pmatrix} \tag{2.6}$$

Here the E_1, ..., E_i are the energy eigenvalues of the neutrino ν_i. So the time evolution for neutrinos in vacuum becomes

$$i\frac{\partial}{\partial t}\left|V_i(x,t)\right\rangle = H_0\left|V_i(x,t)\right\rangle \tag{2.7}$$

Therefore, the neutrino mass state time evolution would be:

$$\left|V_i(x,t)\right\rangle = e^{-iE_it}\left|V_i(x)\right\rangle \tag{2.8}$$

When a neutrino of a particular α starts propagating at t=0 and location x, the time evolution of the neutrino becomes:

$$\left|V_\alpha(x,t)\right\rangle = \sum_i U^*_{\alpha i}e^{-iE_it}e^{ip_ix}\left|V_i\right\rangle \tag{2.9}$$

where p_i is ν_i's momentum. Equation (2.9) can be written in terms of flavor states $\beta = e, \mu, \tau$

$$\left|V_\alpha(x,t)\right\rangle = \sum_\beta(\sum_i U^*_{\alpha i}e^{-iE_it}e^{ip_ix})\left|V_\beta\right\rangle \tag{2.10}$$

The oscillation from flavor α to β state is then calculated as projecting $\left|\nu_\alpha\right\rangle$ onto $\left|\nu_\beta\right\rangle$, called the inner product, with the oscillation probability(from t_{init}, x_{init} = 0 to t and x) as:

$$P_{\nu_\alpha\to\nu_\beta} = \left|\left\langle\nu_\beta(x,t)\right|\left|\nu_\alpha(0,0)\right\rangle\right|^2 \tag{2.11}$$

$$= \sum_{i,j} U^*_{\alpha i}U_{\beta i}U_{\alpha j}U^*_{\beta j}e^{-i(E_i-E_j)t} \tag{2.12}$$

Because neutrinos are relativistic with extremely small mass, the energy can be written in Taylor expansion while ignoring high order terms as

$$E_i = \sqrt{p_i^2 + m_i^2} = p_i \sqrt{1 + \frac{m^2}{p_i^2}} \tag{2.13}$$

$$= p_i (1 + \frac{m^2}{2p_i^2} + \frac{m^4}{8p_i^4} + ...) \tag{2.14}$$

$$\approx p_i + \frac{m^2}{2p_i^2} \tag{2.15}$$

And for neutrinos, neutrino energy E $\approx p_i$, and therefore we can write

$$E_i \approx E + \frac{m_i^2}{2E} \tag{2.16}$$

Therefore the term $E_i - E_j$ can be approximated to:

$$\begin{aligned} E_i - E_j &\simeq \left(E + \frac{m_i^2}{2E}\right) - \left(E + \frac{m_j^2}{2E}\right) \\ &= \frac{m_i^2 - m_j^2}{2E_\nu} = \frac{\Delta m_{ij}^2}{2E_\nu}. \end{aligned} \tag{2.17}$$

where the $\Delta m_{ji}^2 \doteq m_j^2 - m_i^2$. Therefore, equation 2.11 becomes:

$$P_{\nu_\alpha \to \nu_\beta} = \sum_{i,j} U_{\alpha i}^* U_{\beta i} U_{\alpha j} U_{\beta j}^* \exp\left(-i \frac{\Delta m_{ji}^2}{2E} L\right). \tag{2.18}$$

When α and β are the same flavor, the oscillation probability is called a survival probability, because it will tell us the percentage of this flavor left. Then 2.18 becomes:

$$P_{\nu_\alpha \to \nu_\alpha} = 1 - 4 \sum_{j>i} \left|U_{\alpha i} U_{\alpha j}\right|^2 \sin^2\left(\frac{\Delta m_{ji}^2 L}{4E}\right). \tag{2.19}$$

Notice here the oscillation probability is directly proportional to L/E, and we call ϕ_{osc} the oscillation phase, defined as

$$\phi_{osc} \doteq \frac{\Delta m^2_{ij} L}{4E} \tag{2.20}$$

2.4 2 Flavor approximation

Although neutrino oscillations are fundamentally a three flavor phenomenon, two flavor approximation is often introduced to explain physics of oscillation in a simple analytic form. This approximation only considers a single mass splitting and mixing angle, and the three flavor framework reduces to an effective 2 state system. This approximation is widely used for intuition and clarity, where subleading oscillation terms are small or averaged out. In this 2 flavor approximation case, the mixing matrix U reduces into just a rotation matrix:

$$U = \begin{pmatrix} \cos(\theta) & \sin(\theta) \\ -\sin(\theta) & \cos(\theta) \end{pmatrix} \tag{2.21}$$

$$\begin{pmatrix} |\nu_\alpha\rangle \\ |\nu_\beta\rangle \end{pmatrix} \doteq \begin{pmatrix} \cos(\theta_{ij}) & \sin(\theta_{ij}) \\ -\sin(\theta_{ij}) & \cos(\theta_{ij}) \end{pmatrix} \begin{pmatrix} |\nu_i\rangle \\ |\nu_j\rangle \end{pmatrix}. \tag{2.22}$$

Then the equation 2.18 becomes:

$$P_{\nu_\alpha \to \nu_\beta} = \sin^2(2\theta_{ij}) \sin^2\left(\frac{\Delta m^2_{ji} L}{4E}\right) \tag{2.23}$$

It can also be visualized in Fig. 2.1 When $\alpha \neq \beta$, the oscillation (survival) probability P($\alpha \to \alpha$) is simply 1-P($\alpha \to \beta$)

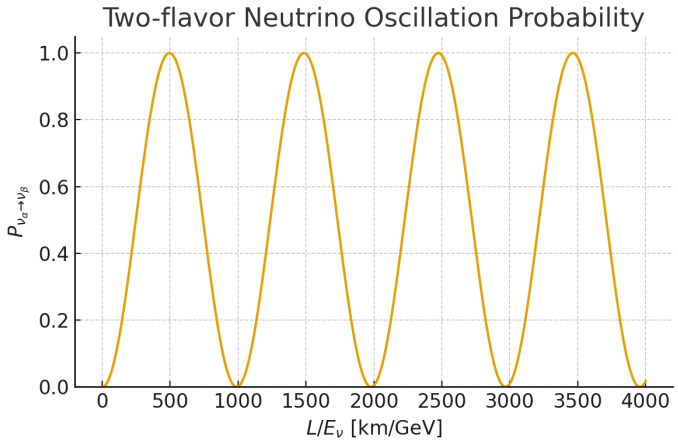

Figure 2.1: Two flavor oscillation approximation, over L/E

2.5 Standard Neutrino Oscillation in Matter

Neutrinos oscillate in vacuum solely because there's a mismatch between flavor eigenstates and mass eigenstates. However, when neutrinos propagate through matter, additional coherent forward scattering interactions modify their effective propagation Hamiltonian, as first introduced by Wolfenstein [11]. When neutrinos travel through the Earth, ν_e undergo coherent forward scattering with electrons in Earth via charged current (CC) interactions with exchange of $W^{\pm}$ bosons (fig. 2.2). ν_μ and ν_τ experience only flavor universal neutral current (NC) scattering with exchange of Z^0 bosons (fig. 2.2), which does not affect oscillation and can be safely ignored. This results in modification of effective mixing angle and mass squared difference, and is known as the Mikheyev-Smirnov-Wolfenstein (MSW) [12] effect, also known as the matter effect.

In addition to the vacuum Hamiltonian H_0, we add the matter effect Hamiltonian H_{matter}; therefore in the flavor basis, they can be written as

$$H_f = U^\dagger H_0 U + H_{matter} \tag{2.24}$$

Since Earth is lacking μ and τ, the main interaction through Earth is electron neutrino coherent

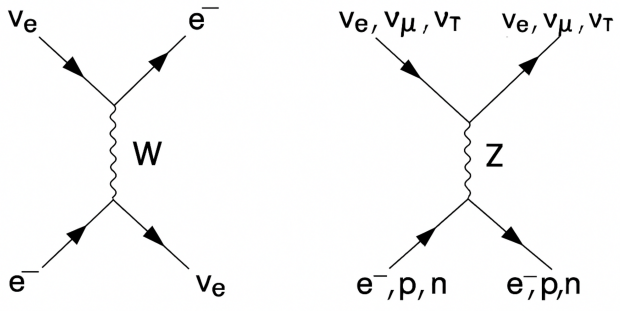

Figure 2.2: Feynman diagram of charge current interaction (a) and neutral current interaction (b) for matter effect

forward scattering, and the standard matter effect due to Hamiltonian potential is:

$$H_{\text{matter}} = \pm V_{CC} \begin{pmatrix} 1 & 0 & 0 \\ 0 & 0 & 0 \\ 0 & 0 & 0 \end{pmatrix}, \tag{2.25}$$

where V_{CC} is the flavor dependent phase to electron neutrinos:

$$V_{CC} = \pm\sqrt{2G_F N_e} \tag{2.26}$$

G_F is the Fermi coupling constant, and N_e is the density of electrons. The $\pm$ is for neutrino (positive) and anti-neutrino (negative).

Therefore, the new Schrödinger equation can be written as:

$$i\frac{d}{dt}\begin{pmatrix} \nu_e \\ \nu_\mu \\ \nu_\tau \end{pmatrix} = \left[\frac{1}{2E_\nu} U M^2 U^\dagger + \begin{pmatrix} V_{CC} & 0 & 0 \\ 0 & 0 & 0 \\ 0 & 0 & 0 \end{pmatrix} \right] \begin{pmatrix} \nu_e \\ \nu_\mu \\ \nu_\tau \end{pmatrix}, \tag{2.27}$$

Where

$$M^2 = diag(m_1^2, m_2^2, m_3^2) \tag{2.28}$$

and with $a \equiv 2E_\nu V_{CC}$,

$$H_f = \frac{1}{2E_\nu}\left[UM^2U^\dagger + \begin{pmatrix} a & 0 & 0 \\ 0 & 0 & 0 \\ 0 & 0 & 0 \end{pmatrix}\right]. \tag{2.29}$$

The oscillation probability is then:

$$P_{\nu_\mu\to\nu_e} \approx 4s_{13}^2 s_{23}^2 \frac{\sin^2[(1-A)\Delta]}{(1-A)^2} + 8c_{12}s_{12}c_{23}s_{23}s_{13}\alpha \frac{\sin(A\Delta)\sin[\Delta(1-A)]}{A(1-A)}\cos(\Delta+\delta_{\rm CP}), \tag{2.30}$$

where

$$\Delta \equiv \frac{\Delta m_{31}^2 L}{4E}, \qquad A \equiv \frac{2EV}{\Delta m_{31}^2}, \qquad \alpha \equiv \frac{\Delta m_{21}^2}{\Delta m_{31}^2}. \tag{2.31}$$

Since neutrino oscillation probabilities depend only on mass-squared differences and not absolute masses, we can redefine the mass-squared matrix by subtracting m_1^2 from each diagonal element:

$$M^2 = \text{diag}(m_1^2, m_2^2, m_3^2) = \text{diag}(0, \Delta m_{21}^2, \Delta m_{31}^2) + m_1^2 \cdot \mathbb{I} \tag{2.32}$$

where $\Delta m_{21}^2 = m_2^2 - m_1^2$ and $\Delta m_{31}^2 = m_3^2 - m_1^2$ are the mass-squared differences, and $\mathbb{I}$ is the 3×3 identity matrix. The term proportional to the identity matrix, $\frac{m_1^2}{2E_\nu}\mathbb{I}$, equally to all mass eigenstates and are not flavor changing. Therefore, Eqn 2.28 can be simplified to:

$$M^2 \to \text{diag}(0, \Delta m_{21}^2, \Delta m_{31}^2). \tag{2.33}$$

2.6 Experimental Status for Standard Oscillation

Before introducing potential beyond standard model (BSM) physics through NSI, I would like to first establish the current state of standard three flavor neutrino oscillation measurements. Over the

past two decades, a global program of reactor, accelerator, solar and atmospheric neutrino experiments and their cross fitting has enabled high precision measurements in the standard framework.

2.6.1 Global Fit Results

The most recent global analysis (NuFit 6.0, September 2024) [13] combines data from long baseline accelerator experiments (NOvA and T2K), reactor experiments (Daya Bay, Reno, Souble, Chooz), Solar experiments (Super-K, SNO, Borexino), and atmospheric neutrino experiments (Super-K, IceCube) to determine the six parameters governing standard oscillation. Table 2.3 shows the best fit values and uncertainties for both mass orderings.

The table shows results under two scenarios: for including atmospheric neutrino data, top half only uses data from IceCube, whereas the bottom half includes both IceCube data and Super-K data.

θ_{23} and Δm^2_{32} dominate the atmospheric mixing parameters due to 2.4 left matrix dominating the atmospheric neutrino $\mu - \tau$ sector oscillation. They are sensitive to the $\nu_\mu(\bar{\nu_\mu}) \to \nu_\mu(\bar{\nu_\mu})$ survival and $\nu_\mu(\bar{\nu_\mu}) \to \nu_e(\bar{\nu_e})$ disappearance. However, the atmospheric mixing angle θ_{23} suffers from the octant ambiguity shown in fig. 2.4. Current data cannot definitely determine if θ_{23} is in the upper octant ($> 45^\circ$) or lower octant ($< 45^\circ$), though the best fit with SK data favors the lower octant. We will see this ambiguity could lead to degeneracy in the $\mu - \tau$ sector for NSI parameters. The neutrino mass ordering remains under investigation. The global fit including Super Kamiokande atmospheric data prefers normal ordering with $\Delta\chi^2 = 6.1$ (2.5σ), but this represents only a modest preference [13]. The CP-violating phase δ_{CP} shows ordering dependent behavior: for normal ordering, the data are consistent with CP conservation within 1σ, while inverted ordering favors maximal CP violation around $\delta_{CP} \approx 270^\circ$ at more than 3σ.

		Normal Ordering ($\Delta\chi^2 = 0.6$)		Inverted Ordering (best fit)	
		bfp $\pm 1\sigma$	3σ range	bfp $\pm 1\sigma$	3σ range
IC19 without SK atmospheric data	$\sin^2\theta_{12}$	$0.307^{+0.012}_{-0.011}$	$0.275 \to 0.345$	$0.308^{+0.012}_{-0.011}$	$0.275 \to 0.345$
	$\theta_{12}/^\circ$	$33.68^{+0.73}_{-0.70}$	$31.63 \to 35.95$	$33.68^{+0.73}_{-0.70}$	$31.63 \to 35.95$
	$\sin^2\theta_{23}$	$0.561^{+0.012}_{-0.015}$	$0.430 \to 0.596$	$0.562^{+0.012}_{-0.015}$	$0.437 \to 0.597$
	$\theta_{23}/^\circ$	$48.5^{+0.7}_{-0.9}$	$41.0 \to 50.5$	$48.6^{+0.7}_{-0.9}$	$41.4 \to 50.6$
	$\sin^2\theta_{13}$	$0.02195^{+0.00054}_{-0.00058}$	$0.02023 \to 0.02376$	$0.02224^{+0.00056}_{-0.00057}$	$0.02053 \to 0.02397$
	$\theta_{13}/^\circ$	$8.52^{+0.11}_{-0.11}$	$8.18 \to 8.87$	$8.58^{+0.11}_{-0.11}$	$8.24 \to 8.91$
	$\delta_{\rm CP}/^\circ$	177^{+19}_{-20}	$96 \to 422$	285^{+25}_{-28}	$201 \to 348$
	$\frac{\Delta m^2_{21}}{10^{-5}\ \mathrm{eV}^2}$	$7.49^{+0.19}_{-0.19}$	$6.92 \to 8.05$	$7.49^{+0.19}_{-0.19}$	$6.92 \to 8.05$
	$\frac{\Delta m^2_{3\ell}}{10^{-3}\ \mathrm{eV}^2}$	$+2.534^{+0.025}_{-0.023}$	$+2.463 \to +2.606$	$-2.510^{+0.024}_{-0.025}$	$-2.584 \to -2.438$
		Normal Ordering (best fit)		Inverted Ordering ($\Delta\chi^2 = 6.1$)	
		bfp $\pm 1\sigma$	3σ range	bfp $\pm 1\sigma$	3σ range
IC24 with SK atmospheric data	$\sin^2\theta_{12}$	$0.308^{+0.012}_{-0.011}$	$0.275 \to 0.345$	$0.308^{+0.012}_{-0.011}$	$0.275 \to 0.345$
	$\theta_{12}/^\circ$	$33.68^{+0.73}_{-0.70}$	$31.63 \to 35.95$	$33.68^{+0.73}_{-0.70}$	$31.63 \to 35.95$
	$\sin^2\theta_{23}$	$0.470^{+0.017}_{-0.013}$	$0.435 \to 0.585$	$0.550^{+0.012}_{-0.015}$	$0.440 \to 0.584$
	$\theta_{23}/^\circ$	$43.3^{+1.0}_{-0.8}$	$41.3 \to 49.9$	$47.9^{+0.7}_{-0.9}$	$41.5 \to 49.8$
	$\sin^2\theta_{13}$	$0.02215^{+0.00056}_{-0.00058}$	$0.02030 \to 0.02388$	$0.02231^{+0.00056}_{-0.00056}$	$0.02060 \to 0.02409$
	$\theta_{13}/^\circ$	$8.56^{+0.11}_{-0.11}$	$8.19 \to 8.89$	$8.59^{+0.11}_{-0.11}$	$8.25 \to 8.93$
	$\delta_{\rm CP}/^\circ$	212^{+26}_{-41}	$124 \to 364$	274^{+22}_{-25}	$201 \to 335$
	$\frac{\Delta m^2_{21}}{10^{-5}\ \mathrm{eV}^2}$	$7.49^{+0.19}_{-0.19}$	$6.92 \to 8.05$	$7.49^{+0.19}_{-0.19}$	$6.92 \to 8.05$
	$\frac{\Delta m^2_{3\ell}}{10^{-3}\ \mathrm{eV}^2}$	$+2.513^{+0.021}_{-0.019}$	$+2.451 \to +2.578$	$-2.484^{+0.020}_{-0.020}$	$-2.547 \to -2.421$

Figure 2.3: Three flavor oscillation parameters from NuFit 6.0 [13]. Values shown include both variants with (top) and without (bottom) Super-Kamiokande atmospheric data. NO = normal ordering, IO = inverted ordering

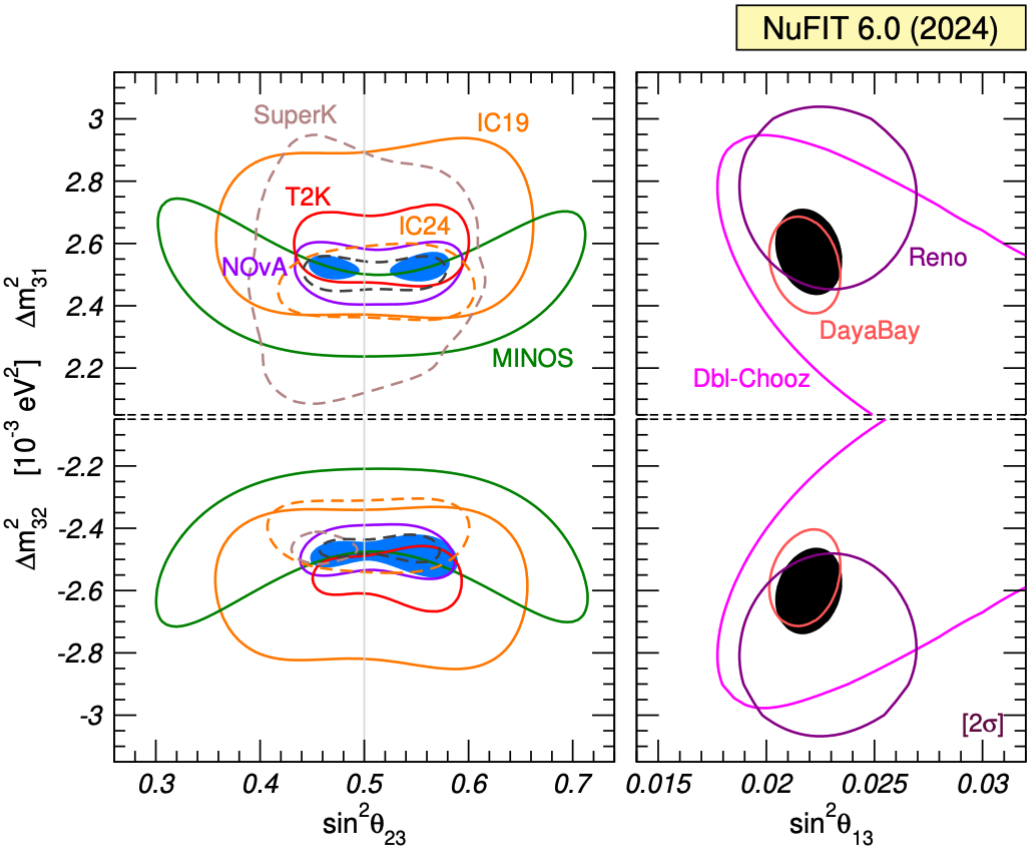

Figure 2.4: 95.45% confidence regions (2 dof) for the oscillation parameters in the $\sin^2\theta_{23}$–$\Delta m^2_{3\ell}$ (left) and $\sin^2\theta_{13}$–$\Delta m^2_{3\ell}$ (right) planes. The left panels show constraints from the accelerator experiments MINOS, NOvA, and T2K, together with atmospheric data from IceCube and Super-Kamiokande, combined with a reactor prior on θ_{13}. The right panels show the corresponding reactor measurements from Daya Bay, Double Chooz, and RENO. Solar, KamLAND, and SNO+ data are included to constrain Δm^2_{21} and θ_{12}. Contours are defined with respect to the global minima of each mass ordering. [13]

2.6.2 Implications for NSI Searches

Well measured parameters such as θ_{13} and Δm^2_{31} constrain how much NSI can modify oscillation patterns. However, remaining ambiguities in θ_{23} and the mass ordering create potential degeneracies with NSI parameters that must be considered in fits. Atmospheric neutrino measurements provide unique NSI sensitivity by probing wide ranges of baselines and matter densities simultaneously, offering complementary constraints to reactor and long-baseline accelerator experiments.

2.7 Non-standard Neutrino Interaction

2.7.1 Motivation and Historical Origin

The idea that neutrino propagation can be modified by coherent forward scattering in matter was first introduced by Wolfenstein in 1978 [11], as discussed in section 2.5. This forms the foundation for the MSW effect, which successfully explains solar neutrino observations through resonant flavor conversion in the Sun. However, in the same work, Wolfenstein noted that additional neutral-current-like interactions beyond the Standard Model could also contribute to the effective matter potential.

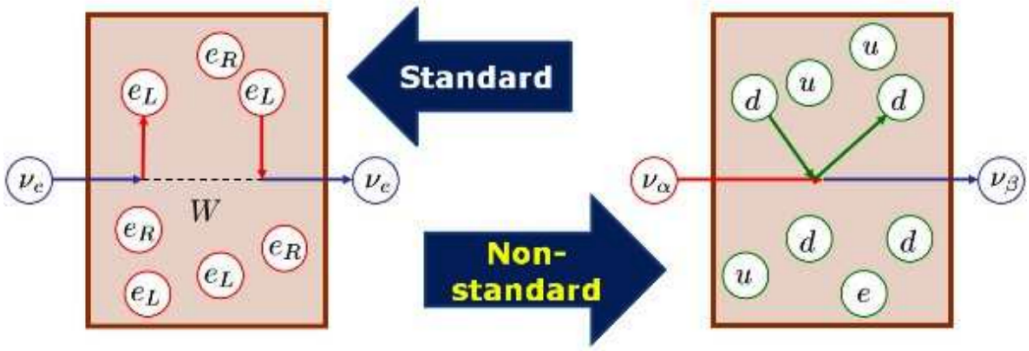

Figure 2.5: Standard matter effect oscillation (left) and matter NSI (right) [14]

These types of beyond-Standard-Model (BSM) effects, known as non-standard interactions (NSI), would modify how neutrinos travel through matter by changing the effective potential experienced by each flavor of neutrino. In the Standard Mode, only ν_e experience a matter effect through charged current interaction with electrons. NSI, however, allows additional interactions that could affect all flavors in fig. 2.5, including new flavor changing terms or shift in the diagonal elements of the matter potential. If the NSI effect exists, these interactions would distort the expected oscillation pattern as neutrinos pass through the Earth, leading to deviations that depend on energy, baseline and flavor of neutrino. This distortion can be searched for in atmospheric and long baseline neutrino experiments [15, 14, 16]

2.7.2 The NSI Effective Operator Framework

NSI interactions are parameterized through effective four-fermion operators that couple neutrino currents to matter fermion currents. The general Lagrangian for NSI in matter can be written phenomenologically for vector NSI as [17]:

$$\mathscr{L}_{\text{NC-NSI}} = -\sqrt{2}G_F \sum_{f,P,\alpha,\beta} \varepsilon_{\alpha\beta}^{fP} (\bar{\nu}_\alpha \gamma^\mu P_L \nu_\beta)(\bar{f}\gamma_\mu P f) \tag{2.34}$$

$$\mathscr{L}_{\text{CC-NSI}} = -\sqrt{2}G_F \sum_{f,P,\alpha,\beta} \varepsilon_{\alpha\beta}^{fP} (\bar{\nu}_\alpha \gamma^\mu P_L \nu_\beta)(\bar{f}\gamma_\mu P f') \tag{2.35}$$

where G_F is the Fermi constant, f, f' are the first generation fermion (e, u, d) for SM. P is the chiral projector L, $R = (1 \pm \gamma^5)/2$, α and β are two flavors of neutrino. $\varepsilon_{\alpha\beta}^{fP}$ represents the dimensionless NSI coupling strength relative to G_F for neutrinos interacting with fermion f with chirality P. $\varepsilon_{\alpha\beta}^{fP} \propto \mathscr{O}(\frac{G_M}{G_F})$, G_M is the coupling constant.

For scalar-type NSI:

$$\mathscr{L}_{\text{NSI}}^{S} = -2\sqrt{2}G_F \sum_{f,P,\alpha,\beta} \varepsilon_{\alpha\beta}^{fP,S} (\bar{\nu}_\alpha P_L \nu_\beta)(\bar{f} P f) \tag{2.36}$$

The key difference between vector NSI and scalar NSI involves the vector current $\bar{f}\gamma_\mu f$ (with a Lorentz index μ), and scalar interactions involve the scalar bilinear $\bar{f}f$ (no Lorentz index), and this matters because vector NSI produces velocity dependent effects and coherent forward scattering, contributing to the effective matter potential during neutrino propagation. The matter potential scales linearly with the number density N_f.

Scalar NSI produces velocity independent effects and does not contribute to coherent forward scattering in the relativistic limit (the scalar current $\bar{f}f$ vanishes for massless fermions). They affect neutrino interactions but not propagation through matter.

For atmospheric neutrino oscillation at multi GeV energies, matter effects dominate the NSI

sensitivity, and vector NSI is the primary concern; therefore, this analysis will focus exclusively on vector NSI.

In principle, NSI couplings can differ between electrons and quarks, and between left and right-handed fermions. The most general case requires specifying $\varepsilon^{eL}_{\alpha\beta}$, $\varepsilon^{eR}_{\alpha\beta}$, $\varepsilon^{uL}_{\alpha\beta}$, $\varepsilon^{uR}_{\alpha\beta}$, $\varepsilon^{dL}_{\alpha\beta}$, and $\varepsilon^{dR}_{\alpha\beta}$ separately for each neutrino flavor combination. However, many beyond-Standard-Model theories predict approximate universality or specific coupling patterns. In this analysis, I consider only NSI coupling to electrons ($\varepsilon^{e}_{\alpha\beta}$) and set the quark couplings to zero ($\varepsilon^{u}_{\alpha\beta} = \varepsilon^{d}_{\alpha\beta} = 0$). This choice is made because leptonic NSI (coupling only to electrons) have less stringent theoretical and experimental constraints than hadronic NSI (coupling to quarks). Therefore, 2.35 becomes:

$$\mathscr{L}^{e}_{\text{NSI}} = -2\sqrt{2}G_F \sum_{\alpha,\beta} \varepsilon^{e}_{\alpha\beta}(\bar{\nu}_\alpha \gamma^\mu P_L \nu_\beta)(\bar{e}\gamma_\mu e) \tag{2.37}$$

For neutrino propagation, coherent forward scattering off the electron background generates an effective potential. The NSI contribution to the matter potential is:

$$V^{\text{NSI}}_{\alpha\beta} = \sqrt{2}G_F N_e \varepsilon^{e}_{\alpha\beta} \tag{2.38}$$

This adds to the Standard Model charged-current potential $V_{CC} = \sqrt{2}G_F N_e \delta_{\alpha e}$ to give the total matter potential:

$$V^{\text{matter}}_{\alpha\beta} = \sqrt{2}G_F N_e(\delta_{\alpha e} + \varepsilon^{e}_{\alpha\beta}) \tag{2.39}$$

In matrix form, this can be written as:

$$V^{\text{matter}} = \sqrt{2}G_F N_e \begin{pmatrix} 1+\varepsilon_{ee} & \varepsilon_{e\mu} & \varepsilon_{e\tau} \\ \varepsilon^*_{e\mu} & \varepsilon_{\mu\mu} & \varepsilon_{\mu\tau} \\ \varepsilon^*_{e\tau} & \varepsilon^*_{\mu\tau} & \varepsilon_{\tau\tau} \end{pmatrix} \tag{2.40}$$

where the "1" in the $(1,1)$ position represents the Standard Model charged-current contribution δ_{ee}, and the $\varepsilon_{\alpha\beta}$ terms are the NSI contributions. The matrix is Hermitian ($\varepsilon^*_{\alpha\beta} = \varepsilon_{\beta\alpha}$) to ensure unitary time evolution.

The total Hamiltonian is then the sum of the vacuum Hamiltonian and the matter potential:

$$H_{\text{total}} = H_{\text{vac}} + V^{\text{matter}} = \frac{1}{2E} U \begin{pmatrix} 0 & 0 & 0 \\ 0 & \Delta m^2_{21} & 0 \\ 0 & 0 & \Delta m^2_{31} \end{pmatrix} U^\dagger + \sqrt{2} G_F N_e \begin{pmatrix} 1+\varepsilon_{ee} & \varepsilon_{e\mu} & \varepsilon_{e\tau} \\ \varepsilon^*_{e\mu} & \varepsilon_{\mu\mu} & \varepsilon_{\mu\tau} \\ \varepsilon^*_{e\tau} & \varepsilon^*_{\mu\tau} & \varepsilon_{\tau\tau} \end{pmatrix} \quad (2.41)$$

where U is the standard PMNS mixing matrix and E is the neutrino energy.

In the SM limits, all NSI parameters $\varepsilon_{\alpha\beta} = 0$, and it reduces to the matter potential with only the $(1,1)$ entry non-zero, affecting only ν_e. NSI generalizes this by allowing all flavors to experience matter effect(diagonal terms) and flavor changing interactions during propagation (off-diagonal terms). With the modification of NSI to the Hamiltonian, the oscillation probability changes matter effect oscillation probability 2.30 to :

$$P(\nu_\alpha \to \nu_\beta; L, E) = \left| \left\langle \nu_\beta \left| \exp\left(-i \int_0^L H_{\text{total}}(x) dx \right) \right| \nu_\alpha \right\rangle \right|^2 \quad (2.42)$$

The resulting probabilities depend on both standard oscillation parameters and the six NSI parameters, creating distinctive L/E-dependent patterns explored in Chapter 4.

2.7.3 Experimental Status of NSI

Global experiments have been searching for NSI during the past two decades. Recent global analyses [18, 19] combine data from reactor experiments (Daya Bay, RENO, Double Chooz), long-baseline accelerator experiments (T2K, NOvA, MINOS), atmospheric neutrino measurements (Super-Kamiokande, IceCube), and solar neutrino experiments (Super-Kamiokande, SNO, Borexino) to constrain NSI parameters.

Global Constraints

The most comprehensive recent global analysis by Coloma et al. [18] combined oscillation data from multiple experiments to constrain NSI parameters. At 90% confidence level, most NSI parameters are constrained to $|\varepsilon_{\alpha\beta}| \lesssim 0.1$–$0.3$, though significant variation exists across the parameter space. Figure 2.6 shows representative global constraints on selected NSI parameters.

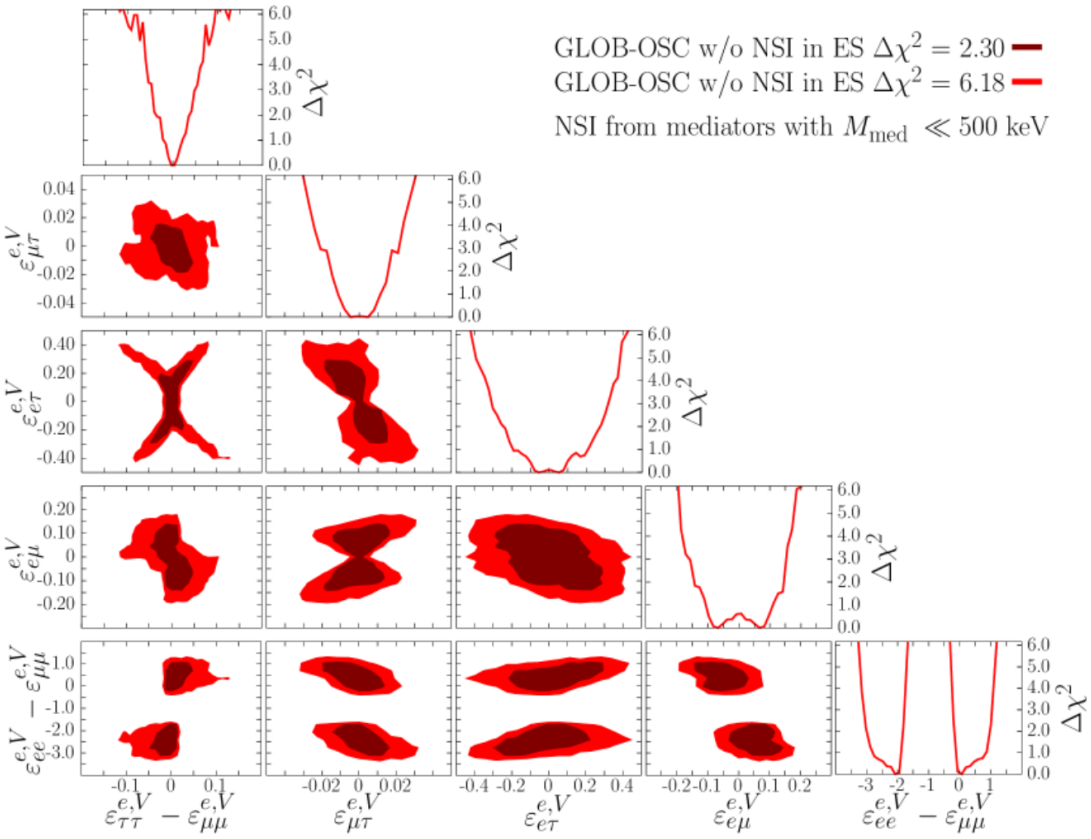

Figure 2.6: Global constraints on NSI parameters with electrons from Coloma et al. [18]. Each panel shows two-dimensional projections of the allowed parameter space after marginalizing over undisplayed parameters. The red regions correspond to 1σ (inner) and 2σ (outer) allowed regions. Note that only differences of diagonal elements ($\varepsilon_{ee} - \varepsilon_{\mu\mu}$ and $\varepsilon_{\tau\tau} - \varepsilon_{\mu\mu}$) are constrained by oscillation data, as overall shifts affect all flavors equally and are unobservable.

The global constraints table 2.7 show that most NSI parameters are bounded to $|\varepsilon_{\alpha\beta}| \lesssim 0.1$–$0.2$ at 90% CL. All parameters remain consistent with zero, meaning no evidence for NSI has been

	Vector ($X = V$)	
	Borexino	**GLOB-OSC w NSI in ES**
$\varepsilon_{ee}^{e,X}$	$[-1.1, +0.17]$	$[-0.13, +0.10]$
$\varepsilon_{\mu\mu}^{e,X}$	$[-2.4, +1.5]$	$[-0.20, +0.10]$
$\varepsilon_{\tau\tau}^{e,X}$	$[-2.8, +2.1]$	$[-0.17, +0.093]$
$\varepsilon_{e\mu}^{e,X}$	$[-0.83, +0.84]$	$[-0.097, +0.011]$
$\varepsilon_{e\tau}^{e,X}$	$[-0.90, +0.85]$	$[-0.18, +0.080]$
$\varepsilon_{\mu\tau}^{e,X}$	$[-2.1, +2.1]$	$[-0.0063, +0.016]$

Figure 2.7: 90% CL bounds on NSI parameters with electrons from the global oscillation analysis by Coloma et al. [18]. The bounds assume vector NSI ($X = V$) and marginalize over all other NSI and oscillation parameters. These constraints include NSI effects in both propagation and detection cross-sections.

observed. The tightest constraint is on $\varepsilon_{\mu\tau}$ at the level of ~ 0.01, while $\varepsilon_{e\tau}$ allows values up to ~ 0.2.

This thesis presents searches for NSI using atmospheric neutrinos in both NOvA and DUNE. Chapter 4 explores NSI signatures in atmospheric neutrino oscillation and event distributions. Chapter 5 describes the NOvA atmospheric neutrino analysis, including event selection, reconstruction, and background estimation. Chapter 6 presents the DUNE analysis framework, including atmospheric flux systematic uncertainties and the MaCh3 Bayesian MCMC fitting methodology. Chapter 7 presents NSI constraints from both experiments, with NOvA providing current limits and DUNE demonstrating future sensitivity. Chapter 8 summarizes the findings and discusses prospects for atmospheric neutrino NSI searches.

Chapter 3

Experiments

3.1 NOvA Experiment

The NuMI Off-axis ν_e Appearance (NOνA) experiment is a long baseline neutrino experiment with a two detector setup. The Far Detector (FD) is located in Ash River, Minnesota, 810 km away from the NuMI beam neutrino source. The Near Detector (ND) is located in Fermi National Accelerator Laboratory (Fermilab) near Chicago, IL and is 100 meters underground. NuMI is short for Neutrinos at the Main Injector. The main objective for NOvA is to observe $\nu_\mu/\bar{\nu_\mu}$ disappearance and $\nu_e/\bar{\nu}_e$ appearance, and to measure the neutrino oscillation angle $\sin^2\theta_{23}$, the mass ordering Δm^2_{32} and the constraints for CP violation phase δ_{CP}. The off-axis in the name is caused by both ND and FD being 14 mrad off the axis of the primary direction of the NuMI beam. Due to NuMI beam traveling through the Earth, NOvA is also affected by the matter effect [11], and the energy peaks at 2 GeV, which shares similarities with the atmospheric neutrino energy distribution at NOvA Far Detector.

3.1.1 The NuMI Beam

Similar to generation of atmospheric neutrinos that takes advantage of cosmic rays, mainly protons, hitting the Earth's atmosphere and producing pions and kaons, the NuMI beam utilizes similar procedure. Fermilab uses an accelerator complex [20], shown in Fig. 3.2. which directs a proton beam into the NuMI beamline.

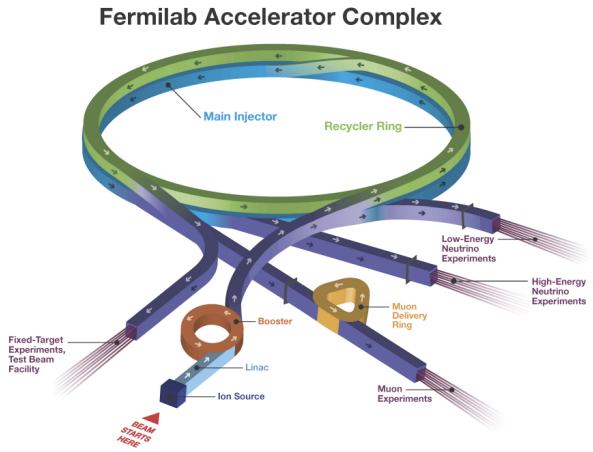

Figure 3.1: Fermilab Accelerator Complex. Linear accelerator (Linac) accelerates protons and feed them into the booster, which is then fed into the Recycler Ring, and then accelerates further into the Main Injector. The Main Injector then decides which beamline to direct the accelerated protons to. [20]

The Fig 3.2 shows how neutrinos are produced using NuMI beam. After protons are directed into NuMI beamline, protons hit a graphite target, and hit the nuclei, producing charged pions and kaons, similar to when cosmic rays hit the Earth's atmosphere and produce pions and kaons. Then the charged particles are further directed into the Target Hall where we use two magnetic focusing horns to focus the secondary particles into the Decay Pipe. We then use a Hadron Monitor to monitor the hadronic activity and use a 5 meter long Absorber to stop non-decayed secondary particles to ensure purity of the beam while allowing only muons and muon neutrinos to go through. Several layers of Muon monitors are then placed into the rock to monitor the amount of muons and analyze the beam more accurately. Neutrinos produced in this process will travel through the

Earth and arrive at the ND first; some of them could be detected by the ND while others continue traveling to the FD.

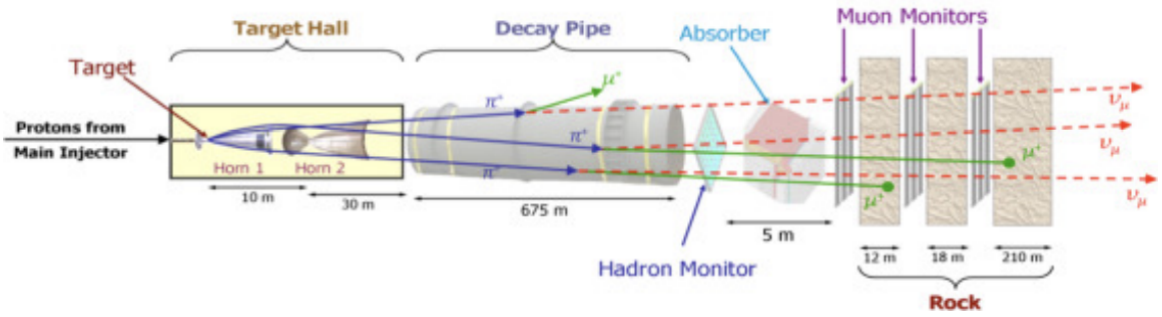

Figure 3.2: NuMI beam with protons hit the target producing hadrons which are directed by magnetic horns, (either FHC or RHC mode). The hadrons then travel into decay pipe and decay neutrinos [21]

3.1.2 Off-axis Design

As the name off-axis in NOvA suggests, a key design feature of NOvA is the position of the detectors being 14.6 mrad off the central axis of the NuMI beam [22].

In the NuMI beam, neutrinos are produced primarily through the two-body decay $\pi^+ \rightarrow \mu^+ + \nu_\mu$. Due to the kinematics of this decay, the neutrino energy depends on both the parent pion energy and the angle relative to the pion's direction. For a pion traveling nearly parallel to the beamline, neutrinos observed at small off-axis angles have lower and more monochromatic energies compared to those observed on-axis.

Figure 3.3 shows this effect. The top panel shows the neutrino flux as a function of energy for various off-axis angles. When On-axis ($\theta = 0$), the spectrum is broad, extending to high energies with a peak around 6-8 GeV. As the off-axis angle increases, the spectrum narrows and shifts to lower energies. At 14.6 mrad, the flux peaks sharply near 2 GeV, with significantly reduced high-energy tails.

The choice of 14.6 mrad off-axis angle optimizes the overlap between the neutrino flux and

the oscillation probability maximum. For NOvA's 810 km baseline, the first oscillation maximum for $\nu_\mu \rightarrow \nu_e$ appearance occurs at approximately 2 GeV (assuming $\Delta m^2_{32} \approx 2.5 \times 10^{-3}$ eV^2). By positioning the detectors 14.6 mrad off-axis, the beam energy spectrum is concentrated at this oscillation maximum, maximizing sensitivity to θ_{13} and the CP-violating phase δ_{CP}.

This off-axis design provides NOvA with excellent energy resolution for oscillation measurements because of the off-axis design which eliminates higher energy neutrinos, suppressing backgrounds from NC interactions and wrong sign contamination. The narrow energy spectrum also reduces systematic uncertainties associated with neutrino cross-section modeling, as the analysis is concentrated in a limited energy range where interaction models are better constrained.

3.1.3 The NOvA Detectors

There are two detectors in NOvA experiment, both are made of PVC pipes that are filled with mineral oil serving as liquid scintillator. The Near Detector is located 1 km away from the target hall, underground in Fermilab, whereas the Far Detector is 810 km away from Fermilab in Ash River, Minnesota. The ND is 290 tons in liquid scintillator weight and the FD is 14 kiloton. They are both placed 14.6 mrad off axis of the NuMI beam center line to reduce systematic uncertainties.

Figure 3.4 shows the ND and FD's size respectively, and each cell's size relative to human hand. The NOVA FD contains 896 vertical and horizontal planes, each plane has 12 extrusion modules, where each module contains 32 PVC cells, therefore each plane has 384 cells, and the entire FD has 344,064 total cells.

Each cell looks like Fig 3.5. It is filled with a wavelength shifting fiber loop and liquid scintillator (mineral oil). The fiber catches blue light that have wavelengths of around 400 to 450 nm and shifts the wavelength to green light around 490 to 550 nm. The lights from each wavelength shifting fiber then travels to the avalanche photodiodes (APD).

The APDs are specifically made for Fermilab by Hamamatsu with 32 channels. They're used to readout all of the signals from 32 wavelength shifting fibers each. These APDs can detect green

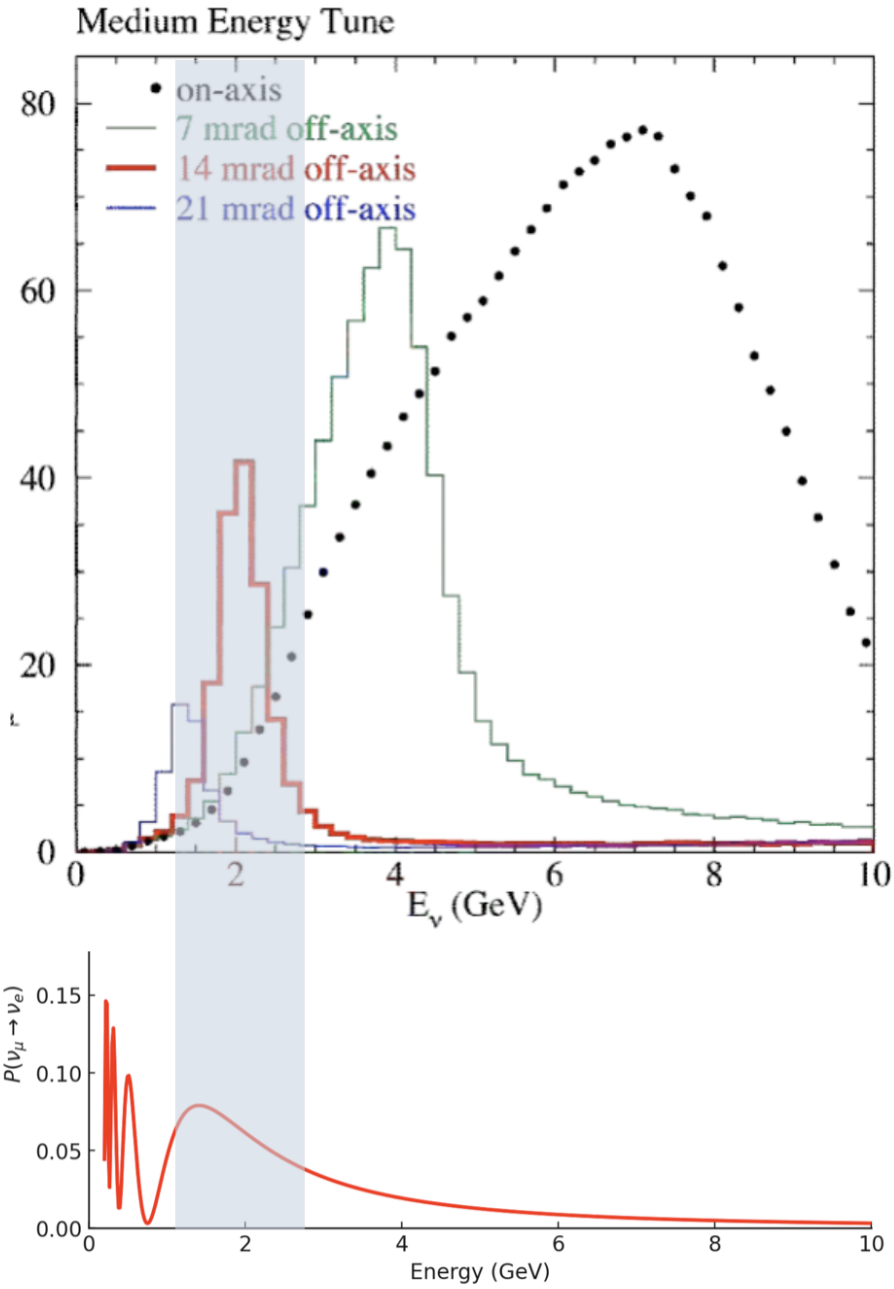

Figure 3.3: Neutrino flux and oscillation probability for different off-axis angles in the NuMI beam. Top panel: neutrino energy spectra at $\theta = 0$ (on-axis), 7 mrad, 14 mrad, and 21 mrad off-axis. Bottom panel: $\nu_\mu \rightarrow \nu_e$ oscillation probability as a function of energy at 810 km for the 14 mrad spectrum. The 14 mrad configuration concentrates the flux near the oscillation maximum at $\sim$2 GeV, optimizing NOvA's appearance sensitivity. Figure adapted from Ref. [22]

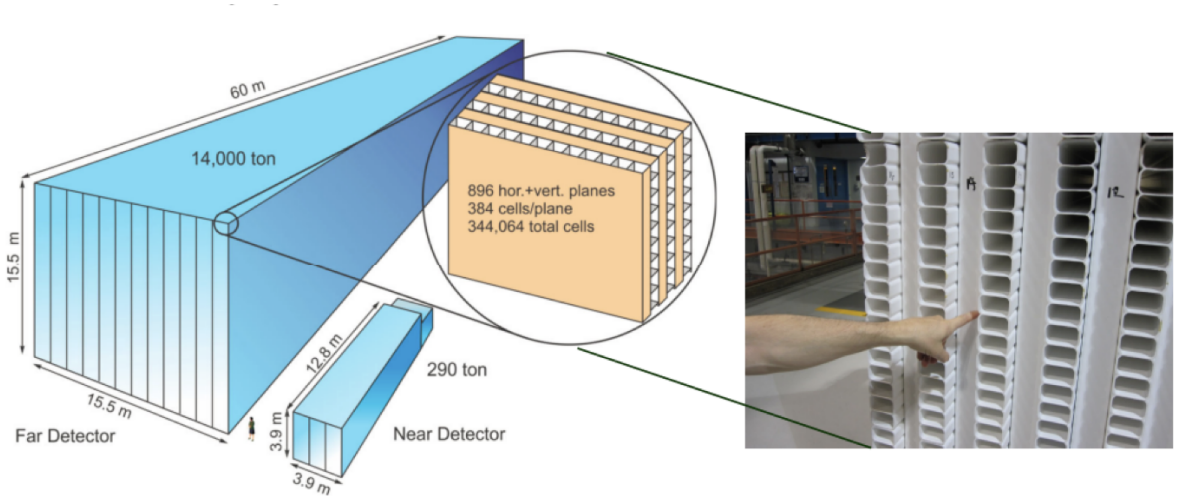

Figure 3.4: Graph showing the relative size difference of NOvA Near Detector and Far Detector. The detectors are consisted with alternating vertical and horizontal planes with stacked cells [22]

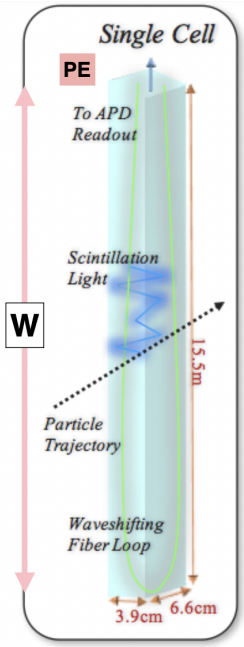

Figure 3.5: Diagram of each cell, filled with liquid scintillator and a wavelength shifting fiber loop. [22]

light shifted from blue light with around 85% efficiency. Signals are recorded when the light from wavelength shifting fiber surpasses a preset threshold when they arrive APD to reduce noise.

3.1.4 The Near Detector

The Near Detector (ND) is located at Fermilab and about 1 km downstream of NuMI beam, 100 m underground [22]. The main purpose of NOvA ND is to measure the un-oscillated neutrinos from the NuMI beam and constrain systematic uncertainties in flux and cross-section model. It contains 290 tons of mineral oil as scintillation material. It shares the same horizontal and vertical alternating cell structure to achieve 2 orthogonal views, front view (Y-Z view) and top view (X-Z view), to achieve 3-D particle track length and energy reconstruction. It does not contribute to the atmospheric neutrino analysis presented in this thesis because atmospheric neutrinos arrive isotopically and do not benefit from near-far detector comparison in the same manner as beam neutrinos. But due to the 100 m underground design, it rejects most of the cosmic background, and has the potential to detect atmospheric neutrinos, as it has activity trigger and could be looked into in future analyses. However, due to the small size transverse to the beam (3.9×3.9 m), muons from atmospheric neutrinos are difficult to contain in the ND, causing poor energy reconstruction.

3.1.5 The Far Detector

The NOvA Far Detector (FD) is one of the largest low-density tracking calorimeters ever constructed. The detector has dimensions of 15.6 m (width) × 15.6 m (height) × 60 m (length) and is situated on the surface at an elevation of 380 m above sea level.

The NOvA FD consists of 896 horizontal planes alternating with 896 vertical planes, with a total of 344,064 extrusion PVC cells. The size of each cell is 3.9 cm ×6.0 cm × 15.5 m and is filled with liquid scintillator.

Figure 3.6: NOvA Near Detector

The liquid scintillator formulation consists of 94.6% mineral oil, 5.0% pseudocumene as a wavelength shifter, and 0.4%PPO (2,5-diphenyloxazole) as a fluor. When charged particles travel through the scintillator, they excite the PPO, which causes ultraviolet light emission. The pseudocumene shifts the UV light to blue-green visible spectrum ~ 420 *nm*, which propagates through the cell and is collected by wavelength shifting fibers.

Unlike most neutrino detectors, which are located deep underground to reduce cosmic ray backgrounds, the NOvA FD is on Earth ground level. This design choice was driven by cost considerations and the relatively narrow energy spectrum of the off-axis beam, which aids in background rejection. However, the surface location presents significant challenges for atmospheric neutrino detection.

The FD is continuously bombarded by cosmic ray muons at a rate of approximately 120 kHz across the entire detector volume [23]. This corresponds to roughly 100,000 cosmic ray muons for every beam neutrino interaction. For atmospheric neutrino analysis, this cosmic ray flux represents an even more severe challenge, as atmospheric neutrino interactions occur at a rate several orders of magnitude lower than beam events and arrive isotropically, making directional cuts less effective.

Figure 3.7: NOvA Far Detector side view

3.2 DUNE

The Deep Underground Neutrino Experiment (DUNE) is a next generation long-baseline neutrino experiment hosted by Fermilab. [24]. Similar to the NOvA experiment, DUNE will also use an intense neutrino beam produced at Fermilab. The DUNE Far Detector is designed as a massive liquid argon time projection chamber (LArTPC) detector 1,300 km away from the neutrino source, located at the Sanford Underground Research Facility (SURF) in Lead, South Dakota. There are three main goals for DUNE: measure CP violation in the neutrino sector, determine mass ordering, and search for physics beyond the Standard Model (BSM). DUNE's LArTPC can resolve deposited energy with few-MeV precision that can detect supernova neutrinos (5-50 MeV), in comparison to NOvA's minimum reconstructed energy around 100-200 MeV. DUNE is currently under construction; the excavation of underground cavities is complete, and detector module construction is beginning. Data collection for the Far Detector will begin in 5 to 10 years.

While DUNE's primary physics program focuses on the Long-Baseline Neutrino Facility (LBNF)

beam, due to its deep underground location and large detector mass, DUNE provides exceptional sensitivity to atmospheric neutrinos, supernova neutrinos, nucleon decay, and other rare event searches. This thesis presents a study of DUNE's sensitivity to nonstandard neutrino interactions using atmospheric neutrino events.

3.2.1 DUNE Near Detector

The DUNE Near Detector (ND) is located 574 m downstream from the neutrino source, 60 m underground [24] The DUNE ND, similar to NOvA ND, is designed to measure the un-oscillated neutrino beam spectrum and contain systematic uncertainties in flux and cross-section models for the long baseline oscillation analyses.

The ND complex consists of multiple detector components with different physics measurement purposes.

- **ND-LAr**: A 67 ton liquid argon TPC that consists of 35 LArTPCs with similar technology to the Far Detector, enabling direct comparison of event topologies and energy reconstruction
- **ND-GAr**: A high pressure gaseous argon TPC surrounded by an electromagnetic calorimeter, with enhanced reconstruction of low-energy particles
- **SAND** (System for on-Axis Neutrino Detection): An on-axis detector that is magnetized by 0.6 T superconducting magnet for neutrino spectrum monitoring.

3.2.2 DUNE Far Detector

The DUNE Far Detector (FD) will be located 1300 km away from the neutrino source in SURF. It is 1,478 m deep underground which allows the rock overburden to reduce cosmic ray background from the surface level of 165 kHz [24]. The overburden will reduce the cosmic ray muon flux by approximately six orders of magnitude compared to the surface. This underground location is

crucial for atmospheric neutrino measurements because it dramatically decreases background that would otherwise overwhelm the atmospheric neutrino signal and cause very low signal purity.

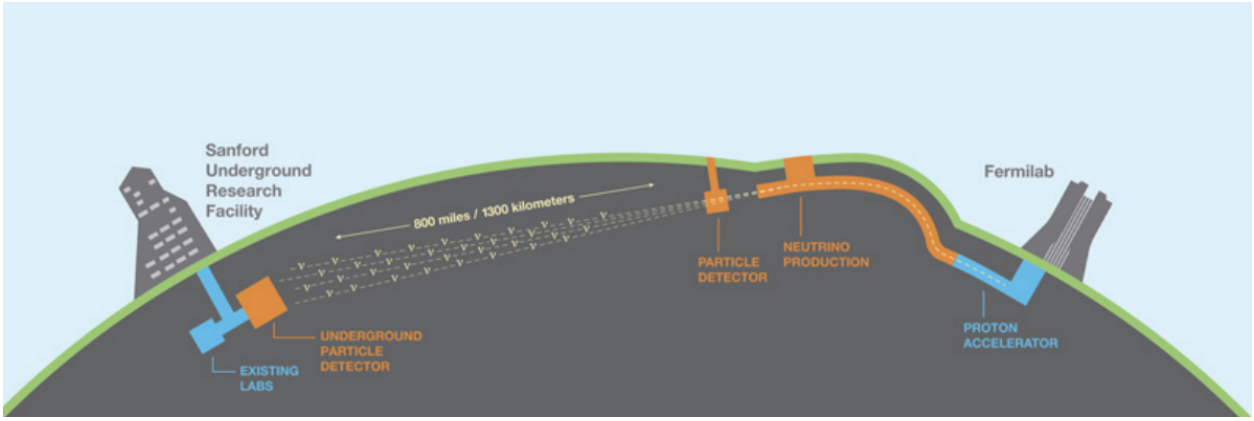

Figure 3.8: The plot shows the setup of DUNE experiment layout. The neutrino source is on the right hand side located at Fermilab. The neutrino beam travels 1300 km to Sanford Underground Research Facility (SURF) on the left hand side. Neutrinos will travel through Earth and reach SURF from Fermilab [24]

3.2.3 Modular LArTPC Design

The DUNE Far Detector is designed as a modular system consisting of four independent LArTPC cryostat detector modules, each with a fiducial mass of approximately 10 kilotons of liquid argon [25]. When fully built, the DUNE FD will have a fiducial mass of 40 kilotons. Instead of constructing one giant detector all at once, the DUNE FD is divided into four separate modules. This modular approach has several benefits: it allows the experiment begin taking data earlier as each module is completed. It also reduces technical risk by avoiding the need to build an extremely large single detector. It also gives flexibility to test different technology in different modules.

Each detector module is housed in a cryostat measuring approximately 15.1 m (width) $\times$ 14.0 m (height) $\times$ 62.0 m (length), containing approximately 10 kilotons of liquid argon total mass [24]. The first two modules will use a horizontal drift single-phase TPC design (Fig. 3.9), while later modules may employ vertical drift or dual-phase technologies.

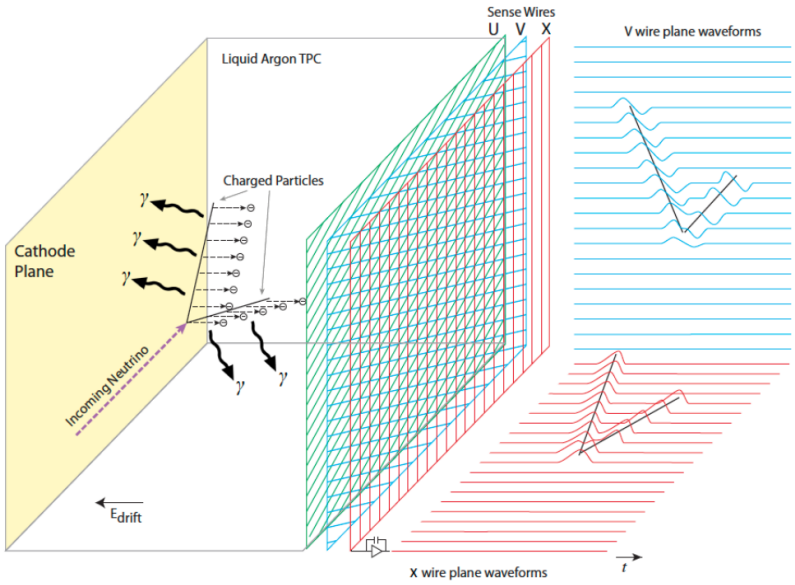

Figure 3.9: Horizontal drift diagram in SP LArTPC. Ionization electrons from the neutrino interaction drift horizontally to the right due to electric field. The electrons will reach the anode, where there are three layers of sensing wires, named U, V and X. [24]

3.2.4 Single Phase Horizontal Drift TPC

DUNE's atmospheric neutrinos are simulated using the single phase horizontal drifting TPC design in this thesis. It operates entirely inside liquid argon phase. The detector volume is divided into drift regions by cathode plane assemblies (CPAs) positioned at the center and edges of the cryostat. Anode plane assemblies (APAs) are positioned at the boundaries of each drift region, allowing a drift distances of up to 3.6 m.

When a charged particle traverses the liquid argon, it ionizes argon atoms along its path, freeing electrons. The electric field ($\sim 500V/cm$) then pushes these ionization electrons to drift horizontally toward the APAs at around 1.6 mm/μs. The APAs consist of 3 layers of sensing wires oriented in 3 different directions as shown in Fig 3.9 which are (0°, ±35.7° relative to vertical) and they collect and measure the drifting charge to provide three two-dimensional projections that allow full three-dimensional reconstruction.

Liquid argon is an excellent detection medium for neutrinos thanks to its high density (1.4 g/cm^3)

and its ability to record interactions with high energy resolution. It provides sub-millimeter tracking resolution [24] and achieves a few-percent calorimetric energy resolution for electromagnetic showers. These capabilities allow detailed reconstruction of interaction topologies and energy deposition patterns, enabling robust particle identification, such as separating electrons from photons and distinguishing muons, pions, and protons from other hadronic activity.

3.2.5 Atmospheric Neutrino Simulation Geometry

The atmospheric neutrino analysis presented in this thesis is based on Monte Carlo simulations of neutrino interactions in a reduced 1×2×6 detector geometry representing a single DUNE detector module [24]. This reduced geometry represents a subset of a single module's active volume, with dimensions scaled down by factors in each direction while preserving the essential detector response characteristics. When scaled to full dimensions, this corresponds to one 10-kiloton fiducial mass LArTPC module, representing one-quarter of the eventual full DUNE Far Detector, which will consist of four modules totaling 40 kton fiducial mass.

The atmospheric neutrino event selection used in this analysis is restricted to reconstructed neutrino energies below approximately 10 GeV. This energy cutoff arises from the single-module geometry and event containment requirements. Higher energy neutrino interactions produce more energetic secondary particles like muons with longer tracks in liquid argon. For neutrino energies exceeding 10 GeV, the resulting muons and hadronic showers frequently exit the boundaries of a single 10-kton module, leading to incomplete energy reconstruction and reduced selection efficiency. By restricting the analysis to sub-10 GeV events, reliable containment and accurate energy measurement are ensured within the single-module volume.

The events simulated in the reduced single-module geometry are scaled to represent the full DUNE Far Detector configuration operating for 10 years. The complete detector consists of four independent modules, each with 10 kton liquid argon fiducial mass using the horizontal drift single phase design, providing 40 kton total fiducial mass. The total integrated exposure assumed for this

analysis is 400 kton-years.

The scaling procedure accounts for two factors. First, geometric scaling from the 1×2×6 reduced geometry to the full single module volume accounts for the dimensional reduction in the simulation. Second, multiplicative scaling by a factor of four represents the four independent modules collecting events simultaneously over the 10-year period.

This scaling approach is valid because atmospheric neutrinos arrive isotropically from all directions and interact independently in each detector module. Each neutrino interaction is localized to a single point, with secondary particles contained within one module's volume. The four-module configuration increases the total event rate by a factor of four compared to a single module, while individual event topologies and reconstruction remain confined to single-module volumes. This approach provides a realistic projection of DUNE's atmospheric neutrino sensitivity while maintaining computational efficiency in the simulation and reconstruction stages.

Chapter 4

Signatures of Non-Standard Interactions (NSI) in NOvA and DUNE

4.1 Introduction

As described in section 2.7, non-standard interactions modify the effective matter potential that atmospheric neutrinos experience when they travel through the Earth. This chapter demonstrates the observable signatures of non-standard interactions (NSI) in atmospheric neutrino Monte Carlo simulations, showing how different NSI parameters produce distinct patterns in the L/E vs zenith angle distribution relevant for NOvA and DUNE analyses.

All NOvA oscillation probability calculations in this chapter are performed using the OscProb package [26], a C++ framework for computing neutrino oscillation probabilities in matter with varying density profiles. OscProb calculates numerical solutions to the neutrino oscillation equations, accounting for Earth's layered density structure using the Preliminary Reference Earth Model (PREM) [27]. DUNE uses MaCH3 [28] and NuOscillator [29], which provides a modular interface to engines that uses the same OscProb package.

4.2 Oscillogram Representation

4.2.1 Definition and Interpretation

An **oscillogram** refers to a two-dimensional map of the neutrino oscillation probability $P_{\alpha\beta}(L/E_\nu, \cos\theta_{zenith})$, computed over a grid of neutrino baseline-to-energy (L/E_ν) and zenith angle cosθ, as shown in Fig. 4.2 for the Standard Interaction case. The quantity L is the path length through the Earth, which depends on the zenith angle and the Earth's radius, together with atmospheric neutrino production height, which is chosen to be 15 km above Earth's surface (see Fig. 4.1). The atmospheric neutrino baseline L is calculated from zenith angle θ_z by Eqn. 4.1

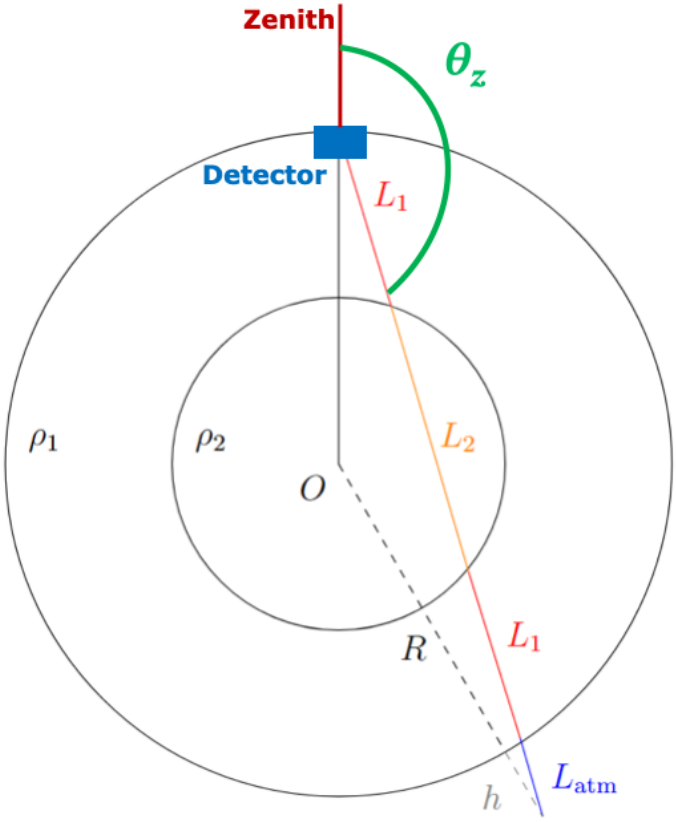

Figure 4.1: Zenith angle to neutrino baseline L calculation. R is radius of earth, h is atmospheric neutrino production height, O represents Earth center. L_1 and L_2 represents distance of travel through Earth mantle (with ρ_1) and core (ρ_2) respectively . θ_z is the zenith angle. [30]

$$L_{tot} = \sqrt{(R+h)^2 - R^2\ sin^2(\pi - \theta_z)} + R\ cos(\pi - \theta_z) \tag{4.1}$$

where R is Earth's radius, h is atmospheric neutrino production height, typically 15 km above Earth surface. θ_z is the neutrino zenith angle.

L/E is used because the oscillation phase is proportional to

$$\phi_{osc} = \frac{\Delta m^2 L}{4E} \approx 1.27 \frac{\Delta m^2[\mathrm{eV}^2] \cdot L[\mathrm{km}]}{E[\mathrm{GeV}]} \tag{4.2}$$

Oscillation features (maximum and minimum) appear at fixed values of L/E regardless of how energy and zenith angle vary individually. Hence, it gives the oscillogram vertical line feature.

Figure 4.2 shows the oscillation probability across the complete zenith angle range, from downward going ($\cos\theta_{zenith}$ +1, vertical from above the detector) to upward coming ($\cos\theta_{zenith}$ -1, vertical from below the detector).

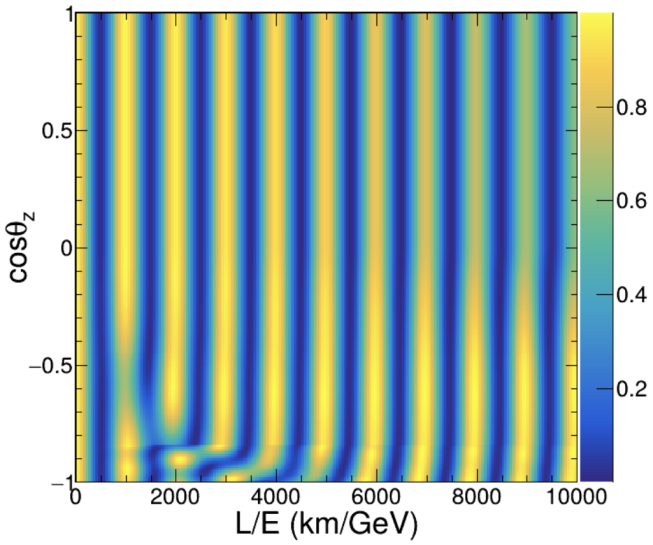

Figure 4.2: Oscillation probability for P($\nu_\mu \rightarrow \nu_\mu$) for Standard Interaction, across full zenith angle range. The stark contrast between downward-going ($\cos\theta_{zenith} > 0$, top half) and upward-going ($\cos\theta_{zenith} < 0$, bottom half) regions demonstrates why atmospheric NSI analyses focus on upward-going events.

The alternating blue (disappearance) and yellow (survival)vertical bands reflect the periodic nature of neutrino oscillation in vacuum. The first minimum appears at around L/E = 500 km/GeV, followed by L/E $\approx$ 1500, 2500, 3500, etc.

The pattern is not symmetrical between upward and downward directions. Especially visible at large L/E, is caused by matter effect in Earth, because neutrinos and anti-neutrinos experience opposite matter potentials, and the long baselines through dense Earth matter causes noticeable deviation from vacuum oscillation.

The most attractive and striking deviation from simple vertical band structure appears at $\cos\theta_{zenith}$ < -0.5 and L/E < 5000 km/GeV. In this region, the regular oscillation pattern breaks down, and develops a sophisticated interference structure that creates a distinctive "kink" or distortion. This feature is not a bug or an artifact, but is the fundamental signature of Earth's internal structure instead.

This distortion appears because neutrinos in this zenith angle range traverse both Earth's mantle ($\rho \approx 4.5 g/cm^3$) and the outer core ($\rho \approx 10 g/cm^3$), crossing the core-mantle boundary at the depth of around 2900 km. The sudden density change at this boundary, almost a factor of 2 increase, creates a matter potential "shock", and is apparent in the oscillation probability. For certain combinations of zenith angle and energy, the oscillation probability amplitudes in these two density regimes interfere constructively or destructively, creating this pattern.

This distortion makes the core-crossing region particularly interesting for NSI searches. If NSI parameters modify the matter potential, they will change both the oscillation amplitude, but also the specific interference pattern created at this core-mantle boundary.

4.3 NSI Signature in Atmospheric Neutrino Observables

This analysis measures two observables: electron-like events (final state $\nu_e CC$ interactions) and muon-like events (final state $\nu_\mu CC$ interactions). Each observable receives contributions from

multiple oscillation channels, and different NSI parameters affect these channels differently.

4.3.1 Dominant Channel: Muon Disappearance P$(\nu_\mu \to \nu_\mu)$

The ν_μ survival channel dominates atmospheric statistics and is most sensitive to the $\mu - \tau$ sector NSI. Figure 4.3 shows the ratio of NSI/SI for three representative $\mu - \tau$ sector parameters. The

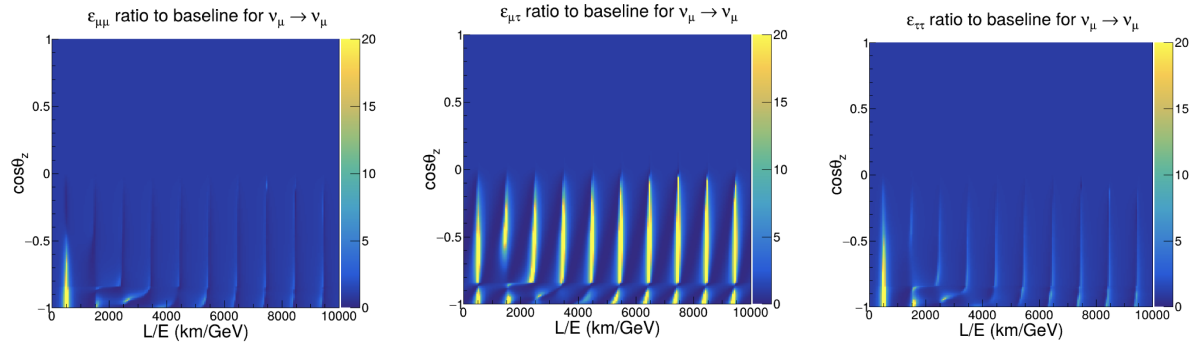

(a) $\varepsilon_{\mu\mu} = 0.25$ (b) $\varepsilon_{\mu\tau} = 0.25$ (c) $\varepsilon_{\tau\tau} = 0.25$

Figure 4.3: Representative NSI/SI ratios for P$(\nu_\mu \to \nu_\mu)$ with $\mu - \tau$ sector parameters at $\varepsilon = 0.25$. Ratio = 1 (blue) indicates no NSI effect. The off-diagonal $\varepsilon_{\mu\tau}$ produces the most distinctive signature with systematic 40-60% deviations showing strong L/E structure.

three $\mu - \tau$ sector parameters show distinct phenomenology:

$\varepsilon_{\mu\mu}$ **(left):** The diagonal muon NSI suppresses the oscillation probability across most of the upward-going region. The ratio drops to 0.2-0.5 (blue) in much of the phase space, with only narrow vertical bands at low L/E staying near 1. This broad suppression makes $\varepsilon_{\mu\mu}$ hard to separate from simple normalization uncertainties.

$\varepsilon_{\mu\tau}$ **(center):** The off-diagonal μ-τ NSI produces the most distinctive signature. The ratio alternates between strong enhancement (yellow bands, ratio $\sim$10-20) and suppression (blue, ratio $\sim$0.5-2). This shifts where the oscillation peaks and dips occur in L/E, creating variations by factors of 10-20 across the plot. These large, structured changes make $\varepsilon_{\mu\tau}$ potentially the easiest parameter to constrain.

$\varepsilon_{\tau\tau}$ **(right):** The diagonal tau NSI falls between $\varepsilon_{\mu\mu}$ and $\varepsilon_{\mu\tau}$. It's mostly suppressed (blue,

ratios 0.5-2) but keeps some of the vertical band structure at low-to-intermediate L/E. The suppression is weaker than $\varepsilon_{\mu\mu}$, with ratios usually staying above 0.5.

The color scale goes up to 20, showing that NSI can change the oscillation probability by more than an order of magnitude in some regions. However, these large ratios often appear where the baseline probability is already limited and near oscillation minimum, so the actual change in event rate is more moderate.

4.3.2 Electron Survival: P($\nu_e \to \nu_e$)

Electron neutrino channels contribute with lower statistics due to the smaller atmospheric ν_e flux (only 1/2 of ν_μ flux), however, these channels do provide important complementary information, especially for constraining electron sector NSI parameters that affect ν_μ disappearance.

Figure 4.4 shows representative examples from electron neutrino channels.

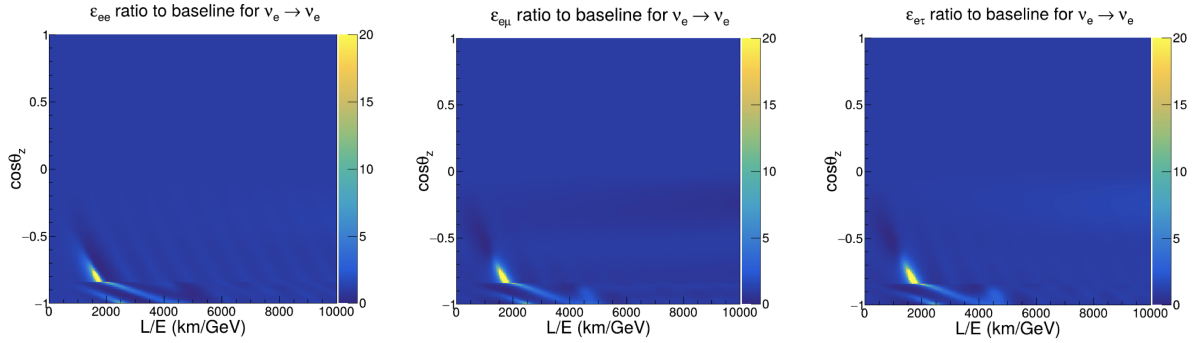

(a) $\varepsilon_{ee} = 0.25$ (b) $\varepsilon_{e\mu} = 0.25$ (c) $\varepsilon_{e\tau} = 0.25$

Figure 4.4: NSI/SI ratios for electron neutrino channels at $\varepsilon = 0.25$. Ratio = 1 (blue) indicates no NSI effect. Electron sector NSI directly modifies these probabilities, providing sensitivity that's unavailable from ν_μ disappearance alone.

All three electron sector parameters produce similar effects on ν_e survival at $\varepsilon = 0.25$. The ratio is strongly suppressed (dark blue, ratio near 0) across most of the upward-going region. NSI effects are concentrated in a narrow "hotspot" at steep upward angles ($\cos\theta_z \sim$ -0.7 to -0.9) and low L/E (1000-2000 km/GeV), where the ratio can reach 10-20.

The μ-τ sector parameters ($\varepsilon_{\mu\mu}$, $\varepsilon_{\mu\tau}$, $\varepsilon_{\tau\tau}$) show essentially identical patterns in P($\nu_e \to \nu_e$), with the same localized hotspot and broad suppression elsewhere. This similarity across all six NSI parameters indicates that ν_e survival provides weak discrimination between different NSI scenarios at this coupling strength.

4.3.3 Electron-to-Muon Appearance: P($\nu_e \to \nu_\mu$)

The appearance channel reveals much more distinctive NSI signatures. Figure 4.5 shows representative examples.

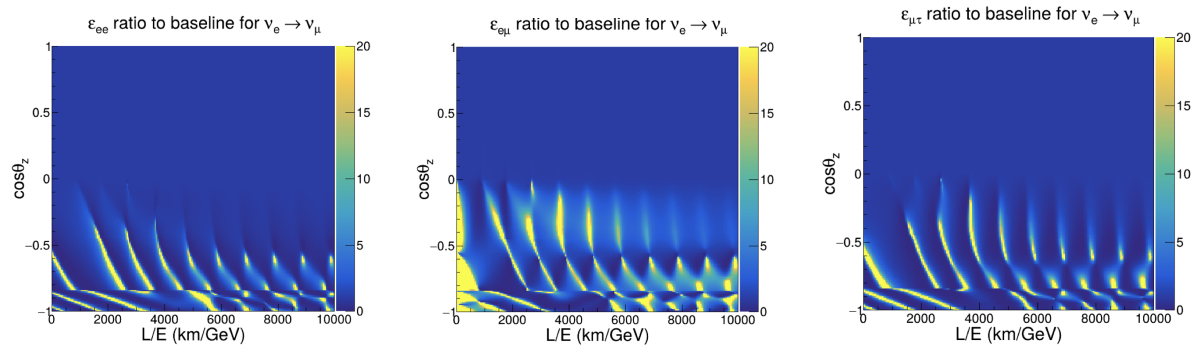

(a) $\varepsilon_{ee} = 0.25$ (b) $\varepsilon_{e\mu} = 0.25$ (c) $\varepsilon_{\mu\tau} = 0.25$

Figure 4.5: NSI/SI ratios for P($\nu_e \to \nu_\mu$) appearance. Unlike ν_e survival, this channel shows distinctive diagonal band patterns with large enhancements (ratio ∼10-20) that vary across parameters.

The rich structure in P($\nu_e \to \nu_\mu$) makes this channel particularly valuable for discriminating between NSI parameters, complementing the strong μ-τ sector sensitivity from ν_μ disappearance.

4.4 Event Rate Predictions with NSI

The oscillation probability with NSI effects translates into observable changes in event rates. NSI modified oscillation probabilities are applied to atmospheric neutrino Monte Carlo samples for NOVA to predict how NSI would affect the measured event distribution in energy, zenith angle, and L/E.

4.4.1 Two-Dimensional Event Distributions

Figure 4.6 shows predicted event distributions in the $\cos\theta_z$ vs L/E plane for final-state muon-like events (ν_μCC interactions) under standard oscillations and with NSI. For more obvious event rate distinction, I set the NSI parameter at 0.5, one at a time.

The largest deviation is around $\cos\theta_z < 0$ and L/E between 500 km/GeV and 5000 km/GeV, where vertical stripe pattern is visible to eye.

The raw event distribution in the top panels appear nearly identical by eye, despite the NSI modification to oscillation probabilities. This similarity arises because NSI is a rather weak effect, and it only shifts the oscillation probability marginally. The relative difference plot in the bottom panel shows the NSI signature more clearly by normalizing out the large dynamic range in event rates across the phase space. A similar effect can also be found for setting $\varepsilon_{\mu\tau}$ to 0.5, as shown in Fig. 4.7. But this pattern is less significant for diagonal NSI parameters including ε_{ee}, $\varepsilon_{\mu\mu}$ and $\varepsilon_{\tau\tau}$, for example, Fig. 4.8

The final ν_e events are a lot less significant for NSI effect.For example, figure 4.9 shows the corresponding distribution for electron-like events (ν_eCC interactions).

4.4.2 L/E Spectra

Projecting the two-dimensional distributions onto the L/E axis (integrating over all zenith angles) shows how NSI modifies the true L/E spectrum. Figure 4.10 shows energy distributions for several NSI parameters. As expected, ν_μ final state particles show significantly more change in event rate compared to that of ν_e final state event rate, particularly at regions where fig. 4.7 the vertical stripes are located. However, by projecting onto L/E axis, I am integrating over all zenith angles which averages out angular dependent features. Since NSI effects vary with zenith angle (upward going neutrinos traverse more Earth matter and longer baselines than downward going neutrinos), this angular averaging reduces the visible NSI signature. I expect stronger NSI sensitivity from

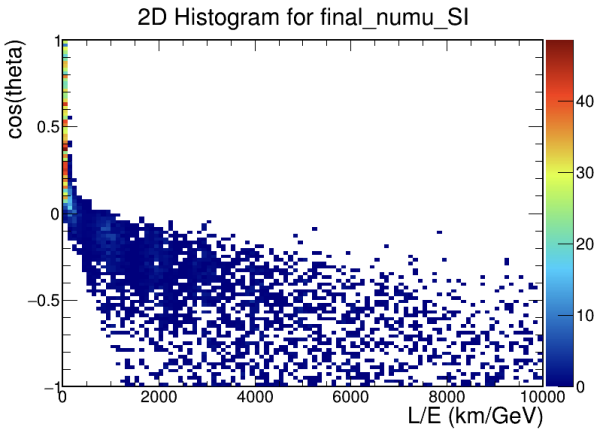

(a) Standard Oscillations

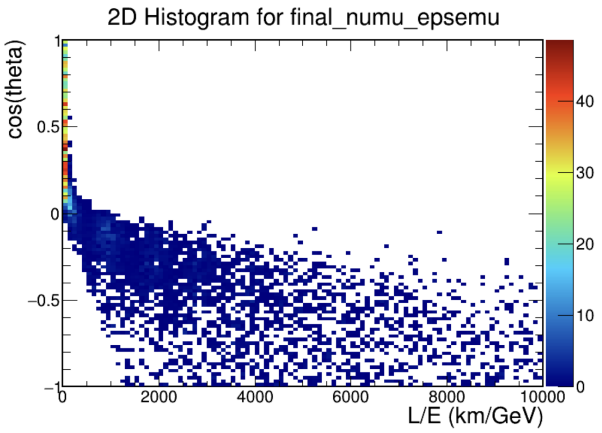

(b) With NSI: $\varepsilon_{e\mu} = 0.5$

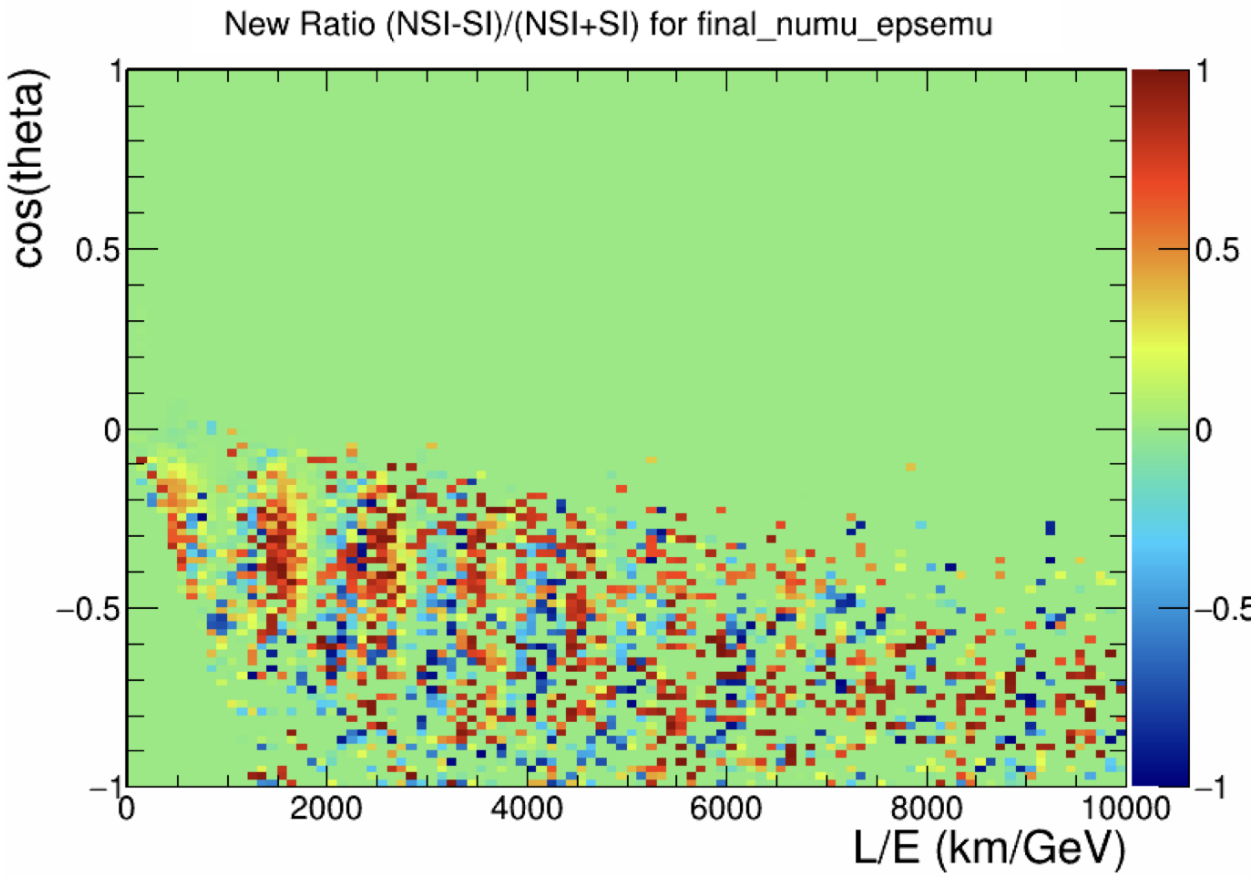

(c) Relative difference: (NSI-SI)/(NSI+SI)

Figure 4.6: Predicted muon-like event distributions with and without NSI. The top panels show absolute event counts in each bin, which appear visually similar. The bottom panel shows the relative difference, revealing where NSI modifies the expected event rates.

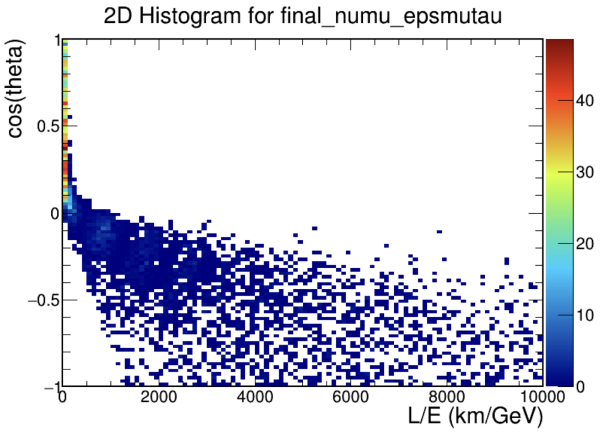

(a) With NSI: $\varepsilon_{\mu\tau} = 0.5$

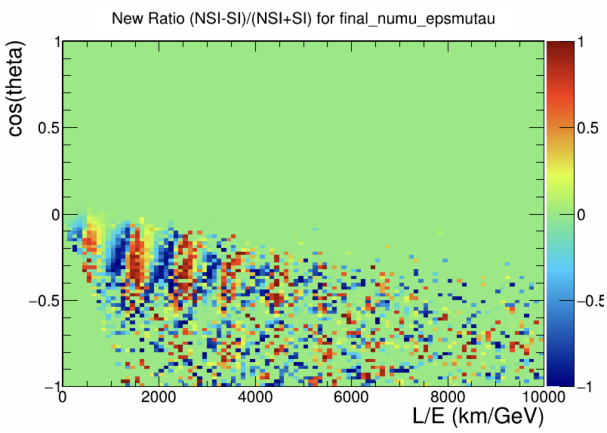

(b) With NSI: $\varepsilon_{\mu\tau} = 0.5$

Figure 4.7: Predicted muon-like event distributions with NSI parameter $\varepsilon_{\mu\tau} = 0.5$.. The left panels show absolute event counts in each bin, which appear visually similar to the event rate without NSI. Right panel shows the relative difference, revealing where NSI modifies the expected event rates.

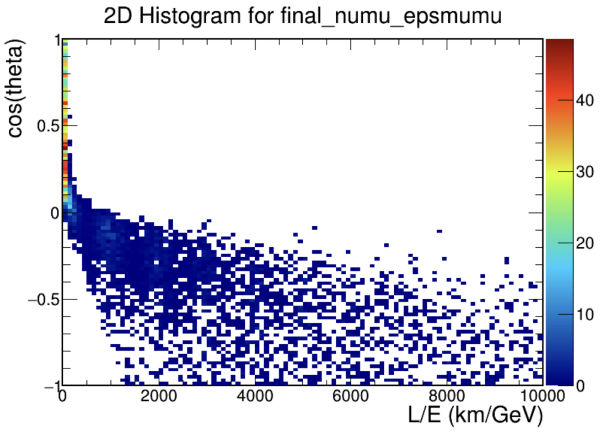

(a) With NSI: $\varepsilon_{\mu\mu} = 0.5$

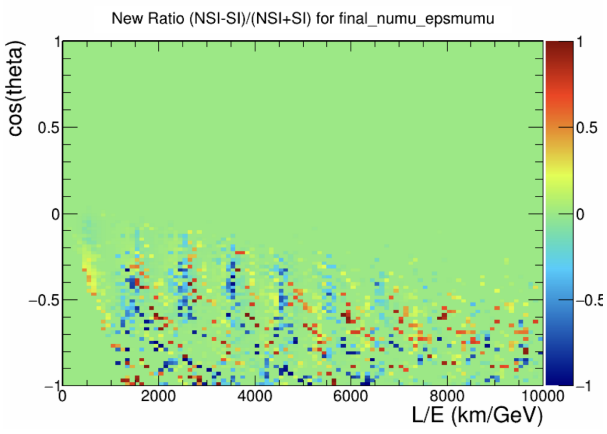

(b) With NSI: $\varepsilon_{\mu\mu} = 0.5$

Figure 4.8: Predicted muon-like event distributions with NSI parameter $\varepsilon_{\mu\mu} = 0.5$.. The left panels show absolute event counts in each bin, which appear visually similar to the event rate without NSI. Right panel shows the relative difference, revealing where NSI modifies the expected event rates.

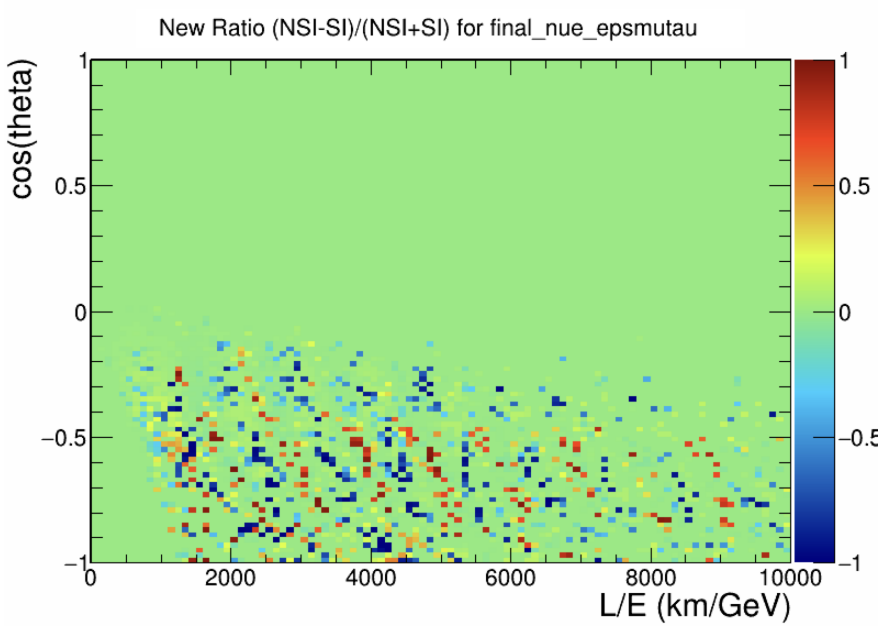

Figure 4.9: Relative difference (NSI-SI)/(NSI+SI) for electron-like events with $\varepsilon_{\mu\tau} = 0.5$. The vertical stripes for ν_μ final state ratio is a lot less significant here

upward going atmospheric neutrinos ($\cos\theta < 0$) , but this information is lost in the angle integrated projection.

4.4.3 Angular Slicing: Energy vs L/E Projections

To reveal angular dependent NSI signatures, we examine event distributions in four zenith angle slices. However, there is a choice of which kinematic variable to project onto: true energy E or the oscillation variable L/E.

Energy Projections with Angular Slicing

Figure 4.11 and Fig 4.12 shows energy distributions in four angular slices for $\varepsilon_{e\mu} = 0.5$ and $\varepsilon_{\mu\tau} = 0.5$.

To better distinguish angular-dependent NSI effects, Figure 4.13 and Figure 4.14 shows energy projection in four zenith angle bins:

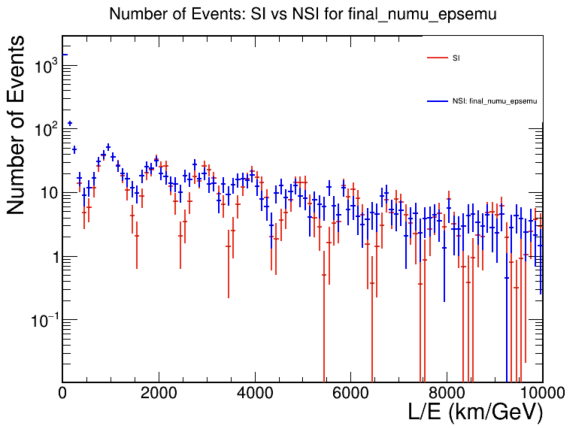

(a) Final ν_μ: $\varepsilon_{e\mu} = 0.5$

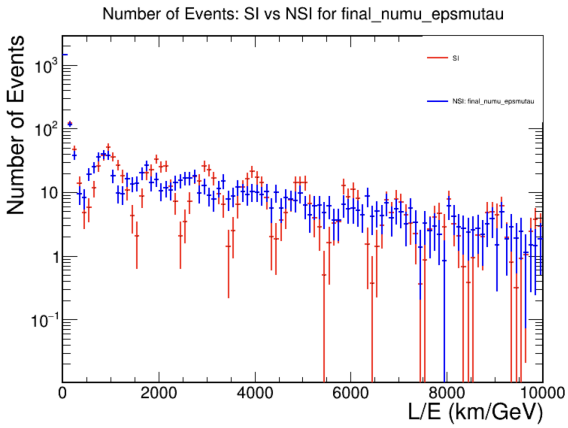

(b) Final ν_μ: $\varepsilon_{\mu\tau} = 0.5$

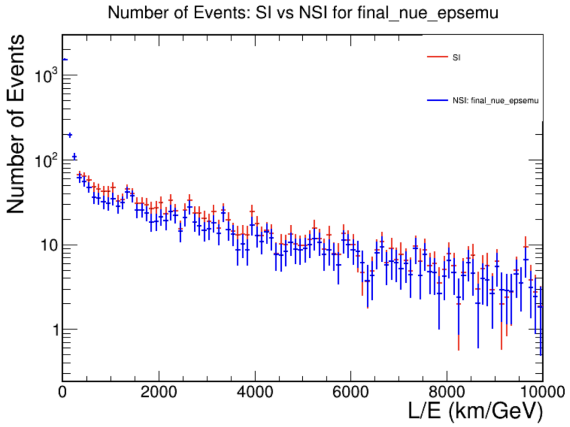

(c) Final ν_e: $\varepsilon_{e\mu=0.5}$

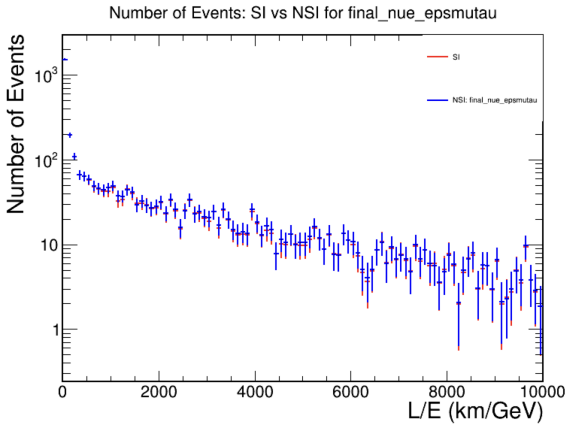

(d) Final ν_e: $\varepsilon_{\mu\tau} = 0.5$

Figure 4.10: L/E spectra comparing standard oscillations (red) to NSI predictions (blue) for representative NSI parameters at $\varepsilon = 0.5$. Top panels are for ν_μ final states, and bottom panels are for ν_e final states

- Slice 1: $0.5 \leq cos\theta \leq 1$ - Downward-going neutrinos with short atmospheric baselines
- Slice 2: $0 \leq cos\theta \leq 0.5$ - Near-horizontal neutrinos with intermediate baselines
- Slice 3: $-0.5 \leq cos\theta \leq 0$ - Upward-going neutrinos traversing the Earth
- Slice 4: $-1 \leq cos\theta \leq -0.5$ - Steeply upward-going neutrinos with maximum Earth traversal

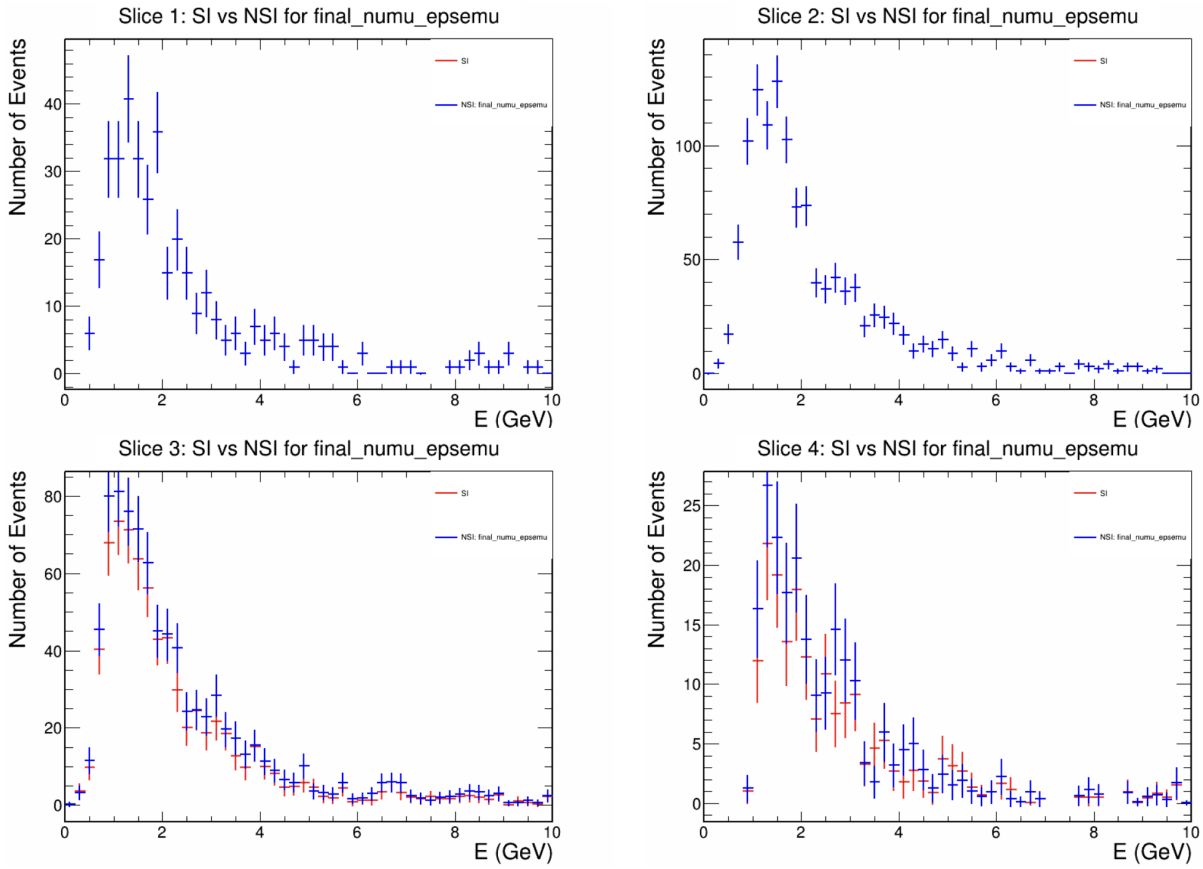

Figure 4.11: Energy spectra in four zenith angle bins for ν_μ final state events, comparing SI (red) to NSI (blue). $\varepsilon_{e\mu} = 0.5$

The energy projection distributes events more evenly across angular bins. Slices 1 and 2 (downward and horizontal neutrinos) contain few events and show essentially no NSI signature (SI and NSI completely overlap), as expected for short baselines where oscillations are minimal. This

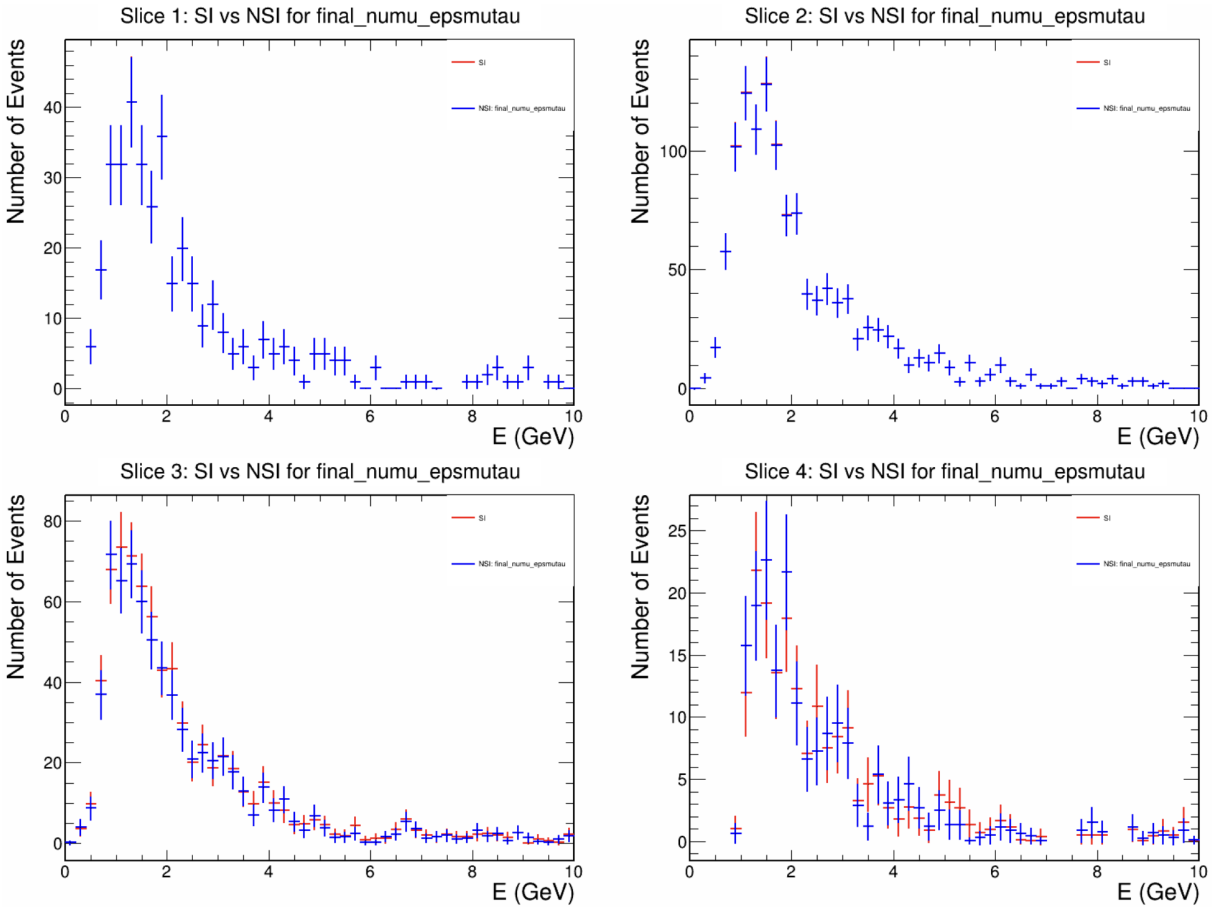

Figure 4.12: Energy spectra in four zenith angle bins for ν_μ final state events, comparing SI (red) to NSI (blue). $\varepsilon_{\mu\tau} = 0.5$

demonstrates a limitation of energy projections for revealing NSI signatures for downward-going atmospheric neutrinos.

Slices 3 and 4 (upward-going neutrinos) dominate the statistics. For $\varepsilon_{\mu\tau}$ (bottom panels), Slice 3 shows visible NSI effects with the blue (NSI) distribution systematically below red (SI) at energies E $\sim$ 1-4 GeV. Slice 4 shows similar but weaker effects. However, the NSI signature is subtle in energy space because neutrinos at the same energy but different angles correspond to different L/E values and thus different oscillation phases.

Corresponding angular slices for ν_e final state events (not shown) display even weaker NSI signatures due to both lower statistics (200 events vs 860 for ν_μ) and the smaller NSI sensitivity of electron channels discussed in Section 4.3. The ν_μ final sample provides the dominant constraining power for μ-τ sector NSI parameters.

4.4.4 L/E Projections with Angular Slicing

Figure 4.13 and Figure 4.14 show the same angular slices but projected onto L/E instead of energy.

- slice 1 & 2 (downward/horizontal): The event rates for SI and NSI are essentially identical
- slice 3 (upward): show clear NSI effect with oscillation structure
- slice 4 (steep upward): maximum NSI effect due to long baseline and matter effects, but limited by statistics

The angular dependence of NSI sensitivity arises because upward going neutrinos travel through more Earth matter with longer baselines, experiencing larger matter-enhanced NSI effects. The most constraining sensitivity comes from $\theta \geq 90$ ($\cos\theta \leq 0$), where NSI modifications are strongest. Slices 1 and 2 contain primarily downward and horizontal neutrinos with minimal NSI effects, while Slices 3 and 4 capture the upward-going population where NSI signatures are most visible. Figure 4.15 and 4.16 show the corresponding angular slices for ν_e final state events.

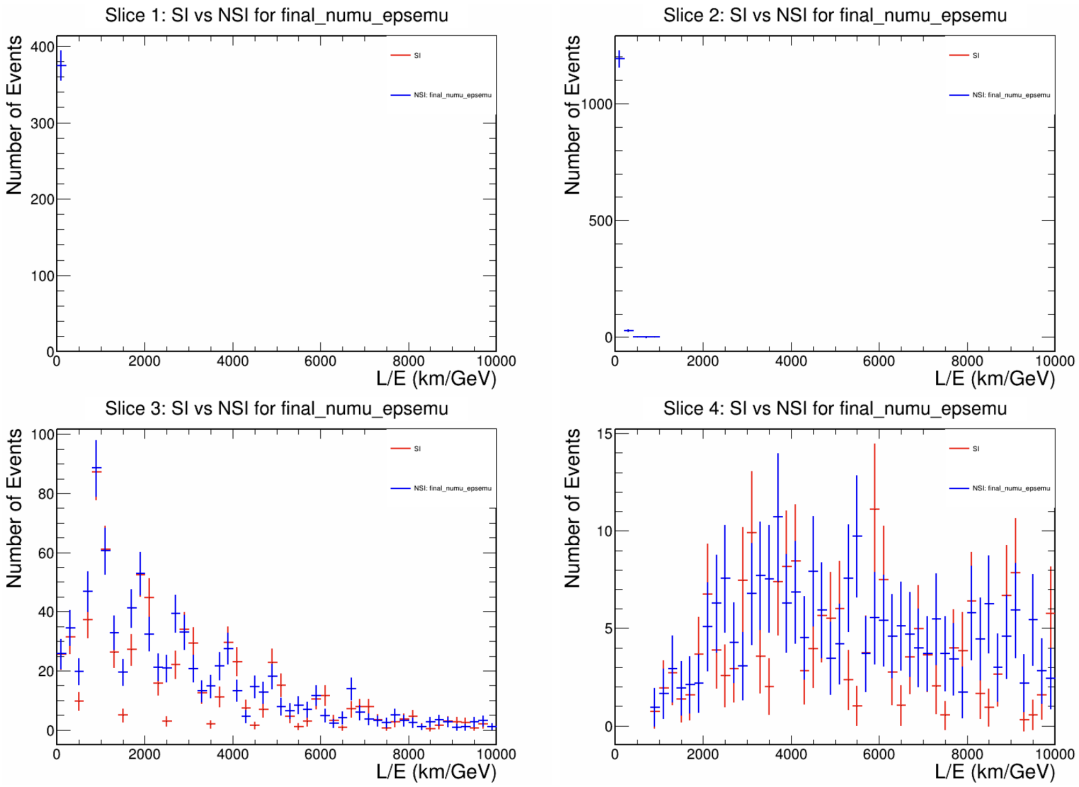

Figure 4.13: L/E spectra in four zenith angle bins for ν_μ final state events, comparing SI (red) to NSI with $\varepsilon_{e\mu} = 0.5$ (blue). Each panel shows a different angular range, revealing how NSI effects vary with neutrino trajectory through the Earth.

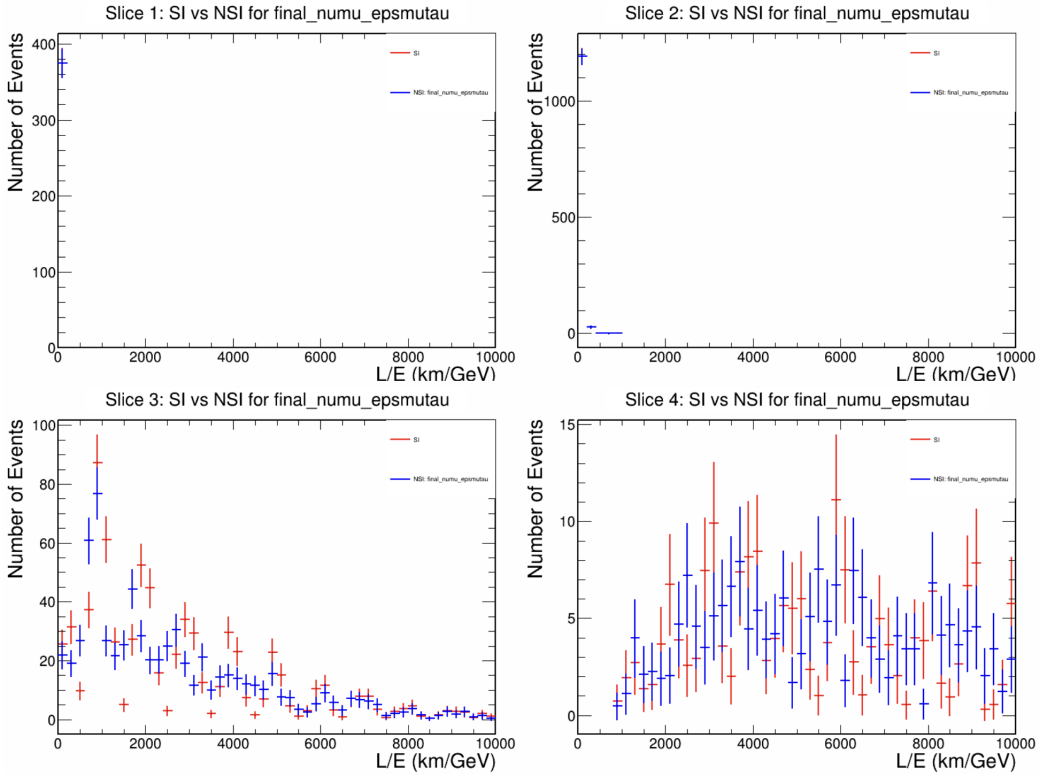

Figure 4.14: L/E spectra in four zenith angle bins for ν_μ final state events with $\varepsilon_{\mu\tau} = 0.5$. The angular slicing reveals where NSI modifications are strongest.

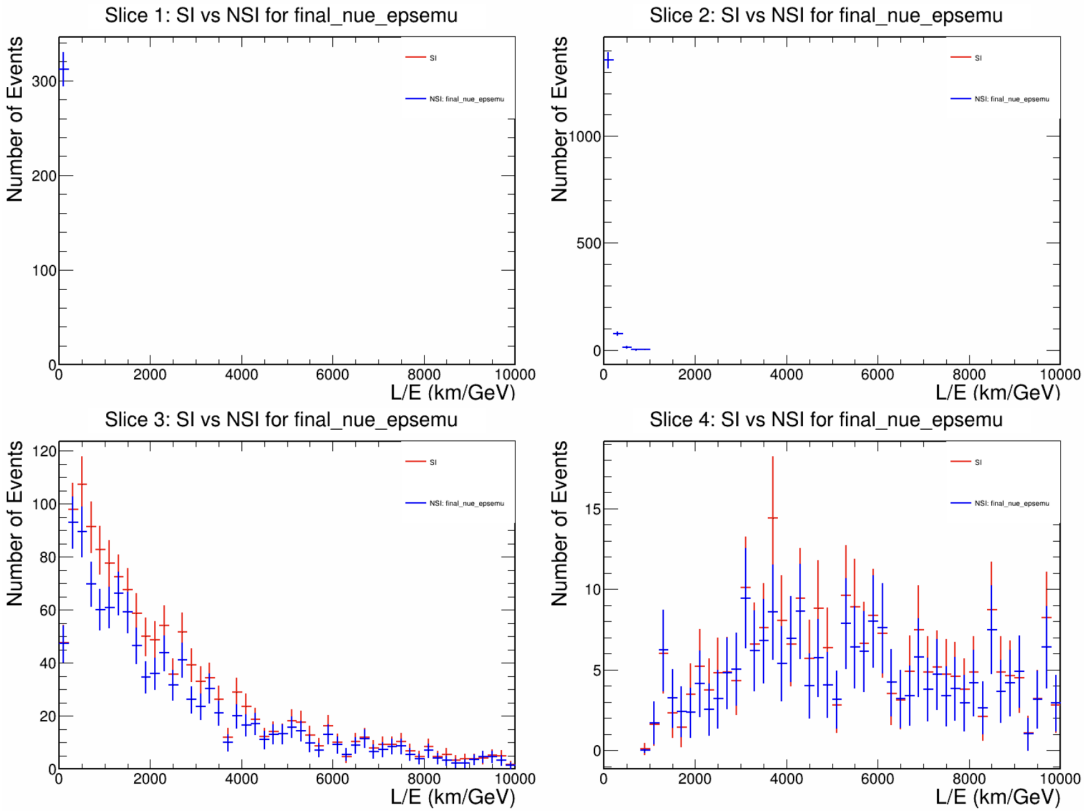

Figure 4.15: L/E spectra in four zenith angle bins for ν_e final state events, comparing SI (red) to NSI with $\varepsilon_{e\mu} = 0.5$ (blue). Each panel shows a different angular range, revealing how NSI effects vary with neutrino trajectory through the Earth.

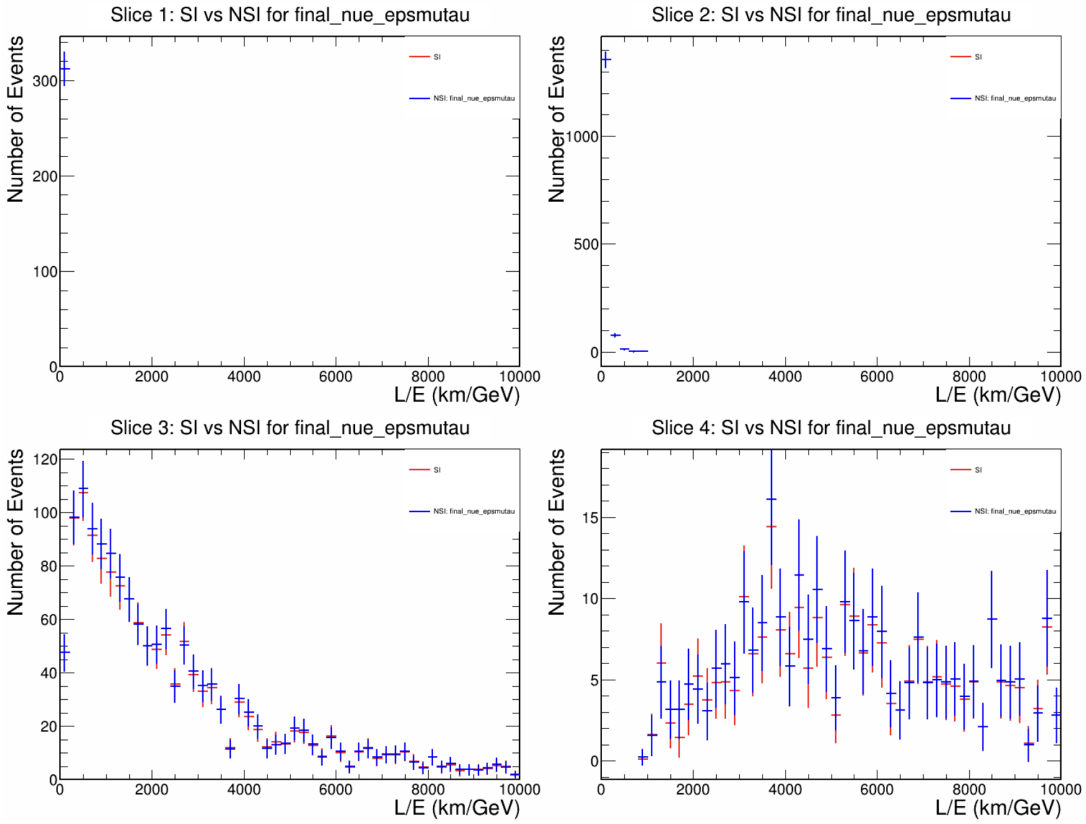

Figure 4.16: L/E spectra in four zenith angle bins for ν_e final state events with $\varepsilon_{\mu\tau} = 0.5$. The angular slicing reveals where NSI modifications are strongest.

- slice 1 & 2 (downward/horizontal): The event rates for SI and NSI are essentially identical
- slice 3 (upward): show clear NSI effect with oscillation structure under 4000 km/GeV
- slice 4 (steep upward): maximum NSI effect due to long baseline and matter effects, but limited by statistics

Tradeoffs and Analysis Strategy

The choice between energy and L/E projection involves a tradeoff, as energy projections are easier to interpret in terms of detector response, but they don't show NSI effect signatures due to mixing of oscillation phases. L/E projections show stronger NSI effect for parameters that shift oscillation phase and they are more directly connected to oscillation physics, but have unequal statistics between 4 angular slices.

For NOvA analysis, the full 2D distribution in L/E and $\cos\theta_{zenith}$ is used, which prevents all available information without forcing a choice between E and L/E projections. The angular slices shown here are for visualization only. The actual selection efficiency and purity use the complete 2D distribution to maximize sensitivity.

4.5 Summary: Implications for Atmospheric Neutrino Measurements

This chapter has examined how NSI modifies atmospheric neutrino oscillations and the resulting observable event rates. The key features are: First, the ν_μ disappearance channel dominates both statistics and sensitivity, particularly for $\mu - \tau$ sector parameters. The off-diagonal $\varepsilon_{\mu\tau}$ produces the most distinctive signatures with large, structured modifications. ν_e final state provide important complementary constraints despite lower statistics.

Secondly, NSI effects mainly affect upward going atmospheric neutrinos that traverse significant Earth matter. This angular dependence means the full 2D energy angle distribution provides much stronger constraints than 1D projections.

Lastly, even large NSI parameters $\varepsilon \approx 0.5$ produce relatively subtle event rate modifications when integrated over phase space. Therefore, distinguishing these effects from standard oscillations requires careful treatment of systematic uncertainty and good reconstruction performance.

Chapter 5

NOvA Analysis

5.1 Monte Carlo production and detector simulation

Monte Carlo simulation is essential for atmospheric neutrino analysis in the NOvA Far Detector, serving multiple critical roles throughout the analysis chain. Firstly, MC simulation enables the prediction of expected atmospheric neutrino event rates by combining flux models, interaction cross sections, and detector response. Secondly, MC simulation is necessary to evaluate trigger efficiency, particularly for the NNBarDDT trigger which was not originally designed for atmospheric neutrinos. Thirdly, it provides the foundation for developing and optimizing event reconstruction algorithms, including neutrino interaction vertex finding, particle identification, and energy estimation. Fourth, it enables the optimization of event selection criteria by characterizing signal topologies and background rejection. Finally, simulation provides the framework for estimating systematic uncertainties arising from flux predictions, cross-section modeling, and detector response.

This section describes the Monte Carlo simulation chain used for this atmospheric neutrino analysis, following the general NOvA simulation framework [31] with modifications specific to atmospheric neutrinos. Figure 5.1 demonstrates the full chain for simulation procedure, from

atmospheric flux generation through final trigger simulation.

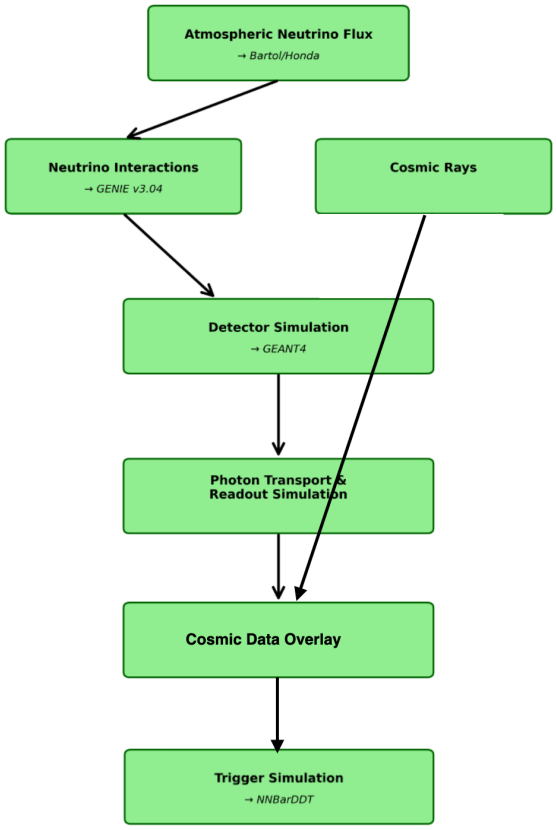

Figure 5.1: NOvA atmospheric neutrino simulation flow

5.1.1 Atmospheric Neutrino Flux

Atmospheric neutrinos are produced when cosmic ray protons and nuclei hit the Earth's atmosphere, creating a cascade of particles (Fig. 2.1). The atmospheric neutrino flux varies with different neutrino energy, zenith angle and detector location. In this analysis, Bartol's atmospheric neutrino flux model [32] is used. It calculates atmospheric neutrino production from cosmic ray interaction with the atmosphere. It gives predictions of flux in 2D histograms for $\nu_e, \nu_\mu, \bar{\nu}_e, \bar{\nu}_\mu$. For example, Figs. 5.2 and 5.3 shows the flux of atmospheric neutrino Bartol predicts from 0.1 GeV to 100 GeV (though this analysis is only using 0.1 GeV to 10 GeV), and for $cos\theta_{zenith}$ from -1 to 1, in

the unit of $cm^{-2}sr^{-1}GeV^{-1}s^{-1}$. This flux model is made specifically for the Soudan Underground Laboratory located approximately 40 miles from NOvA's Far Detector near Ash River. Therefore, they share similar geometric latitude and atmospheric overburden.

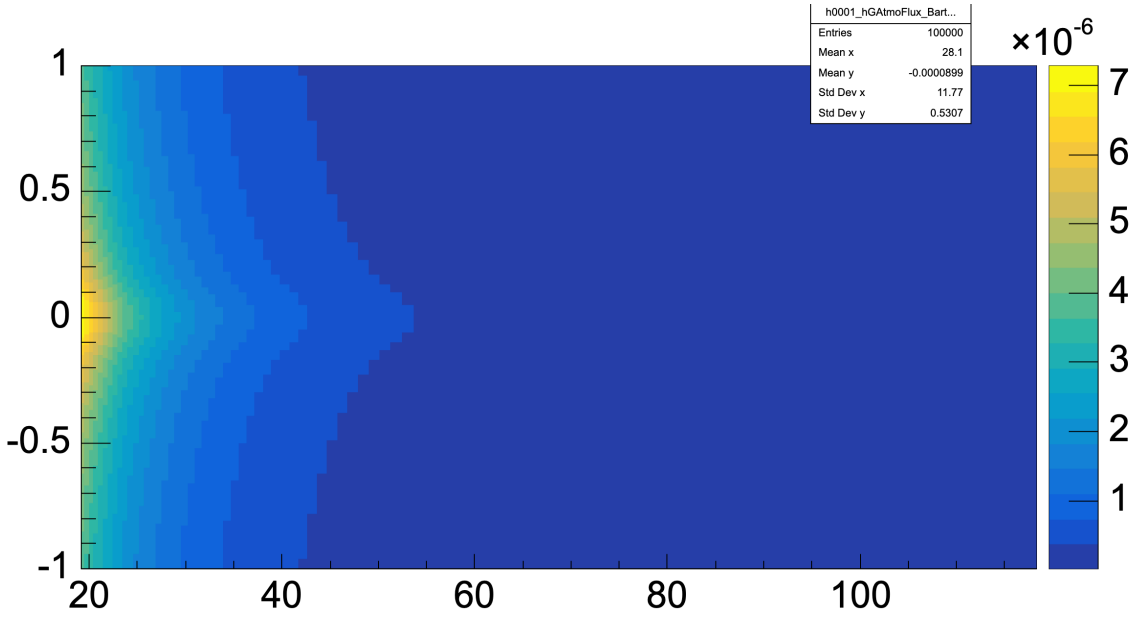

Figure 5.2: Bartol flux for ν_μ with x axis: E(GeV), y axis: $\cos\theta_{zenith}$, z axis: $cm^{-2}sr^{-1}GeV^{-1}s^{-1}$. [32]

5.1.2 Neutrino Interaction Simulation

Next the flux is fed into the GENIE neutrino generator [33] to generate neutrino interactions. This work specifically uses GENIE version v3.04.00 configured for atmospheric neutrino generation. GENIE uses interaction cross sections with the NOvA Far Detector geometry to determine whether a specific atmospheric neutrino will interact with a nucleon inside the detector. When a neutrino interacts inside the detector, GENIE will simulate detailed information about the kinetic information, together with geometric information such as the coordinates of the interaction vertex. For example, the GENIE empirical MEC cross section is shown in Fig. 5.4. Beyond modeling the initial neutrino interaction vertex, GENIE also simulates final state interactions in the nucleus by tracking the propagation of produced hadrons through the target nucleus using the INTRANUKE

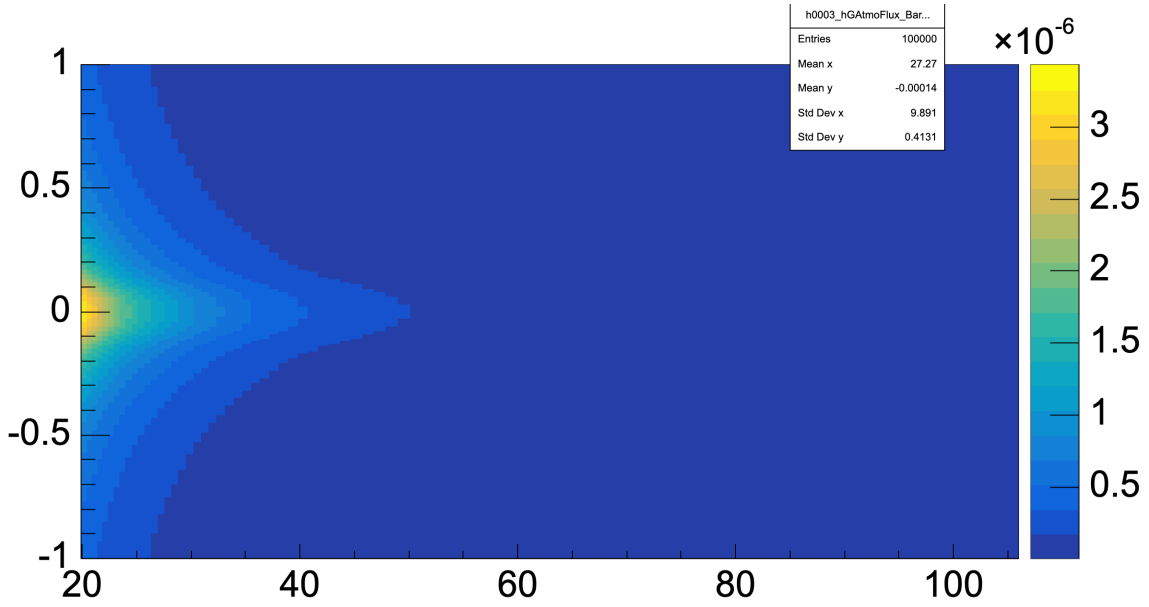

Figure 5.3: Bartol flux for ν_e with x axis: E(GeV), y axis: $\cos\theta_{zenith}$, z axis: $cm^{-2}sr^{-1}GeV^{-1}s^{-1}$. [32]

hadron transport model. As hadrons traverse the nuclear medium, they may undergo elastic scattering, charge exchange interactions, or be absorbed before exiting the nucleus. GENIE's output provides the list of particles that successfully escape the nucleus along with their momentum and energy for input to the detector simulation.

GENIE models all relevant neutrino interaction processes in the atmospheric neutrino energy range (0.1-10 GeV), with the interaction types listed under for example.

- **Charged-current quasi-elastic (CCQE):** Single nucleon knockout reactions, $\nu_\ell + n \to \ell^- + p$, with exchange of W boson. CCQE is most significant at energies below 1 GeV and provides clean single-lepton signatures.

- **Meson exchange currents (MEC):** Multi-nucleon interactions happen when nucleons inside a nucleus are not isolated, and they interact via meson exchange, or two-particle two-hole (2p2h). MEC contributions are important in the 0.5-1.5 GeV range. It gives explanation

to observed excess energy near the quasi-elastic peak. Figure 5.4 shows the GENIE empirical MEC cross section as a function of neutrino energy.

- **Resonance production (RES):** This process becomes significant above 0.5 GeV and peaks around 1-2 GeV. It happens when W boson from neutrino has enough energy to excite the nucleon into a resonance stage.

- **Deep inelastic scattering (DIS):** Over 5 GeV, the W boson's wavelength is small enough to interact with the quark inside the nucleon, and when an interaction occurs, it scatters off individual quarks instead of hitting the nucleus as a whole.

5.1.3 Detector Simulation

Detector simulation is handled by GEANT4 [34], where we provide all the particle information to it and simulate how they propagate through the NOvA FD, while simulating particle propagation, energy deposit, secondary particle generation. The detector simulation follows the standard NOvA simulation chain:

- **GEANT4:** Particle propagation through detector geometry

- **Photon Transport:** Scintillation light collection and fiber transport

- **Electronics Readout:** APD response and digitization

- **CalHit:** Calibrated hit reconstruction

- **Slicer4D:** Event clustering based on spatial-temporal proximity

5.1.4 Cosmic Data Overlay

Due to NOvA's Far Detector ground level geometric location, there is 120 kHz of cosmic rays constantly bombarding the detector; therefore, the simulation needs to include the cosmic rays.

Overlaying cosmic background on top of atmospheric neutrinos is essential, because the real data will include this background; we cannot use beam timing information to cut out cosmic background as is done in the beam neutrino analysis, as atmospheric neutrinos can enter the detector any time.

In the NOvA experiment, we do not simulate cosmic rays, instead, we use cosmic data directly and overlay them on top of the neutrino simulation. Cosmic ray data collected during beam operations in between beam spills is overlaid onto simulated atmospheric neutrino events to reproduce realistic detector conditions. The overlay process combines the energy deposition of one simulated atmospheric neutrino event with cosmic data within the 500 ms time window. This creates a combination of both events.

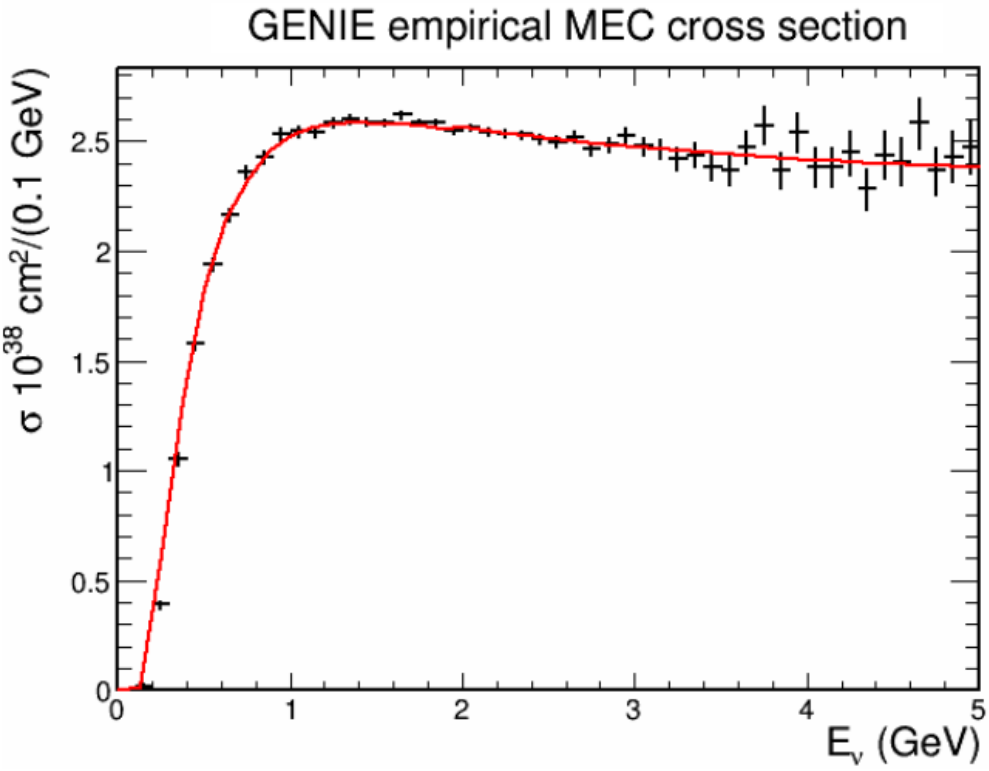

Figure 5.4: GENIE empirical MEC (black) cross section over neutrino E compared to the input GENIE spline(red). (red)[21]

The event display of the final result for this atmospheric neutrino simulation chain Fig. 5.5 is

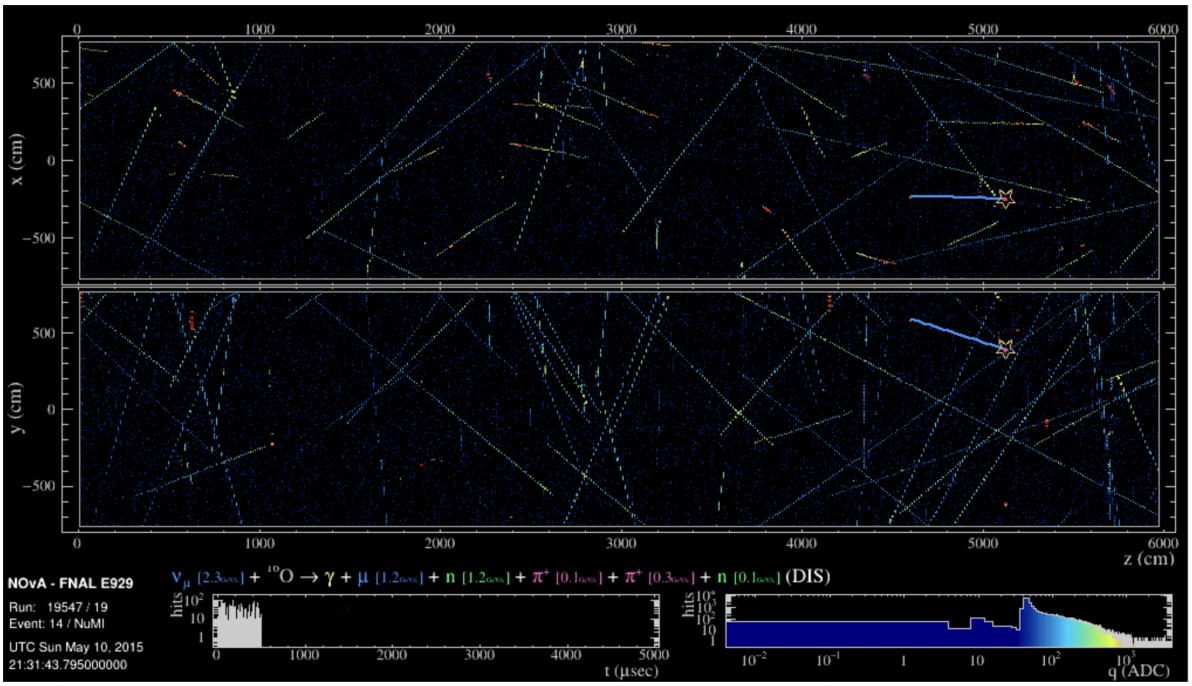

Figure 5.5: NOvA Far Detector Event Display. The color of hits changes based on how long it is read out. Top part shows the NOvA Far Detector in the top view (x-z view) and the bottom panel shows front view (y-z view). This event display shows atmospheric neutrino with cosmic overlay and detector response; a ν_μ enters from right hand side of NOvA FD and experiences $\nu_\mu CC$ interaction, leaving a μ track going to the left.

provided as an example. These simulated events will then be passed to Data Driven Trigger (DDT) simulation to be further investigated.

5.2 Data-Driven Trigger

The Far Detector data acquisition (DAQ) system is illustrated in Figure 5.6. The NOvA Far Detector has 120 kHz of cosmic rays entering the detector, with 10752 front end boards (FEB) taking data continuously from avalanche photodiodes (APDs) that have a readout window of 50 μs, feeding the data to data concentrator module(DCMs). The DCMs combine these signals and make microslices to concentrate the FEB information, and synchronize these events in a time window that is approximately $5\mu s$.[35]. The DCM program will again concentrate these $5\mu s$ combined data into a longer 5ms of millislices, each containing several bytes of microslices. and use a jumbo frame transport protocol to send DCM data to a buffer farm. The bandwidth at which DCM transports these millislices to the buffer farm is 1Gb/s, making it infeasible to record everything from NOvA FD to the storage.

Due to this huge amount of data, NOvA FD uses the Global Trigger (GT) Processor to decide which data to save to storage. The trigger decision can be made based on 3 different conditions:

- Beam Spill Indicator
- Calibration Pulser (10-40 Hz)
- Data Driven Trigger (main trigger for atmospheric neutrinos)

The beam spill indicator signals the GT a start time t_0 to start recording events when the NuMI turns on, allowing the FD to record neutrinos coming out from the NuMI beam. The calibration pulse indicator is set to continuously record data at a 10 Hz frequency to record cosmic rays for detector systematics calibration and for monitoring detector data quality. The Data Driven Trigger (DDT) actively uses free CPUs to run a simple event reconstruction in the data buffer ring

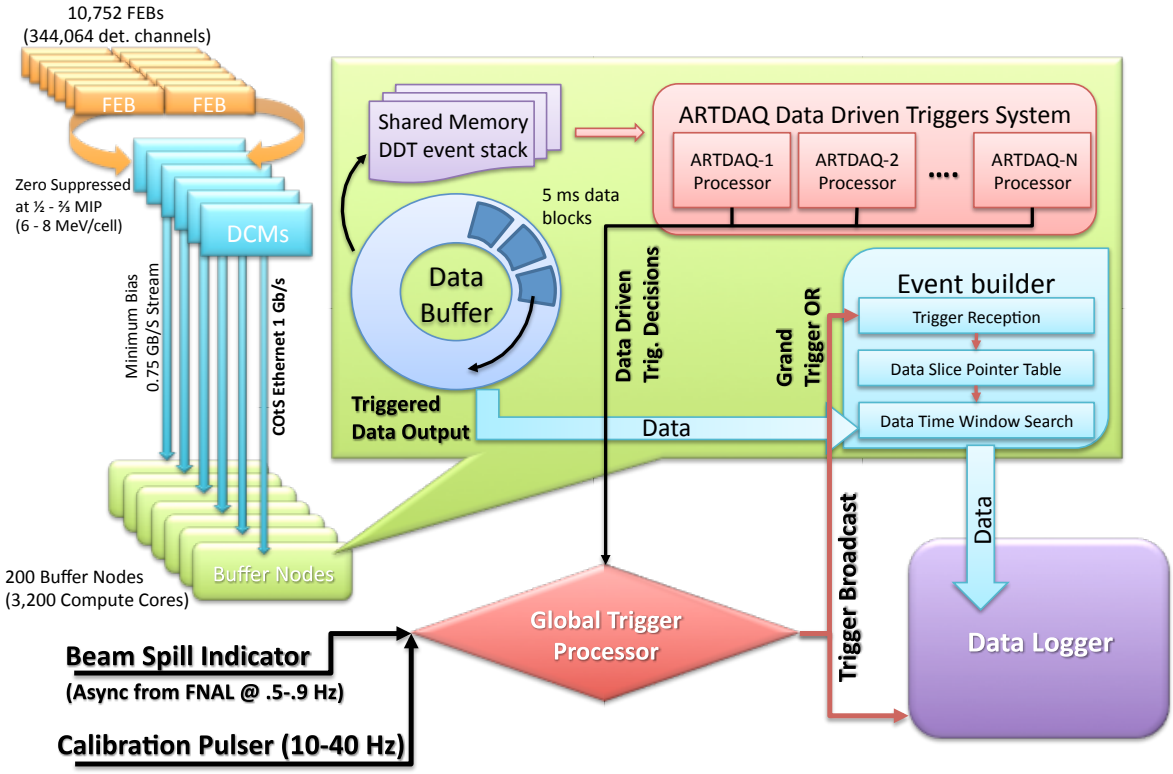

Figure 5.6: NOvA Far Detector DAQ system [36]

and search for interesting patterns. The DDT program includes several parallel programs such as supernova neutrino search, up-going neutrino search, and the neutron-antineutron transition search programs. Whenever one of the programs determines the features of the event on the buffer ring meets its criteria, it tells the GT to start recording the data in the buffer ring, and can allow the GT to keep on taking data for up to 10 seconds for supernova events, and down to 5 ms window that's stored in the data buffer ring.

5.2.1 NNBar Trigger

Atmospheric neutrinos have a dedicated DDT trigger called "UpMu", which searches for upward-going muons; these muons are most likely caused by upward-going muon neutrinos since a cosmic ray muon could not travel all the way through the Earth. However, due to poor reconstruction

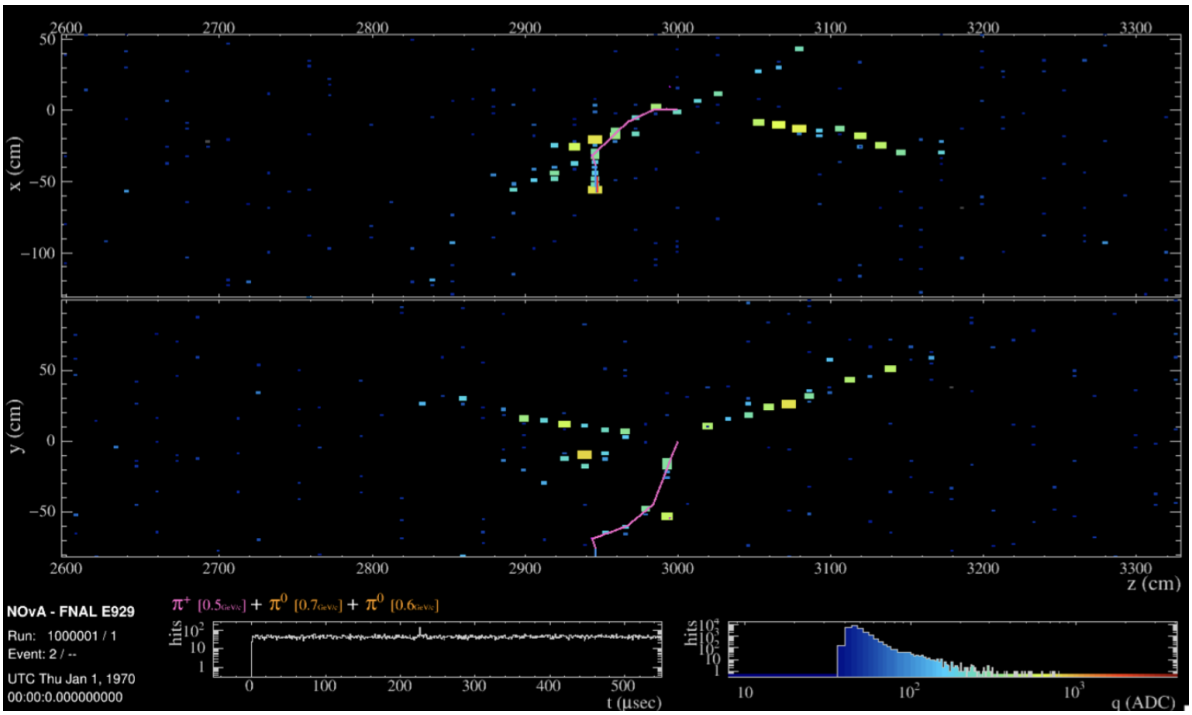

Figure 5.7: NOvA FD event display of $p + \bar{n} \rightarrow \pi^+ + 2\pi^0$, where each of $2\pi^0$ further decay into 2γ [23]. This is the signature of antineutron annihilation following a spontaneous conversion of a neutron into an antineutron.

of track direction based on timing, it is less than 1% efficient in detecting atmospheric neutrinos. An alternative trigger that is not limited by the UpMu specific timing reconstruction quality is required.

The Neutron-antineutron trigger (NNBarDDT) is designed to search for the beyond Standard Model process of neutron-antineutron transitions, but works well for atmospheric neutrinos. The signature of an NNBar event is the annihilation of the antineutron with a nucleon in the detector. Therefore NNBar events are usually contained, with multiple-prongs, and have "star" shape topology due to multiple pions being produced at the annihilation point, including π^0 decay into two photon-induced electromagnetic showers, spreading out from the interaction vertex, see Figure 5.7. Atmospheric neutrino interactions can have a similar signature, with a contained vertex and either a long straight track for a ν_μ interaction or an electromagnetic shower for a ν_e interaction. [23]

The NNBarDDT has the following criteria:

- Containment volume (to remove cosmic muons entering FD from outside)
- width-to-length ratio (remove track like cosmics)
- cell number multiplicity (for star shape identification)
- hit count asymmetry (reject vertical cosmics)
- Hit extent asymmetry (remove through going events)

5.2.2 NNBar trigger performance

The NNBarDDT trigger is applied to the atmospheric neutrino MC sample, and it yields a 11.09% passing rate (true atmospheric neutrinos that pass the NNBarDDT correctly); applied to the pure cosmic data, it yields a 0.81% passing rate (background passing the NNBarDDT incorrectly).

5.3 Neutrino Flavor, Energy and Angle Reconstruction

After the atmospheric neutrinos go through detector simulation, cosmic overlay and DDT, only "truth" level information (i.e. neutrino interaction location, incoming particle direction) is defined. Since this information cannot be perfectly determined in the real data, the same algorithms that would be used on the data to determine the event characteristics are also used on the simulated events. In order to obtain detailed information about the atmospheric neutrino simulation sample, including neutrino flavor, energy and zenith angle, we need to use event reconstruction algorithms. In this analysis, the NOvA “Prod5" reconstruction algorithm was used to run over the atmospheric neutrino simulated events with cosmic overlay that has passed the NNBar DDT trigger selection.

Event reconstruction takes in the raw hits of the simulated atmospheric neutrinos. A “hit" is energy deposited above some threshold in one single cell of the detector. These hits contain

information such as scintillation light intensity in the detector, and the time when they hit in the detector. The hits are then grouped together by algorithms called slicers, such as time slicer or spatial slicer. The reconstruction algorithm then identifies event type (for example, $\nu_\mu CC$) using a convolution neural network (CVN). NOvA reconstructs the neutrino energy based on the sum of leptonic energy (muon or electron) and the deposited hadronic energy. Because we can not see the neutrino tracks in the detector since they have no charge, we can only calculate neutrino energy and direction by final state particles (particles that exit the nucleus).

5.3.1 Reconstruction Algorithms

Event Slicer

As mentioned previously, the hits are grouped together by slicers based on their physical location and the time they hit the detector. Without being grouped, the far detector events look like Figure 5.8 within a 500 μs window, and we do not have information on which hit cells belong to the same particle from a particular interaction. But based on the readout time window in the bottom left, we can visualize which events occurred during the same readout time. The NOvA Far Detector can also be visualized with color representing the caloric energy deposit from the bottom right panel, as shown in Figure 5.9. By using the slicers, we are able to find events that belong to the same particle interaction, and this process is called clustering [37]. The slicer used for these atmospheric neutrino events is TDSlider, which is a slicer based on time density. Whenever the algorithm finds a particular hit, it will calculate the geometric density of hits around this particular hits within the same time gap.

After finding clusters, the algorithm tries to find lines of clusters that resemble tracks left behind particles as they fly through our detector. In this analysis, the Hough algorithm [38] is used. The Hough transform is a voting based method that is known for its line detection capability because it can reduce noise. It works by first taking all the data points, then for every possible shape (for

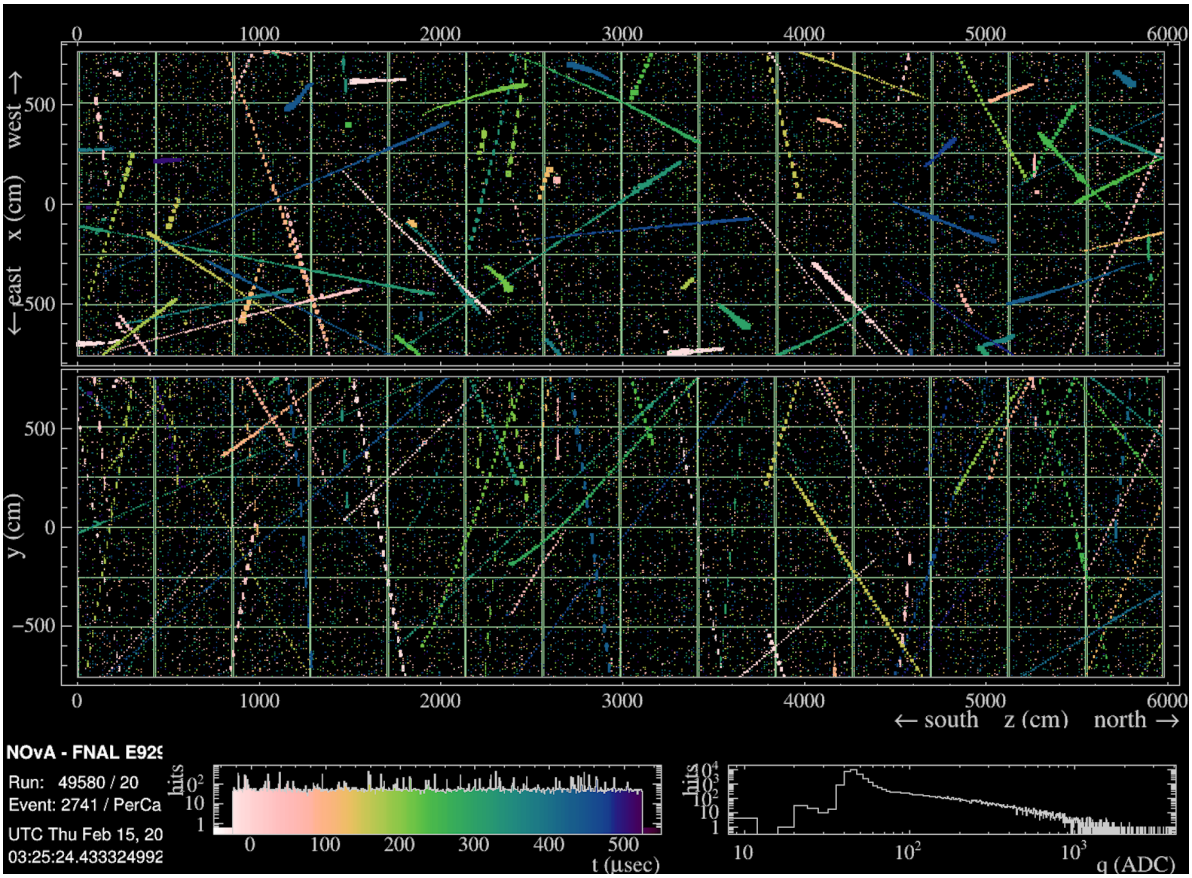

Figure 5.8: NOvA Far Detector Event Display. The color of hits changes based on how long it is read out. Top part shows the NOvA Far Detector in the top view (x-z view) and the bottom panel shows front view (y-z view)

example, a line), it computes its parameters such as its angle and length. Note that Hough does not use slope because it uses polar coordinates; Cartesian space can not represent vertical lines, which is extremely important for atmospheric neutrinos since they can come into the detector from any direction. Then each possible line is converted into a point in (ρ, θ) space. Finally, Hough algorithm in NOvA specifically uses Gaussian smearing centered at the expected (ρ, θ), with the width determined by the detector's resolution to avoid noise and handle uncertainties, instead of the regular Hough Transform's single discrete vote.

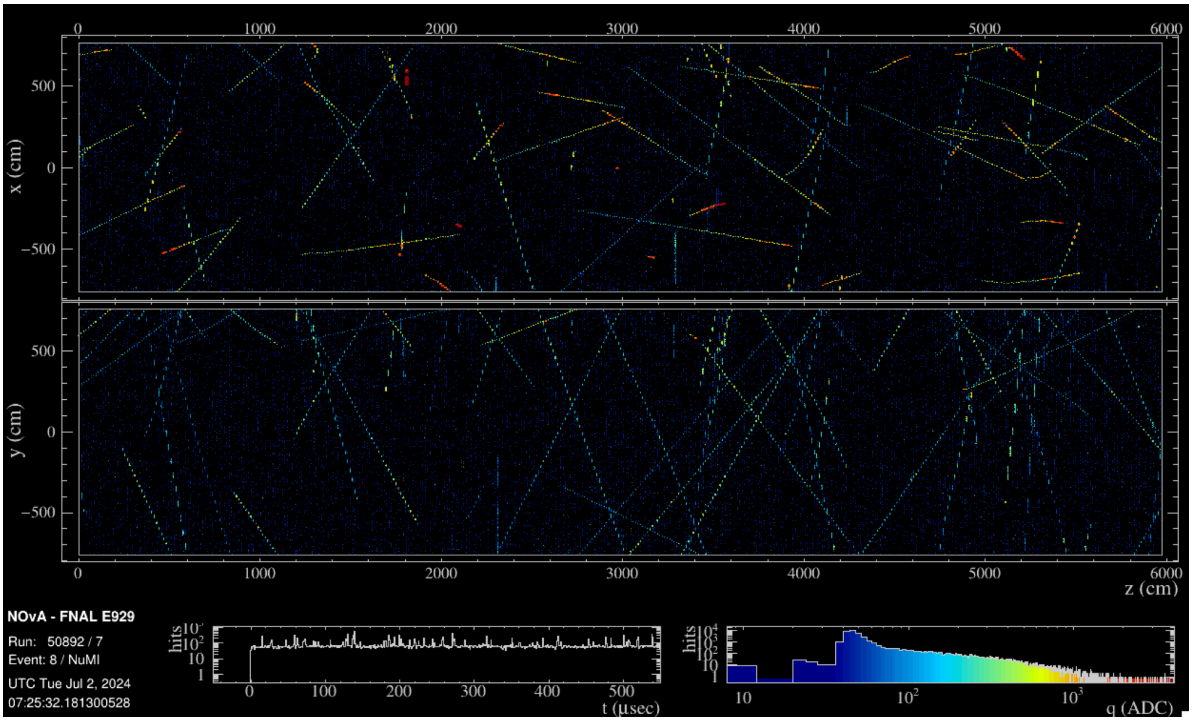

Figure 5.9: NOvA Far Detector Event Display. The color of hits changes based on the caloric energy deposit which is represented in the bottom right panel. Top part shows the NOvA Far Detector in the top view (x-z view) and the bottom panel shows front view (y-z view)

Vertex Finding

Following the Hough transform track finding stage, the vertex finding algorithm tries to locate the vertex of interaction, which is the location where the neutrino interacts with the detector. The algorithm achieves this by looking for intersection of Hough tracks identified in the previous step with the other Hough tracks, which we now call “arms" as they extend out from the vertex. For example, in Fig 5.10, the neutrino interaction vertex is represented by using the yellow star, with arms extending to the left.

The heart of the algorithm is to minimize the global energy cost function based on the distance between hits and their nearest arm. The total energy minimized by the fit [39] is given by Eq. 5.1

$$E = \sum_{i=1}^{N}\sum_{a=1}^{M} V_{ia} M_{ia} + \lambda \sum_{i=1}^{N} \Big(\sum_{a=1}^{M} V_{ia} - 1 \Big)^2 + \frac{2}{\lambda_v} \sum_{a=1}^{M} D_a \,, \tag{5.1}$$

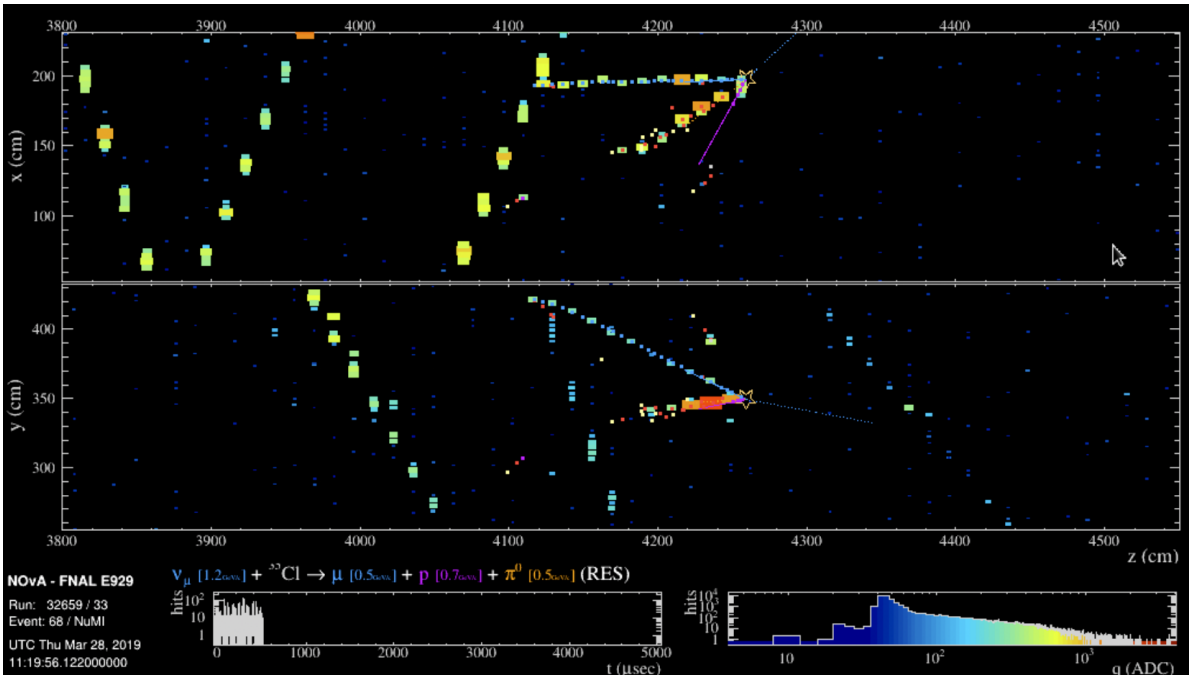

Figure 5.10: Atmospheric neutrino $\nu_\mu CC$ event, with primary ν_μ entering the detector from the right hand side of the detector, with a muon track (blue) and proton track (purple) and a π_0 that decayed into 2 photons(orange)

where M_{ia} is the perpendicular distance from hit i to arm a, V_{ia} is the hit–arm association weight, and D_a is the distance from the vertex to the first hit on arm a. The terms weighted by λ and λ_v penalize poor and inconsistent hit arm associations. Association weights are updated via simulated annealing, in which the "temperature" controls the sharpness of hit-arm association: at a high temperature, many hits contribute to several arms, while at a low temperature, each hit is strongly associated with a single arm. This allows the fitted vertex and track direction to converge to the global optimum instead of getting stuck at a local minimum.

An issue with this method is that in beam neutrino training samples, the majority of true vertices have tracks pointing roughly along the beam direction in z axis, therefore the Hough transform statistically finds more lines that align with the beam. Therefore their intersections produce vertex seeds biased the beam direction, and then elastic arms then refines around those seeds, and since they optimize locally, it tends to preserve that orientation unless there's strong evidence to counter

it. The good news is, the energy function itself is agnostic to beam direction. But because the minimization starts from beam aligned seeds, and because annealing only explores nearby configurations, the optimizer naturally converges toward those initial directions, so the beam direction bias arises from initialization, but not the cost function structure.

The consequences of this bias for atmospheric neutrinos could result in reconstructed track directions slightly peaking along the beam axis, vertex positions displaced toward the upstream direction, and down-going events misclassified as up-coming if the reconstruction has this bias.

Fuzzy-K clustering

Once the reconstruction algorithm recognizes the vertex and arms, it will group different vertex and arms into different clusters, called prongs. The prong finding clustering algorithm used in Prod5 is called Fuzzy-K [40] based on the fuzzy k-means technique, which allows hits to belong to more than one cluster. The core of this algorithm is not to treat every cell hit as a signal, but to give them a probability of been treated as noise instead.

Fuzzy-K starts working from the vertex already identified, and it looks at a circle around the vertex, essentially covering all directions in one detector view. At each angle, it counts how many hits lie roughly along that direction that belong to the same slice. Then each hit is given a calculated angular uncertainty, which depends on how far the hit is from the vertex; nearer hits have larger uncertainty, whereas further hits are cleaner in direction and therefore have smaller uncertainty. This allows Fuzzy-K to build a smooth angular hit density map, essentially identifying how many hits in each direction.

The direction with the highest hit density is chosen as the first cluster center, which defines the first prong direction, and hits are associated with that cluster. Once the hits are assigned to a particular cluster, fuzzy-K recomputes the cluster center like fuzzy k-means by updating the mean direction. Hits that belong very little to this particular cluster (prong) are considered noise or unused hits and are set aside to look for other prongs. Then Fuzzy-K looks again at the remaining

unassigned hits and repeats the process, and this process continues until all significant angular peaks are identified. Since NOvA has 2 views (top view x-z and front view y-z), Fuzzy-K looks for prongs separately in each view. Once all of the prongs are identified in each view, they are matched to create complete 3D prongs using Kuiper's test [41]. This test examines the energy distribution over the z direction, and if two 2D prongs from different views have compatible energy distribution shapes along the z axis, they are considered the same physical prong; otherwise, they remain 2D prongs and are saved as separate prongs. These 2D prongs could be useful for atmospheric neutrinos in the future because vertical entering events might only pass through horizontal detector cells, and therefore, have only a frontal y-z view but no top x-z view.

Track Reconstruction

One weak point of Fuzzy-K prongs is that they only contain directions and clusters of hits; they do not have information on how particles traverse or scatter in the detector. Track reconstruction, specifically Kalman track reconstruction, reconstructs the exact 3D trajectory of the particles through the detector. The Kalman tracking method [42] is used because the majority of the atmospheric neutrino signal tracks will be $\nu_\mu CC$, which produce long, straight muons, and $\nu_e CC$, which produce electron showers. The idea of Kalman track filter is that it predicts the next measurement based on the previous measurement, weighting by uncertainties.

First, the Kalman filter starts at the downstream end of a slice (the end of an arm, opposite end to the vertex) and picks two points as the starting direction. Then, it predicts where the next upstream hit should be using extrapolation. If one point is found within an uncertainty window, Kalman attaches it to the track; if not, it stops the track. After finding the next point, it calculates the new trajectory with the updated point and repeats this process until no further hits are found. The result of this recursive procedure is a 2D Kalman track build from the x-z and the y-z view, and similar to Fuzzy-K, matched by their Z position (instead of energy).

Besides the Kalman track, another Reconstructed Muon Identification (ReMId) [43] is also

used. Each track is given a muon score that will be used to select a candidate muon track based on the ReMId machine learning classifier. ReMId is a recurrent neural network (RNN) classifier that takes the sequence of hits along a reconstructed track as input, and it outputs the probability that the track is muon like. Each hit is represented by a set of features describing its position, energy deposition, and local geometry, which allows the network to learn correlations along the particle trajectory. This method allows ReMId to distinguish minimum ionizing muons from hadronic or electromagnetic tracks. This allows ReMId to distinguish neutral current (NC) interactions from charge current (CC) interaction; therefore, a cut on ReMId score is used in this analysis to eliminate NC background It was updated in 2019 to improve performance on the cosmic sample, and this version is used in the present analysis.

Event Identification

To be able to do any real physics analysis, the identification of the event type is crucial. NOvA uses Convolutional Neural Networks (CVNs) to identify events based on their interaction topology. Each CVN gives a score based on how likely the event is $\nu_e CC$, $\nu_\mu CC$ (Fig. 6.3) or Neutral Current. In this analysis, the cut from the NOvA 3-flavor (standard) oscillation analysis is used to identify ν_e interactions. It is a combination of 3 different CVN scores: kNue2024CVNe, kNue2024CVNcosmic and kNue2024CosRej, which will be explained further in 5.4.3. For identification of ν_μ interactions, cuts called kNumuBasicQuality and kNumuNCRej are used, and will be explained in the same section.

5.3.2 Zenith Angle Reconstruction

Accurate reconstruction of the neutrino direction is crucial for atmospheric neutrino oscillation analysis, as the oscillation probability depends on the baseline length L, which is determined by the neutrino's incoming direction relative to the detector (zenith angle). For atmospheric neutrinos, the baseline varies from approximately 15 km for downward-going neutrinos (produced in the

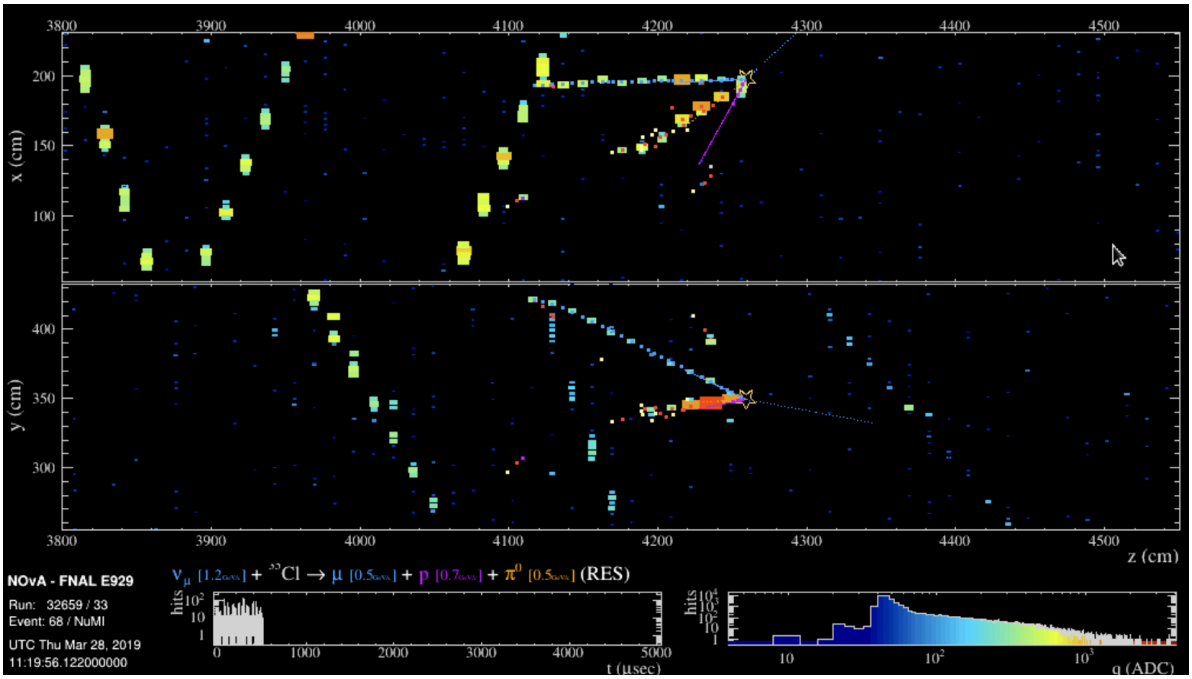

Figure 5.11: Atmospheric neutrino $\nu_\mu CC$ interaction in NOvA Far Detector, leaving muon track (blue), proton prong (purple) and π^0 which further decays into 2 photons (orange)

atmosphere directly above the detector) to approximately 12,800 km for upward-going neutrinos (produced in the atmosphere on the opposite side of the Earth).

The neutrino zenith angle is calculated from the transverse momentum fraction. It is computed from the reconstructed prongs in each slice. For an event with multiple prongs, the total momentum direction is calculated using energy weighted vector sum:

$$\vec{P}_{\text{tot}} = \frac{\sum_i E_i \vec{\mathbf{d}}_i}{\left|\sum_i E_i \vec{\mathbf{d}}_i\right|}, \tag{5.2}$$

where E_i is the calorimetric energy and $\vec{d}_i$ is the direction unit vector for the i-th prong. From this reconstructed direction, the zenith angle θ is obtained from $\cos\theta = \vec{P_{tot}} \cdot \hat{y}$, where $\hat{y}$ is the vertical upward direction.

The baseline distance L can be calculated geometrically based on the zenith angle. For downward-going neutrinos ($\cos\theta > 0$):

$$L = \frac{h}{1 + cos\theta} \tag{5.3}$$

where h is the atmospheric neutrino production height. For upward-coming neutrinos ($\cos\theta < 0$):

$$L = 2(R_{\oplus} - h)\sqrt{1 - cos^2\theta} \tag{5.4}$$

where $R_{\oplus}$ = 6371 km is radius of the Earth. The ratio L/E is used as oscillation variable for atmospheric neutrino analysis.

ν_μ Zenith Angle Reconstruction Performance

The current performance of the angular reconstruction is evaluated using the reconstructed neutrino zenith angle. Figure 5.12 (left) displays the reconstructed zenith angle spectrum for muon neutrinos. It's relatively flat through the entire $\cos(\theta_{zenith})$ from -1 to 1, consistent with the expected atmospheric neutrino flux at these angles.

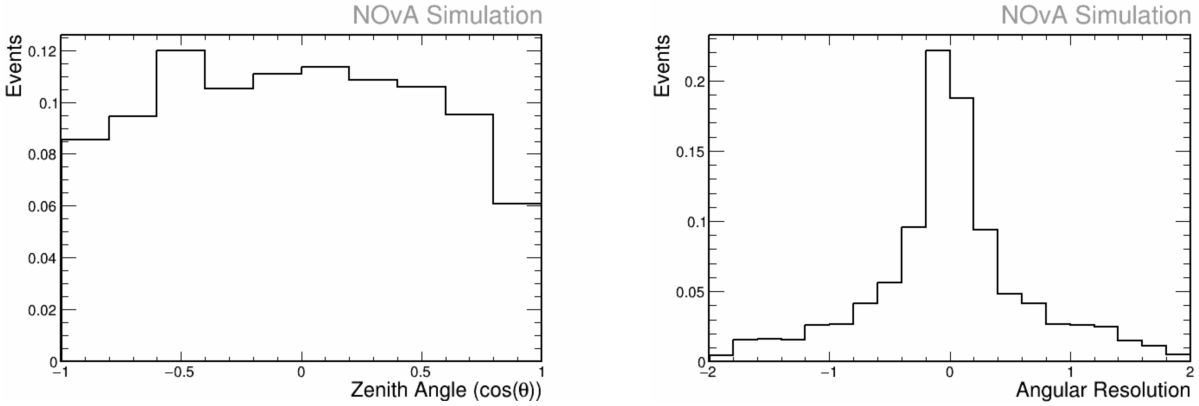

Figure 5.12: Current muon neutrino reconstructed cosine zenith angle (left) and angular resolution, with mean: -0.004 and std dev 0.666(right, reconstructed cos(reco θ_{zenith}) - true θ_{zenith}))

The angular resolution, shown in Fig. 5.12 (right), is quantified as the difference between reconstructed and true cosine of the zenith angle:

$$\Delta\cos\theta = \cos\theta_{\text{reco}} - \cos\theta_{\text{true}} \tag{5.5}$$

The resolution distribution is approximately Gaussian with a mean of -0.004, indicating negligible systematic bias, and a standard deviation of $\sigma(\Delta\cos\theta) = 0.666$. To interpret this uncertainty in angular space, we use error propagation:

$$\sigma_\theta = \frac{\sigma_{\Delta\cos\theta}}{|\sin\theta|} \tag{5.6}$$

To give perspective, for upward-going events, at $\theta = 120^\circ$ (moderately upward), this corresponds to $\sigma_\theta \approx 44^\circ$, while at $\theta = 150^\circ$ (steeply upward), the uncertainty increases to $\sigma_\theta \approx 76^\circ$. This substantial angular uncertainty reflects the reconstruction's poor performance.

To understand the source of the substantial angular uncertainty ($\sigma(\Delta\cos\theta) = 0.666$), a 2D histogram of reconstructed versus true $\cos\theta_{\text{zenith}}$ was produced, shown in Figure 5.13. The distribution shows a clear cross-shaped pattern, with significant event population along the diagonal (correctly reconstructed direction) and along the anti-diagonal highlighted by the red line (events reconstructed in the opposite direction). This indicates that a substantial fraction of events are reconstructed with directions approximately opposite to the true neutrino direction.

To further investigate this behavior, events reconstructed in the opposite direction were isolated by requiring $|\cos\theta_{\text{true}}| > 0.5$ and $|\cos\theta_{\text{reco}}| > 0.5$ with opposite signs. This selection focuses on events where both the true and reconstructed directions are relatively vertical (either relative upward or relative downward-going) but point in opposite directions. Figure 5.14 shows the 2D distribution for this subset of events. These events are also selected and made into a samweb definition to further investigate.

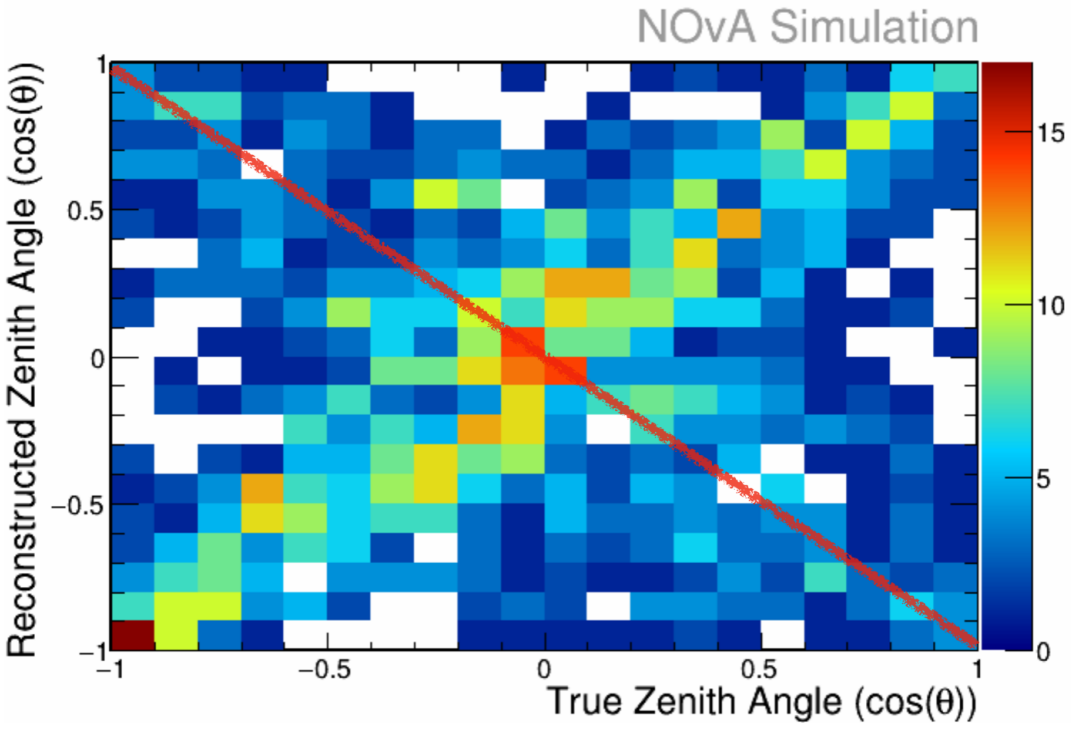

Figure 5.13: Reconstructed cos θ_{zenith} and true cosθ_{zenith}, the red line indicates the events that are reconstructed in the wrong direction

Vertex Position Bias Analysis

To identify the root cause of this directional mis-reconstruction, the vertex position difference ($z_{\text{true}} - z_{\text{reco}}$) was examined for these opposite-direction events. Figure 5.15 shows this distribution, which has a mean of 108.6 cm and standard deviation of 174.5 cm. The predominantly positive values indicate that the true vertex is systematically located downstream (higher z, to the right) of the reconstructed vertex position.

This systematic bias arises because the reconstruction algorithms, including the Convolutional Neural Network (CNN) used for vertex and direction identification, were trained on simulated beam neutrino events. Beam neutrinos have a strongly preferred direction along the NuMI beam axis, and the training therefore has this directional prior. However, atmospheric neutrinos can

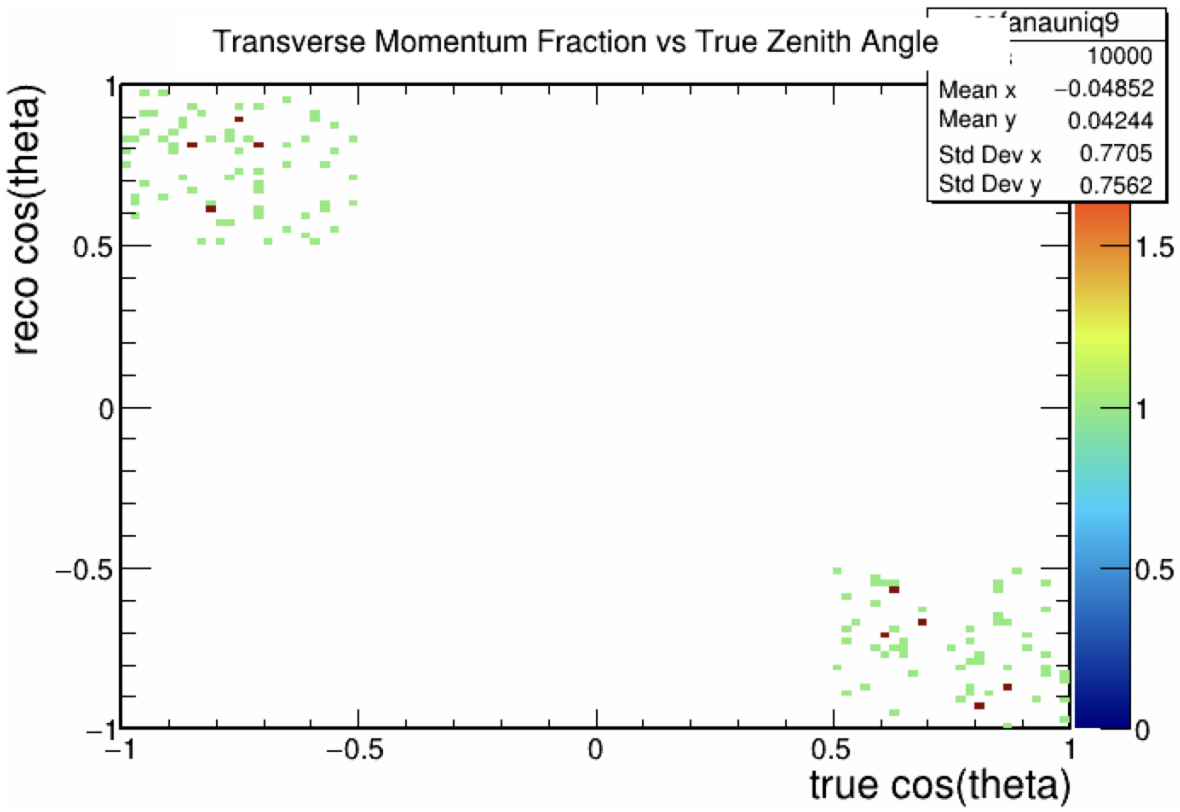

Figure 5.14: Reconstructed cos θ_{zenith} and true cosθ_{zenith}, selecting the region for events reconstructed in the opposite direction to true neutrino direction

arrive from all directions. When applied to atmospheric neutrinos, particularly those arriving from angles opposite to the beam direction, the algorithm's beam-direction bias causes it to misidentify the vertex position and consequently, reconstruct the neutrino direction in the opposite direction.

Event Display Examples

Figure 5.16 shows representative event displays from this mis-reconstructed sample, illustrating the vertex misidentification problem. In these events:

- The reconstructed vertex (marked with crosshairs to the left) is located at the upstream end of visible energy deposition left
- The true interaction vertex is located downstream (marked with star to the right, further along

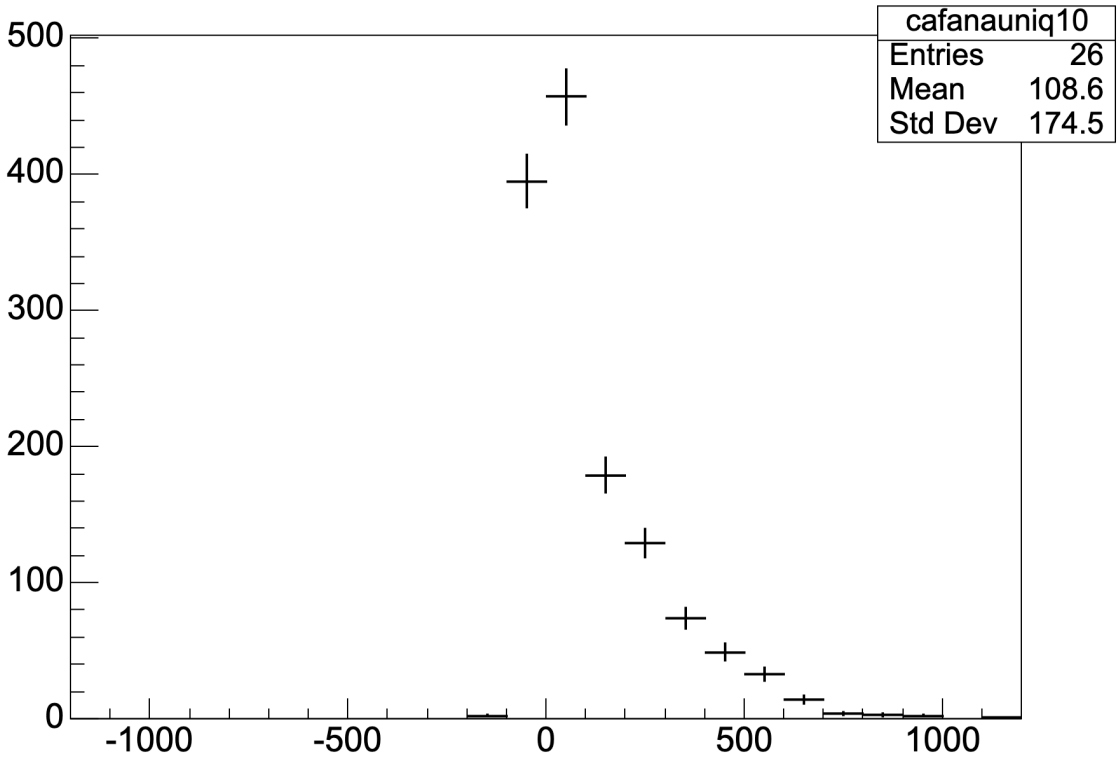

Figure 5.15: true neutrino vertex z position - reco neutrino vertex z position

the beam direction)

- The directional reconstruction reflects the bias of the beam trained algorithm rather than the true atmospheric neutrino direction

This training bias highlights the importance of using appropriately matched training samples for different physics analyses. To improve atmospheric neutrino direction reconstruction, further analysis could be done on the raw atmospheric neutrino files by looking for hadronic energy deposit around end of tracks to help determine neutrino vertex by looking at a 2x2 box, for example, Fig. 5.17, by finding proton energy deposited near true vertex, we can change the direction of the neutrino. Reconstruction algorithms could also to be retrained on atmospheric neutrino Monte Carlo or developed to be direction-agnostic for potential improvements in direction reconstruction.

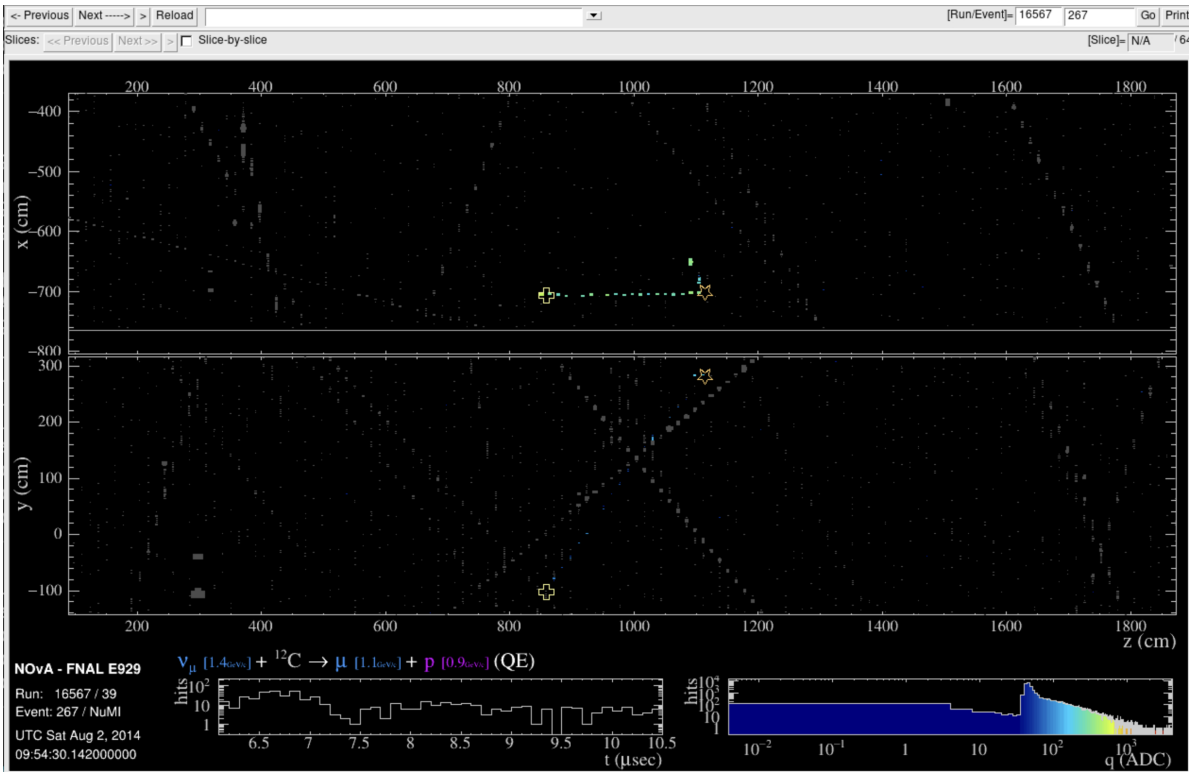

Figure 5.16: On the event display we have xz view (top) and yz view(bottom). The atmospheric neutrino (ν_μ) travels from top right of the detector to the bottom left side. With the true neutrino interaction vertex marked by the star shaped topology, and a muon track going along the blue line and a short proton track depositing energy only in one plane. The reconstruction however, picks the crosshair as the neutrino interaction vertex by mistake, and deciding the muon goes to the top right corner of the detector incorrectly.

Optimistic Resolution with Well-Reconstructed Vertex Selection

The angular resolution can be significantly improved by selecting events with well reconstructed vertex. To demonstrate this potential improvement, I select events where the reconstructed vertex position is within 30 cm of the true vertex position, as shown in Figure 5.18. While this selection uses truth information not available in real data, it provides an estimate of the best achievable performance if vertex reconstruction biases could be mitigated.

With this selection applied, the angular resolution improves to $\sigma(\Delta\cos\theta) = 0.285$ with a mean of -0.016, which is a factor of 2.3 improvement over the baseline reconstruction. Using the same conversion to angular space, this corresponds to angular uncertainties of approximately 16°

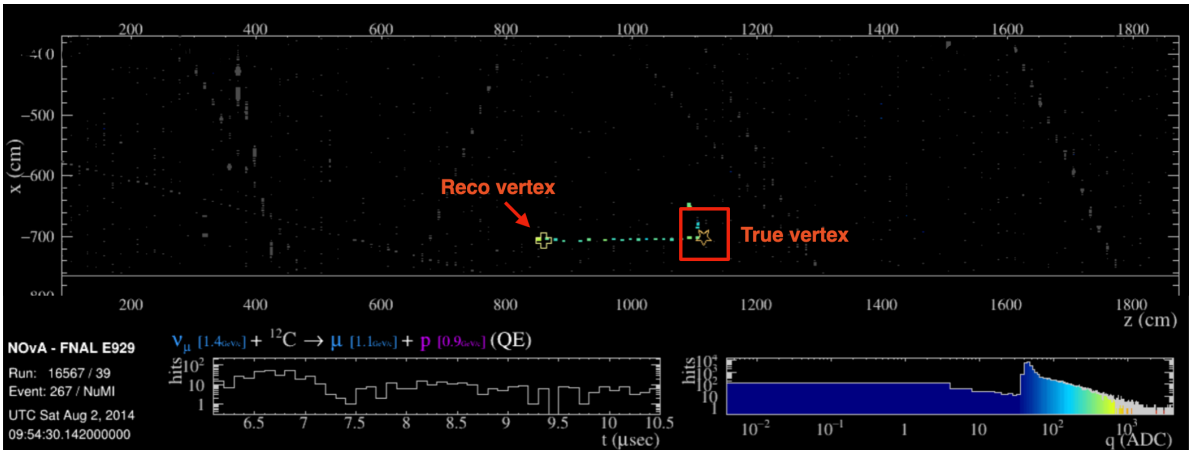

Figure 5.17: xz view of event display clearly showing true neutrino vertex and reconstructed neutrino vertex in the opposite two ends, with reconstruction algorithm preferring upstream direction

at $\theta = 120^\circ$ and 33° at $\theta = 150^\circ$ for upward-going neutrinos. This enhanced resolution provides better separation between different baseline lengths, improving sensitivity to oscillation parameters in the L/E analysis.

This optimistic scenario demonstrates the performance limit achievable with improved vertex reconstruction. In real data analysis, similar improvements could potentially be obtained through:

- Checking hadronic energy deposits around prong ends for vertex identification
- Retraining reconstruction algorithms on atmospheric neutrino Monte Carlo rather than beam neutrinos
- Incorporating additional information, such as timing or improved particle identification

Table 5.1 summarizes the angular resolution performance for both scenarios.

ν_e Zenith Angle Reconstruction Performance

The zenith angle reconstruction for electron neutrino events follows a similar methodology but exhibits different performance characteristics due to the electromagnetic shower topology. Figure 5.19 (left) shows the distribution of reconstructed $\cos(\theta_{\text{zenith}})$ for electron neutrino events,

Table 5.1: Comparison of angular resolution performance for current (all events) and optimistic (well-reconstructed vertex within 30 cm) reconstruction scenarios, shown for representative upward-going zenith angles.

Scenario	Mean	$\sigma(\Delta\cos\theta)$	σ_θ at 120°	σ_θ at 150°
Current (all events)	-0.004	0.666	$\sim 44°$	$\sim 76°$
Optimistic (vertex < 30 cm)	-0.016	0.285	$\sim 19°$	$\sim 33°$
Improvement factor	–	2.3×	2.3×	2.3×

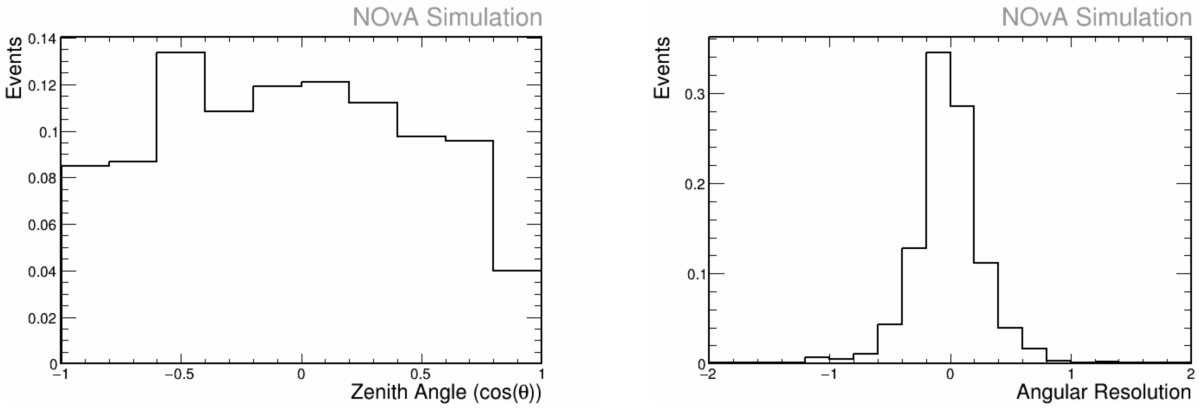

Figure 5.18: Optimistic muon neutrino reconstructed cosine zenith angle (left) and angular resolution, with mean: -0.016 and std dev 0.2845(right, reconstructed cos(reco θ_{zenith}) - true θ_{zenith}))

which also spans the full angular range from upward-going ($\cos\theta_{zenith}$ = -1) to downward-going ($\cos\theta_{zenith}$ = 1) directions.

The angular resolution for electron neutrinos, shown in Figure 5.19 (right), yields mean of -0.02, with standard deviation at $\sigma(\Delta\cos\theta) = 0.287$. This represents significantly better performance compared to the baseline muon neutrino reconstruction ($\sigma(\Delta\cos\theta) = 0.666$), achieving resolution comparable to the optimistic muon neutrino scenario. The improved resolution for electron neutrinos can be attributed to less beam baseline bias in cvn training, together with more electron energy deposit near the actual vertex.

Using the same error propagation formula $\sigma_\theta = \sigma_{\Delta\cos\theta}/|\sin\theta|$, the electron neutrino angular resolution corresponds to approximately ~ 19 at $\theta = 120^\circ$ and $\sim 33^\circ$ at $\theta = 150^\circ$ for upward-going events. This performance is nearly identical to the optimistic muon neutrino scenario, demonstrating that the reconstruction algorithm is better at reconstructing the zenith angle of electron neutrinos.

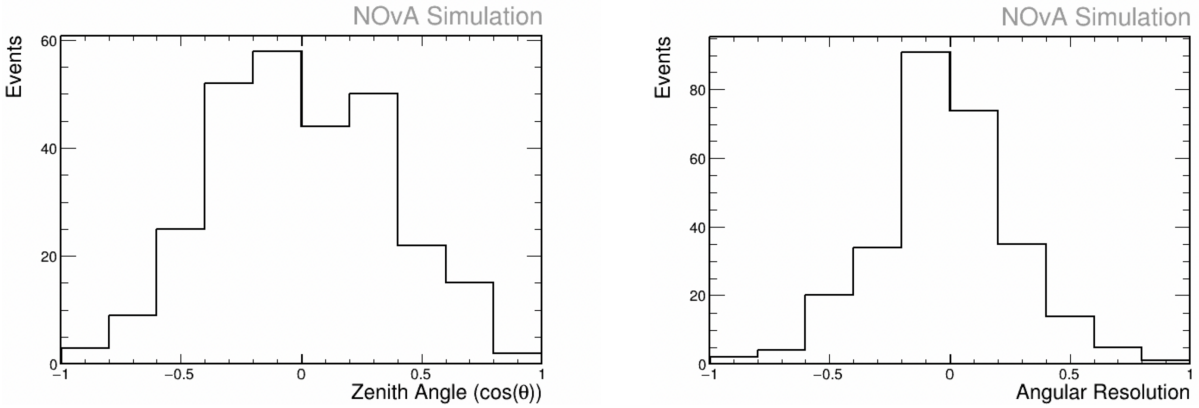

Figure 5.19: Electron neutrino reconstructed cosine zenith angle (left) and angular resolution, with mean: -0.02 and std dev 0.2874(right, reconstructed cos(reco θ_{zenith}) - true θ_{zenith}))

Figure 5.20: $\nu_e CC$ event (a) and ν_μCC event (b)

5.3.3 Energy Reconstruction

For oscillation analysis, the atmospheric neutrino energy estimation is crucial because the oscillation probability is directly linked to L/E. Because neutrinos do not leave tracks behind them, the only method to estimate neutrino energy is by measuring the energy of the secondary particles produced from the neutrino interaction.

Muon Neutrino Energy

Due to the Bethe-Bloch [44] curve for muons and the relatively flat region at $\beta\gamma \approx 3$–5 with constant energy deposition for minimum ionizing particles, the energy deposition is proportional to the track length inside the detector. The energy reconstruction method used for atmospheric neutrinos in this analysis utilizes kNumuE = kNumuMuE + kNumuHadE due to conversation of energy, which adds muon energy determined by muon track length, together with hadronic energy, which can be visualized in Fig. 5.20(b). The muon energy is calculated based on track length due to muons being minimum ionization particles in the this energy range given the Bethe-Bloch curve (Fig. 5.21).

$$\left\langle -\frac{\mathrm{d}E}{\mathrm{d}x} \right\rangle = K z^2 \frac{Z}{A} \frac{1}{\beta^2} \left[\frac{1}{2} \ln \left(\frac{2 m_e c^2 \beta^2 \gamma^2 T_{\max}}{I^2} \right) - \beta^2 - \frac{\delta(\beta\gamma)}{2} - \frac{C}{Z} \right], \tag{5.7}$$

with:

- $K = 4\pi N_A r_e^2 m_e C^2 = 0.307075$ MeV cm^2 mol^{-1} is dE/dx coefficient,
- z is the electric charge of the incident particle,
- Z is atomic number of the absorber and
- A is the atomic mass of the absorber
- $\beta = v/c$ is incident particle's velocity relative to the speed of light
- γ Lorentz factor = $1/\sqrt{1-\beta^2}$,
- m_e is the electron mass,
- $T_{\max}$ is the maximum kinetic energy possible to be transferred to a free electron in a single collision:

  $$T_{\max} = \frac{2 m_e c^2 \beta^2 \gamma^2}{1 + 2\gamma m_e / M + (m_e/M)^2},$$

  where M is the mass of the incident particle,
- I is the mean excitation (ionization) potential of the target absorber,
- $\delta(\beta\gamma)$ is the density-effect correction at high energies,
- C/Z is the shell correction at low energies.

The first log term tells us the higher the speed of the incident particle, the more energy the particle will lose to the absorbing medium due to ionization. the $\frac{1}{\beta^2}$ term shows us more rapid

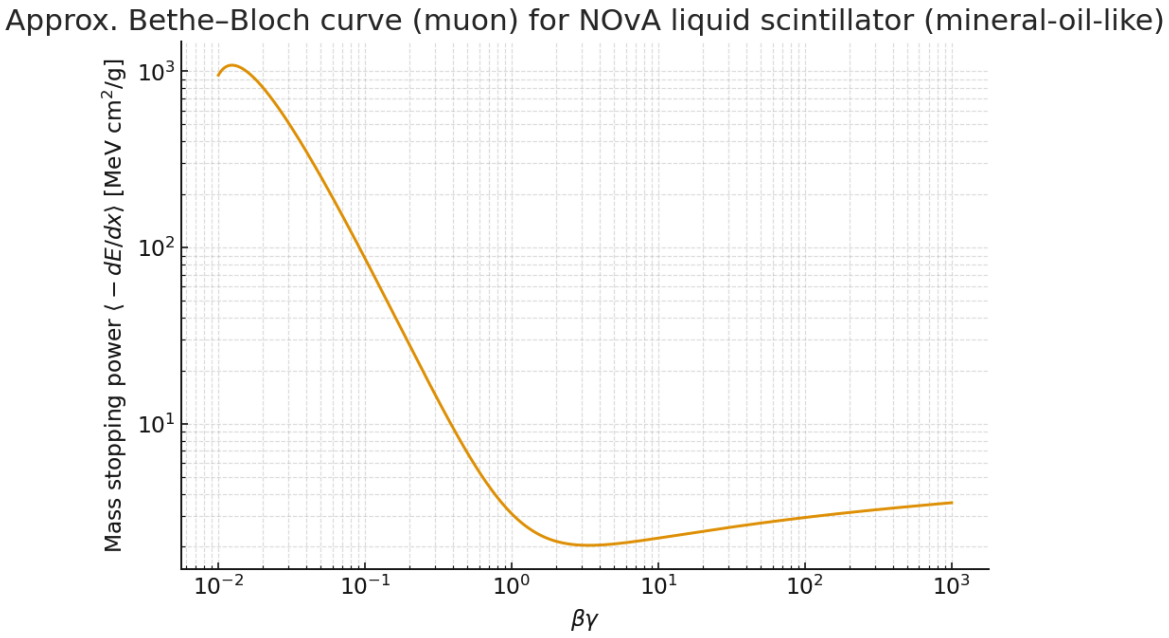

Figure 5.21: Mean energy loss in NOvA's Far Detector mineral oil liquid scintillator

energy loss for slower particles, leaving a shorter track. The Bethe-Bloch curve (fig. 5.21) shows that the energy loss reaches a minimum near $\beta\gamma \approx$ 3-5, which corresponds to the minimum ionizing particles (MIP) and rises at high energy due to relativistic effects and the density correction.

ν_μ Energy Reconstruction Performance

The current performance of the energy reconstruction is evaluated using reconstructed neutrino energy. Figure 5.22 shows the reconstructed energy distribution and energy resolution for atmospheric neutrinos in the NOvA detector.

The left panel of Figure 5.22 displays the reconstructed energy spectrum for muon neutrinos, which peaks around 2 GeV, consistent with the expected atmospheric neutrino flux at these energies. The distribution extends to approximately 10 GeV, capturing the typical energy range of atmospheric muon neutrino interactions in the detector.

The right panel shows the energy resolution, defined as the difference between reconstructed and true energy (reconstructed E − true E). The distribution is approximately Gaussian, centered

near zero with a mean of -0.194 GeV and a standard deviation of 0.66 GeV. The slightly negative mean indicates a small systematic underestimation of the neutrino energy, which could arise from several sources: undetected particles escaping the detector (such as neutrons), muons exiting the detector volume before depositing all their energy, or hadronic shower energy falling below the detection threshold. The standard deviation of 0.66 GeV represents the energy resolution of the reconstruction algorithm and reflects the combined uncertainties from detector response, muon range measurement, hadronic shower reconstruction, and energy calibration.

For a typical atmospheric muon neutrino energy of 2 GeV, this corresponds to a fractional energy resolution of approximately $\sigma_E/E \approx 33\%$, which means it can typically be measured with an uncertainty of $\pm$ 0.66 GeV. This is adequate for oscillation analyses where the L/E dependence spans orders of magnitude. The energy resolution is crucial for accurately determining the oscillation parameters, particularly $|\Delta m^2_{32}|$, θ_{23} and $\varepsilon_{\mu\tau}$, as it affects the ability to resolve the oscillation pattern in the L/E distribution.

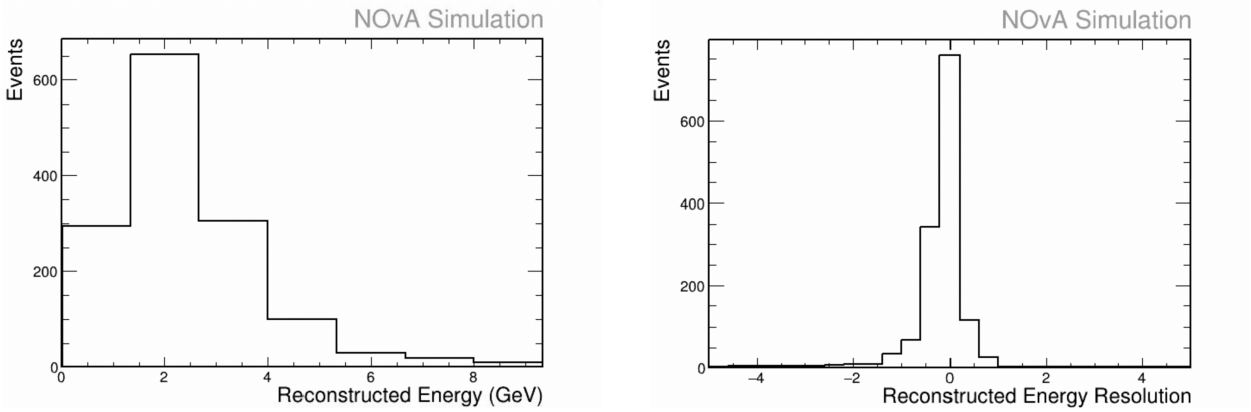

Figure 5.22: Current muon neutrino reconstructed energy (left) and energy resolution, with mean: -0.194 GeV and std dev 0.66 GeV (right, reconstructed E - true E)

Assuming the problem of the neutrino vertex being identified in the wrong direction can be solved, with the exact same energy reconstruction method the optimized reconstruction reduces the systematic bias from -0.194 GeV to -0.165 GeV and improves the resolution from 0.66 GeV

to 0.54 GeV as shown on the right panel on Fig. 5.23, representing an 18% improvement in the standard deviation. This corresponds to an improved fractional energy resolution of approximately $\sigma_E/E \approx 27\%$ at 2 GeV. The reduction in both bias and resolution width enhances the ability to precisely map the oscillation pattern in L/E space, leading to improved constraints on the oscillation parameters $\varepsilon_{\mu\tau}$ and $\sin^2\theta_{23}$.

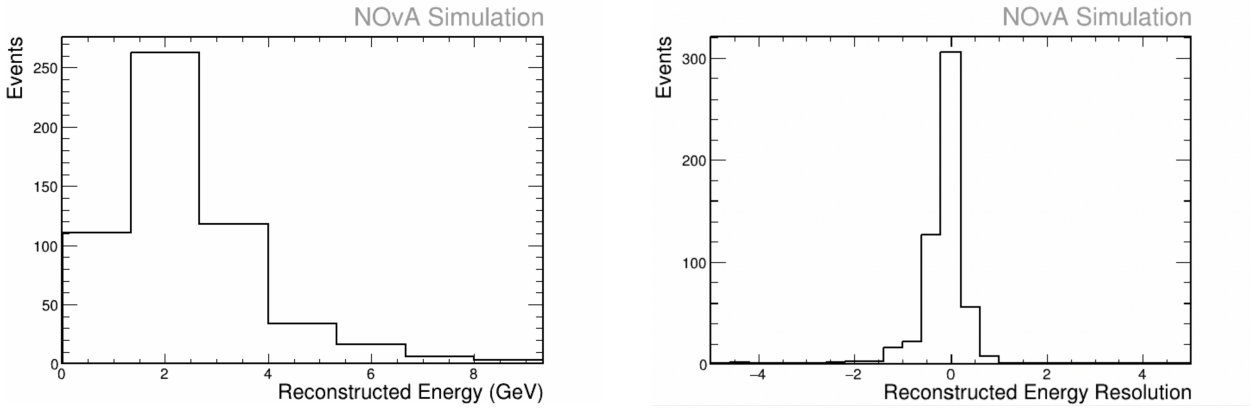

Figure 5.23: Optimistic muon neutrino reconstructed energy (left) and energy resolution, with mean: -0.165 GeV and std dev 0.54 GeV (right, reconstructed E - true E)

Electron Neutrino Energy

The energy of the electron neutrino is determined by the outgoing particles from the $\nu_e CC$ interaction, which has an electron shower and hadronic tracks coming out from the interaction, see Figure 5.20 (a).

The energy reconstruction for electron neutrino events accounts for the different detector responses to electromagnetic and hadronic energy deposition. Electromagnetic showers (from electrons and photons) produce approximately 1.26 times more detectable light than hadronic showers of the same energy [45].

To estimate the neutrino energy, a quadratic calibration is applied to the summed electromagnetic and hadronic components:

$$E_\nu = A \cdot E_{\text{EM}} + B \cdot E_{\text{had}} + C \cdot E_{\text{EM}}^2 + D \cdot E_{\text{had}}^2 \tag{5.8}$$

where prongs are classified as electromagnetic or hadronic based on CVN particle identification scores. The NOvA beam energy estimator achieves an energy resolution of approximately 10% for electron neutrino events in the 1-4 GeV range. The Ev, E_{EM} and E_{had} are the summation of energy deposition from the electromagnetic shower and hadronic prongs. The constants A, B, C, D are scalar constants that are fitted.

ν_e Energy Reconstruction Performance

The left panel of Figure 5.24 displays the reconstructed energy spectrum for electron neutrinos, which peaks around 1–2 GeV, consistent with the atmospheric neutrino flux. The energy distribution starts at 0.5 GeV and extends to maximum of 6 GeV.

The right panel shows the energy resolution for electron neutrinos, with a mean of -0.03 GeV and a standard deviation of 0.229 GeV. The near-zero mean indicates minimal systematic bias in the energy reconstruction, significantly better than the muon neutrino case (-0.194 GeV). The standard deviation of 0.229 GeV is also substantially smaller than that of muon neutrinos (0.66 GeV), reflecting the advantages of calorimetric reconstruction for electromagnetic showers.

For a typical atmospheric electron neutrino energy of 2 GeV, this corresponds to a fractional energy resolution of approximately $\sigma_E/E \approx 11\%$, nearly three times better than the current muon neutrino resolution of 33%. This superior energy resolution for electron neutrinos arises because there are fewer undetected particles (such as neutrons or exiting muons) that can carry away energy. The improved resolution for electron neutrinos enhances the sensitivity to electron neutrino appearance in $\nu_\mu \to \nu_e$ oscillation searches.

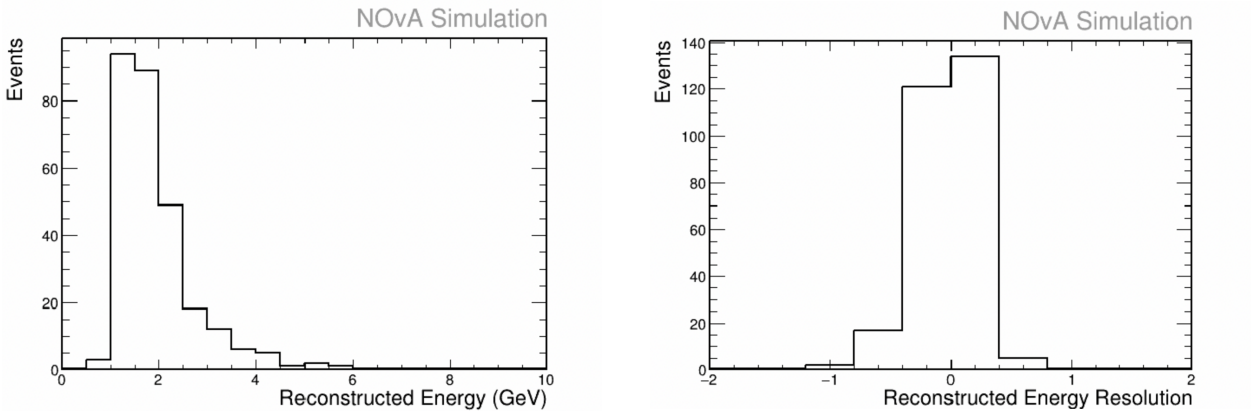

Figure 5.24: Electron neutrino reconstructed energy (left) and energy resolution, with mean: -0.03 and std dev 0.229 (right, reconstructed E - true E)

5.4 Signal and Background Estimation

Due to the ground level NOvA Far Detector geometric setup, the selection of atmospheric neutrino events in NOvA FD faces two major challenges: the small neutrino interaction rate and the overwhelming cosmic ray background. With cosmic muons constantly traversing the detector at around 120 kHz, compared to an expected atmospheric neutrino rate of approximately 0.03 Hz for 8 years of exposure. Therefore, achieving a sufficient signal to background ratio is critical for a viable measurement.

This section presents the methodology for estimating both the atmospheric neutrino signal and cosmic ray background, followed by the development of selection criteria optimized to maximize signal efficiency while rejecting background. The signal prediction uses atmospheric neutrino flux models, neutrino-nucleon cross sections, and measured trigger efficiencies to calculate expected event rates (Section 5.4.1). The cosmic background is estimated using cosmic trigger data with software cuts emulating the NNBar Data Driven Trigger topology (Section 5.4.2). Finally, reconstruction-level selections are applied to identify ν_e CC and ν_μ CC candidates while maintaining acceptable purity (Section 5.4.3).

The goal is to achieve sufficient signal purity to enable oscillation parameter measurements

while retaining enough events for statistical power. The selection strategy differs for electron and muon neutrino channels due to their distinct topological signatures and background compositions.

5.4.1 Atmospheric Neutrino Signal Prediction

The expected atmospheric neutrino signal is calculated from first principles as:

$$N_{events} = \Phi_\nu \times \sigma_{\nu N} \times N_{targets} \times \varepsilon_{trigger} \times T_{exposure} \tag{5.9}$$

We use the Bartol atmospheric neutrino flux model, GENIE v3.04.00 neutrino-nucleon cross sections (spline set AR2320i00000-k250-e1000 with GENIE reweighting factors applied), and 7.16×10^{33} target nucleons in the fiducial volume. The NNBarDDT trigger efficiency of 11.09% was measured using atmospheric neutrinos with cosmic overlay in simulation.

For 8 years of exposure, this yields:

- ν_e charged-current: 2,748 events
- ν_μ charged-current: 2,642 events
- Neutral-current (all flavors): 1,245 events
- **Total: 6,635 atmospheric neutrinos**

5.4.2 Cosmic Background Estimation

Cosmic muons traverse the NOvA Far Detector at approximately 100-120 kHz. To estimate the cosmic background contribution to the NNBar selected atmospheric neutrino sample, we utilize cosmic trigger data processed through reconstruction and subject to software selection cuts designed to emulate the NNBar Data Driven Trigger (DDT) topology requirements.

Data Sample

Our cosmic background sample contains 1.42×10^8 reconstructed slices of events over 60,000 s of livetime during FHC running. This corresponds to an effective cosmic trigger rate of 2,367 Hz. The standard cosmic trigger operates at 10 Hz with 450 μs readout windows, capturing the majority of cosmic ray activity in the detector. Note that NOvA does not simulate cosmic Monte Carlo, we use cosmic data directly.

NNBar Trigger Emulation via Software Cuts

The use of software cuts applied to reconstructed cosmic data, rather than the direct application of the NNBarDDT trigger simulation to raw cosmic files, is necessitated by incompatibilities between the current development analysis framework and the libraries required for offline trigger emulation. Specifically, changes in the artdaq-core package between development versions 3.07.04 and 3.09.02 have removed support for the waveform processing modules needed to execute the DDT algorithm on the stored art-format files. To emulate the NNBar DDT selection, I developed a set of software cuts (kNNBarCutCosmic) that are applied at the reconstruction level. These cuts are designed to reproduce the topology and multiplicity requirements of the hardware NNBarDDT trigger described in section 5.2.

Normalization to NNBar Trigger Rate

Application of the kNNBarCutCosmic software cut to the cosmic trigger sample yields an event rate of 218.2 Hz. Since the actual NNBar DDT trigger operates at 8Hz, we normalize the selected cosmic sample by applying a scale factor

$$\text{Scale factor} = \frac{R_{\text{NNBar DDT}}}{R_{\text{software cuts}}} = \frac{8.0 \text{ Hz}}{218.2 \text{ Hz}} = 0.0367 \tag{5.10}$$

This scale factor of 3.67% is significantly higher than the 0.81% NNBar DDT efficiency measured on non-reconstructed cosmic art files. This difference arises because:

- Reconstruction-level filtering: The standard NOvA reconstruction chain applies quality cuts during slice formation, track/shower identification, and energy calibration. These reconstruction-level selections already reject a substantial fraction of cosmic events before our software cuts are applied. As a result, our kNNBarCutCosmic operates on a pre-filtered sample rather than on raw detector data.

- Timing and causality information: The NNBar DDT has access to complete waveform timing and can apply causality constraints during event formation. This information is either partially lost or not preserved in the same form after reconstruction, making offline cuts less selective.

- Detector information granularity: Art files contain hit-level information including individual cell hit numbers, whereas CAF files store only reconstructed object properties. To calculate quantities like track width-to-length ratios and cell occupancy multiplicity in our software cuts, we must derive them from reconstructed track start and stop positions, whereas the NNBar DDT has direct access to the raw hit-level information.

The assumption underlying our normalization is that each NNBar DDT trigger produces one candidate event slice. Our software-selected sample identifies 218.2 candidate slices per second, and we scale this down by a factor of 8/218.2 to match the observed DDT rate. This approach ensures that the total cosmic background normalization is correct, even though the intermediate selection efficiency differs from that of the DDT trigger. After applying this normalization, the cosmic background rate for events passing kNNBarCutCosmic becomes 8 Hz, matching the NNBar DDT rate observed during data taking.

After applying this normalization, the cosmic background rate for events passing `kNNBarCutCosmic`

becomes 8 Hz, matching the NNBar DDT rate observed during data taking. For 8 years of exposure, this corresponds to approximately 2.0×10^9 cosmic events selected by the NNBar trigger.

5.4.3 Reconstruction Selection Cuts

After the NNBar trigger selection, we apply reconstruction-level cuts to identify ν_e CC and ν_μ CC candidates while rejecting neutral current and cosmic backgrounds. [46] The selections are optimized separately for each flavor based on the distinct topological signatures of electromagnetic showers (from electrons) and minimum ionizing tracks (from muons).

ν_e-like selection

kNue2024FDBasicQuality

- kApplySecondAnalysisMask: Cut to introduce analysis diblock masking rules at CAFAna stage to work around cases where RunHistory did not apply the rules at the reco stage. Keep any section of detector larger then 4 diblocks
- k3flavor2024FDVeto: currently only using kCosRejVeto to reject cosmic rays with hits in the outer veto region of the detector
- kNue2024RecoQuality: Cuts out FEB flashers(nuecosrej.hitsperplane < 8), basic reco quality cuts to make sure elastic.IsValid, and make sure number of prongs larger than 0

kModifiedNue2024CoreBasicEventCut

- kNueEnergy2024 > 1 GeV
- 150 > kNHit > 30
- 500 > kLongestProng > 100

kNue2024ProngContain Ensure the electron shower (prong) is fully contained within detector for complete energy reconstruction

- kDistAllTop > 63 cm
- kDistAllBottom > 12 cm
- kDistAllWest/kDistAllEast > 12 cm
- kDistAllFront/kDistAllBack > 18 cm

kNue2024PID The kNue2024PID combines 3 deep learning classifiers kNue2024CVNe, kNue2024CVNcosmic and kNue2024CosRej, providing strong discrimination between electromagnetic showers and backgrounds, rejecting 156.8 times NC background and 5069.6 times cosmic background, while decreasing signal by 85.9%. Note that the CVN is trained on beam neutrinos, not atmospheric neutrinos.

kNue2024FDNearestSlice The nearest slice selection cut removes background events by requiring the selected slice to be well separated from other activity in the detector. It has temporal separation, together with spacial separation.

- For temporal, it requires at least 100 time units between the slice and the nearest other slice. It ensures clean events isolated in time
- vertical separation: requires distance from detector top must exceed threshold. Slices with high CVNe score have to be 50 cm from detector top, where as low CVNe score events must be at least 400 cm from the detector top
- 3D Spatial separation: requires at least 500 cm separation from nearest other slice to ensure the selected event is spatially isolated. It removes multi-interaction events and cosmic pile up.

ν_μ-like selection

kHas1Prongs: Requires at least one reconstructed prong (track or shower) in the event. This basic topological requirement removes empty slices and ensures the event contains identifiable particle trajectories. This cut maintains 98.1% signal efficiency while providing minimal background rejection, as most triggered events contain at least one prong.

kNumuBasicQuality (from 3 flavor analysis[46]): Applies fundamental quality requirements to ensure well-reconstructed events:

- Track energy: energy.numu.trkccE > 0
- at least one 3D Kalman track with a sel.remid.pid value
- more than 20 hits in the slice: slc.nhit > 20
- more than four contiguous planes: slc.ncontplanes > 4
- at least one track found by the CosmicTrack: trk.cosmic.ntracks > 0 (any track including cosmic)

kNumuNCRej kNumuNCRej cut is a cut based on ReMId mentioned in section 5.3.1; it requires the remid.pid > 0.75. This cut maintains 95.2% efficiency relative to the previous stage while beginning to reject poorly reconstructed cosmic events.

5.4.4 Cut Flow and Cosmic Rejection

Tables 5.2 and 5.3 show the evolution of signal and background through the selection cuts. Key observations are:

Neutral Current Rejection: The RemID variable (for ν_μ) and PID variable (for ν_e) provide powerful NC rejection, with factors of 35.3× and 156.8× respectively, while maintaining reasonable signal efficiency.

Cosmic Ray Rejection: Containment cuts are extremely helpful for cosmic rejection, providing factors of 127.5× (ν_μ) and maintained low background for ν_e (already rejected by PID). The ν_e PID cut achieves extraordinary cosmic rejection of 5,069.6×.

Table 5.2: Cut flow showing signal efficiency and background rejection for ν_μ CC selection

Cut Stage	**Signal**	**Eff.**	**NC Bkg**	**Rej.**	**Cosmic Bkg**	**Rej.**
After NNBar trigger	2662	—	1252	—	8.48×10^8	—
+ kHas1Prongs	2612	98.1%	1229	1.0×	8.48×10^8	1.0×
+ kNumuBasicQuality	2486	95.2%	1130	1.1×	7.79×10^8	1.1×
+ kNumuNCRej (RemID>0.75)	1042	41.9%	32	35.3×	7.79×10^8	1.0×
+ Containment	862	82.7%	32	1.0×	4.53×10^6	172.1×

Table 5.3: Cut flow showing signal efficiency and background rejection for ν_e CC selection

Cut Stage	**Signal**	**Eff.**	**NC Bkg**	**Rej.**	**Cosmic Bkg**	**Rej.**
After NNBar trigger	2763	—	1252	—	1.11×10^9	—
+ kHas1Prongs	2713	98.2%	1229	1.0×	1.11×10^9	1.0×
+ kNue2024FDBasicQuality	2386	87.9%	1013	1.2×	1.02×10^9	1.1×
+ kModifiedNue2024CorePart	1479	62.0%	627	1.6×	3.22×10^7	31.8×
+ kNue2024PID	209	14.1%	4	156.8×	6.35×10^3	5069.6×
+ Containment	200	95.70%	3	1.4×	6.35×10^3	1.0×

5.4.5 Flavor Misidentification

Due to similarities in event topology, a small fraction of events are misidentified between the ν_e and ν_μ channels. Table 5.4 summarizes the cross-contamination rates.

The flavor misidentification is highly asymmetric. The ν_e selection, which relies on the electromagnetic shower identification via the CVN particle identification algorithm, achieves excellent rejection of ν_μ events (99.944% rejection). Only 2 true ν_μ CC events pass the ν_e cuts, contributing

Table 5.4: Flavor misidentification rates and cross-contamination between ν_e and ν_μ selections

Parameter	$\nu_\mu \to \nu_e$-like	$\nu_e \to \nu_\mu$-like
True CC events (after trigger)	3549	3684
Passing opposite-flavor cuts	2	56
Mis-identification rate	0.056%	1.520%
Events in final sample (with 0.75 norm)	1.5	42.0
Contamination of selected sample	0.72%	4.03%

1.5 events (0.72%) to the final ν_e sample.

In contrast, the ν_μ selection shows moderate contamination from ν_e events. Approximately 1.52% of true ν_e CC interactions pass the ν_μ reconstruction cuts, contributing 42 events (4.03%) to the final ν_μ sample. This asymmetry arises because ν_e CC interactions can occasionally produce hadronic tracks from charged pions that mimic the muon track topology, while ν_μ CC events rarely produce the compact electromagnetic shower signature characteristic of electrons.

Figure 5.25 shows the reconstructed energy distribution of misidentified events. The $\nu_e \to \nu_\mu$-like misidentification is distributed across the energy range from 1-8 GeV, with a peak around 2-3 GeV where hadronic activity is most prominent.

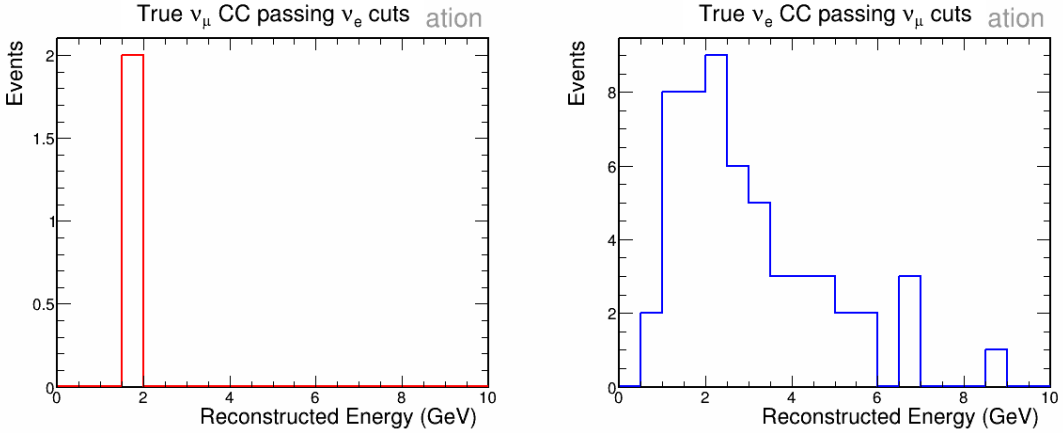

Figure 5.25: Energy distribution of flavor-misidentified events. Left: True ν_μ CC events passing ν_e selection. Right: True ν_e CC events passing ν_μ selection.

Chapter 6

DUNE Analysis

This chapter presents the atmospheric neutrino nonstandard interaction sensitivity study for the Deep Underground Neutrino Experiment (DUNE). Unlike NOvA's surface detector, DUNE's deep underground location provides substantial overburden to reduce cosmic ray background to negligible levels. Therefore, DUNE has excellent atmospheric neutrino purity. This analysis uses a Bayesian Markov Chain Monte Carlo (MCMC) framework [47] implemented in the MaCh3 fitting framework in DUNE atmospheric [28]. Neutrino event reconstruction is performed using the Pandora algorithm [25], which provides particle identification and energy reconstruction optimized for liquid argon time projection chambers (LArTPC). The systematic uncertainties, dominated by atmospheric flux modeling, are incorporated through spline based parameterizations with Gaussian priors derived from model to model spreads, which is described in the following section.

6.1 DUNE flux systematics

Experimental measurements are affected by both statistical fluctuations due to the finite size of the data sample and systematic uncertainties due to limited knowledge of the detector response, neutrino cross-sections, and the atmospheric neutrino flux. Unlike statistical uncertainties, which

we can reduce by increasing exposure, systematic uncertainties do not average away and therefore, become the limiting factor for long term precision.

Including a systematic study brings two major benefits. Firstly, it allows the report of sensitivities or measurements not biased by model assumptions. Secondly, it allows sources of uncertainty that dominate the error budget to be identified. Careful treatment of systematic uncertainties is essential for translating observed event distributions into reliable physics results.

Unlike the NOvA and DUNE beam neutrino analyses, atmospheric neutrino studies do not have a near detector and therefore lack a sample of unoscillated flux measurements to normalize against. As a result, the flux prediction cannot be directly constrained by data, and the fit must rely entirely on theoretical calculations such as the Honda, Bartol, and FLUKA flux models. The absence of a near detector means that uncertainties in the overall flux normalization, spectral shape, and flavor composition cannot be mitigated through cancellations in relative near–far detector measurements, as is done in beam experiments. Consequently, flux-related uncertainties constitute the dominant systematic in atmospheric neutrino analyses.

The uncertainty in the atmospheric neutrino flux prediction originates from limited knowledge of the physical processes that generate neutrinos in the atmosphere. The flux is calculated from the convolution of the incident cosmic ray spectrum with hadronic particle production in atmosphere. Both of these inputs are only partially constrained by external data: cosmic-ray fits vary in normalization and spectral index, while hadron production data are incomplete in the phase space relevant for pion and kaon yields. These limitations result in uncertainties of order 15–20% in the absolute normalization of the flux, with additional energy and angle dependent variations that modify the spectral shape, flavor composition, and zenith distribution [48, 49].

There are four main factors that cause flux systematics: (i) the primary cosmic ray spectrum, including normalization and spectral index; (ii) hadronic product, including pion/kaon yields, cross-sections, and multiplicities; (iii) geomagnetic and atmospheric profile effects; and (iv) flavor and

charge ratios, such as ν_μ/ν_e and $\nu/\bar{\nu}$, typically uncertain at the 5 - 10% level. Because atmospheric oscillation analyses probe a wide range of energy and zenith angle, these uncertainties directly propagate into the dominant error budget of predicted event rates. Differences between flux models can reach 20-30% in the multi-GeV region and near-horizontal directions, substantially larger than the uncertainties from neutrino cross-sections or detector response.

While some analyses incorporate the flux uncertainties provided by a specific model through covariance matrices or dedicated spline parameterizations, this approach implicitly assumes that the corresponding model fully captures the uncertainty space of the true atmospheric flux. In contrast, the present analysis adopts a model-spread envelope derived from several independent flux calculations (Honda, Bartol, and FLUKA). This choice provides a conservative and model-agnostic estimate of the systematic uncertainty by encompassing differences in primary cosmic-ray spectra, hadronic production models, and atmospheric density profiles across calculations. Because these flux models are based on distinct hadronic interaction generators and cosmic-ray fits, the spread between them more realistically reflects the range of plausible flux predictions. The envelope method therefore avoids relying on the internal error decomposition of any single model, while still allowing a smooth parameterization of flux variations through spline interpolation over energy and zenith angle.

In this work, the nominal flux prediction is taken from the Honda 2014 solar-minimum model [49, 50]. To account for the full range of theoretical uncertainty, we do not rely on the internal covariance of this single model. Instead, a flux error envelope is constructed based on the spread between independent flux calculations. Specifically, we compare the Honda solar-minimum flux to alternative predictions, including the Bartol 2004 [32] and Bartol 2025 preliminary fluxes, as well as the Honda solar-maximum configuration. For each $(E_\nu, \cos\theta_z)$ bin, the ratio of each model to the nominal is computed, and the $\pm 1\sigma$ uncertainty is defined as the maximal fractional deviation across models. This produces a conservative uncertainty band that captures the model-to-model spread.

6.1.1 Atmospheric Flux Models

The nominal atmospheric neutrino flux used in this analysis is the Honda 2014 calculation for solar-minimum conditions [49, 50]. This model is based on updated primary cosmic-ray spectra and hadronic interaction modeling using the JAM cascade code, and provides tabulated fluxes as a function of neutrino energy and zenith angle for each flavor and charge. The Honda 2014 flux serves as the baseline for all Monte Carlo (MC) event generation for the DUNE analysis in this work.

To assess the uncertainty associated with the atmospheric flux prediction, the Honda model is compared with two alternative flux calculations. The first is the Bartol 2004 flux [32], which is based on an earlier cosmic-ray fit and hadronic production model; although the public data tables are no longer hosted online, they remain available upon request from the Bartol collaboration.[1] The second comparison model, referred to here as the *Bartol 2025 preliminary flux*, is an updated calculation currently under development by members of the Bartol group in collaboration with DUNE atmospheric analysts. It incorporates updated cosmic-ray fits, modern hadronic interaction generators, and a more detailed geomagnetic treatment.

Because these three flux models are generated with independent assumptions and simulation frameworks, the spread among them provides a conservative and physically motivated estimate of the systematic uncertainty in the atmospheric flux. The resulting model-to-model deviations are used to construct the flux error envelope.

The resulting envelope is parameterized by smooth spline functions in neutrino energy and zenith as shown in Fig. 6.1 . These spline distortions enter the oscillation analysis as nuisance parameters, with Gaussian priors set by the envelope width. In this way, the flux prediction is allowed to vary within a realistic, model-driven uncertainty band, without assuming the internal error breakdown of any one flux calculation. This treatment captures the dominant systematic in atmospheric neutrino analyses and ensures robustness of the results to known limitations of flux

[1] Access to the Bartol 2004 flux tables used in this study was provided by D. Barrow (private communication).

modeling. The effect is non-negligible: the flux envelope induces variations of order 10–20% in sub-GeV samples and up to 30% in multi-GeV horizontal samples, and therefore represents the single largest systematic uncertainty in this study.

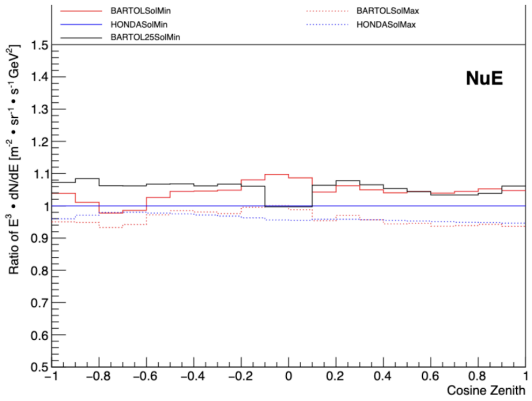

(a) Flux model comparison for ν_e with HondaSolMin as nominal, in cosine θ_{zenith}

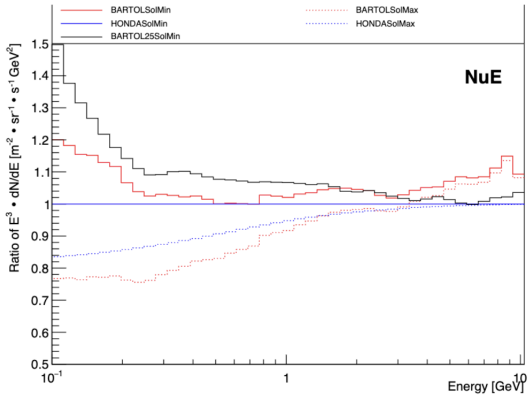

(b) Flux model comparison for ν_e with HondaSolMin as nominal, in energy

Figure 6.1: Comparison of different atmospheric flux models used in constructing the uncertainty envelope.

To visualize the energy dependence of the model-to-model differences more clearly, slices of the flux ratio as a function of $\cos\theta_z$ at representative neutrino energies for ν_e (Fig. 6.2), ν_μ (Fig. 6.3) are shown; $\bar{\nu}_e$, $\bar{\nu}_\mu$ show similar effect. These energy-sliced comparisons reveal that the model spread is smallest at sub-GeV energies and increases with energy, reaching up to $\mathcal{O}(20\%)$ near multi-GeV and horizontal directions. This trend motivates the energy-dependent parameterization adopted for the flux uncertainty envelope.

Although the neutrino–antineutrino flux ratio is not included as an explicit systematic in this analysis, it was cross-checked against previous results for consistency. Figure 6.4 compares the $\nu/\bar{\nu}$ ratios predicted by the Honda and Bartol models to those reported in Ref. [51]. The overall energy dependence and relative hierarchy between $\nu_\mu/\bar{\nu}_\mu$ and $\nu_e/\bar{\nu}_e$ agree well with the established calculations, confirming that the present flux inputs reproduce the expected charge-sign asymmetries. Although these effects are not yet propagated as a dedicated systematic, they could become

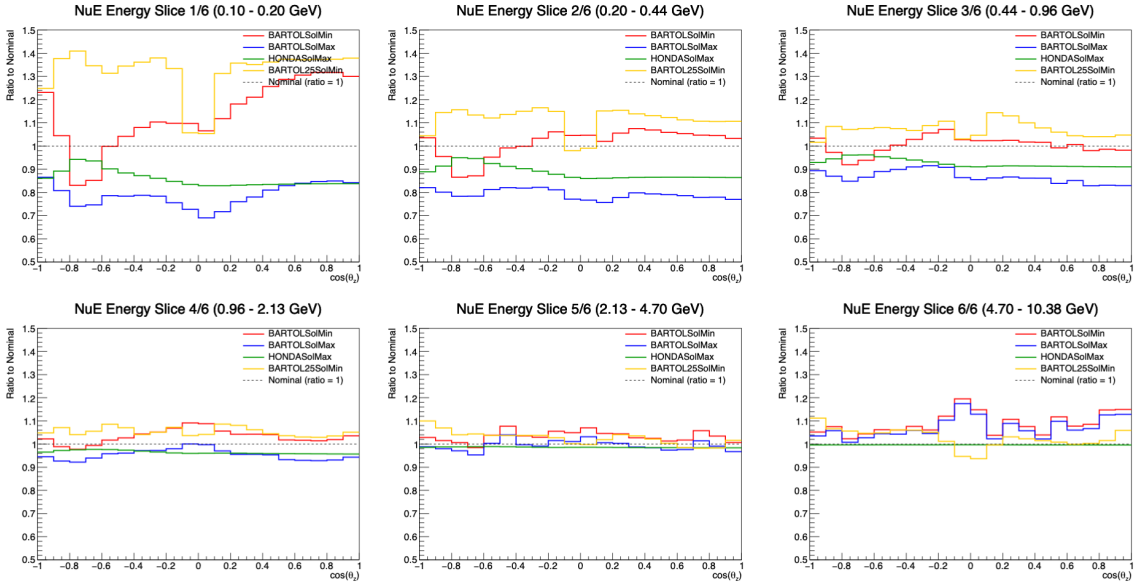

Figure 6.2: Flux model comparison shown as flux ratio slices in $\cos\theta_z$ at representative neutrino energies for ν_e. The shaded regions indicate the model-to-model spread between the Honda and Bartol fluxes. The relative deviation decrease with energy, reaching up to $\mathcal{O}(20\%)$ under 0.5 GeV range.

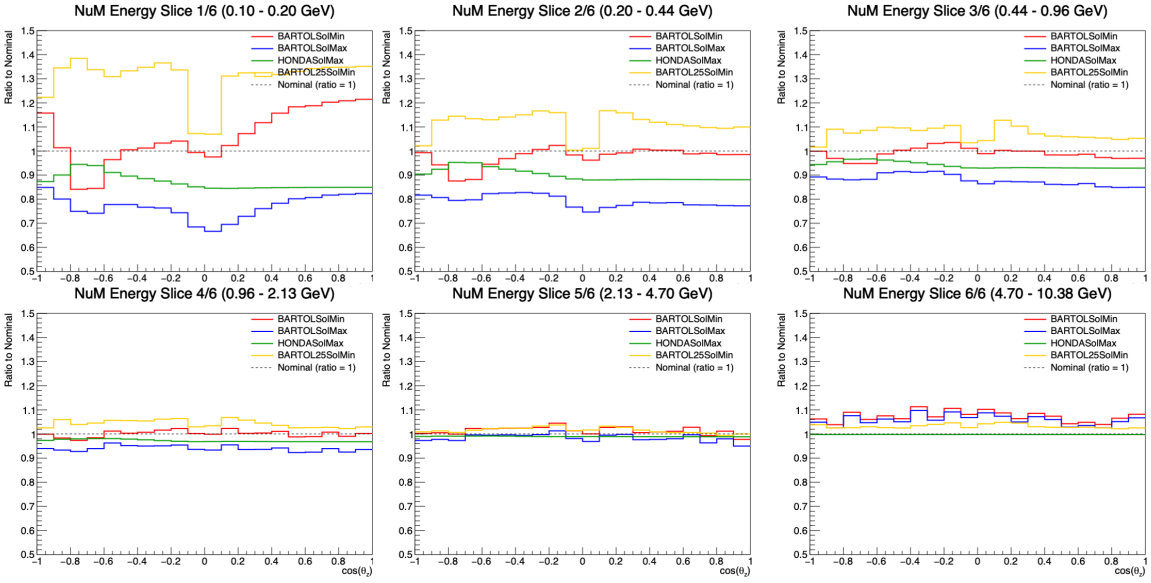

Figure 6.3: Flux model comparison shown as flux ratio slices in $\cos\theta_z$ at representative neutrino energies for ν_μ. The shaded regions indicate the model-to-model spread between the Honda and Bartol fluxes. The relative deviation decrease with energy, reaching up to $\mathcal{O}(20\%)$ under 0.5 GeV range.

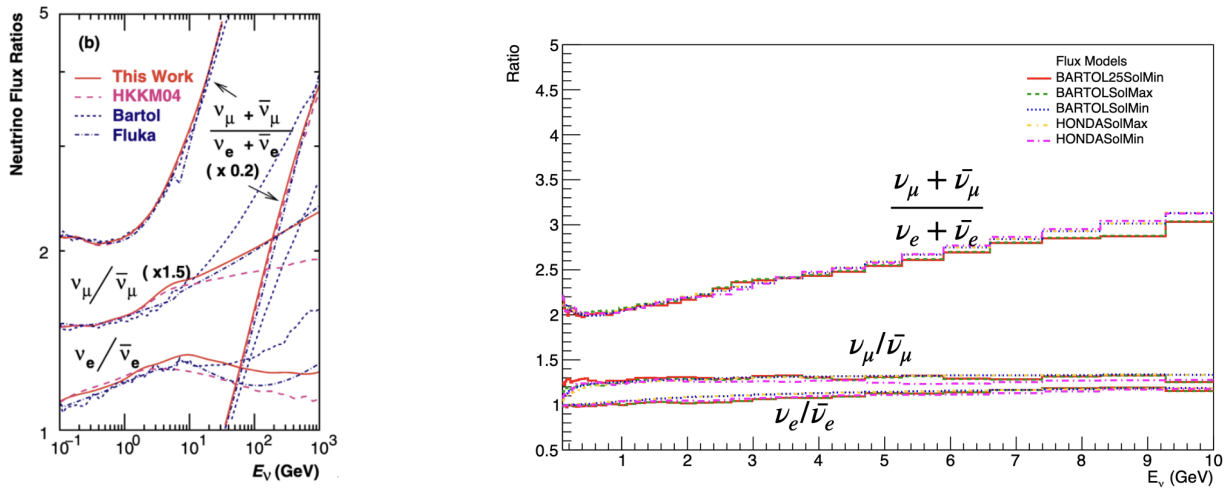

(a) Flux ratios from Ref. [51].

(b) Flux ratios from this work.

Figure 6.4: Comparison of neutrino-to-antineutrino flux ratios between the canonical Honda 2007 calculation [51] (left) and the present DUNE-atmospheric flux inputs (right). Both show the expected hierarchy $\nu_\mu/\bar{\nu}_\mu > \nu_e/\bar{\nu}_e$ and an increasing $(\nu_\mu+\bar{\nu}_\mu)/(\nu_e+\bar{\nu}_e)$ ratio with energy. The left panel is in log10 scale whereas the right panel is linear scale due to simulation up to 10 GeV. The agreement validates that the flux models used in this analysis reproduce established charge-sign asymmetries.

relevant in future analyses with $\nu/\bar{\nu}$ separation capabilities.

To further examine the zenith-angle dependence of the neutrino-to-antineutrino flux ratios, Fig. 6.5 shows energy-sliced ratios as a function of $\cos\theta_z$. The behavior is broadly consistent across all energies: the $\nu_\mu/\bar{\nu}_\mu$ ratio remains around 1.3–1.5, while $(\nu_\mu+\bar{\nu}_\mu)/(\nu_e+\bar{\nu}_e)$ increases gradually with energy, reaching values above 3 in the multi-GeV regime. These trends agree with expectations from pion and kaon production asymmetries and provide a useful cross-check of the flux model consistency. Although these ratios are not used as input systematics in this analysis, they help establish confidence that the employed flux models correctly capture the charge-sign asymmetry behavior seen in prior calculations.

The following subsection describes the atmospheric flux models used in this work. Their differences are later used to construct an error envelope that quantifies the uncertainty on the flux prediction as a function of energy and zenith angle.

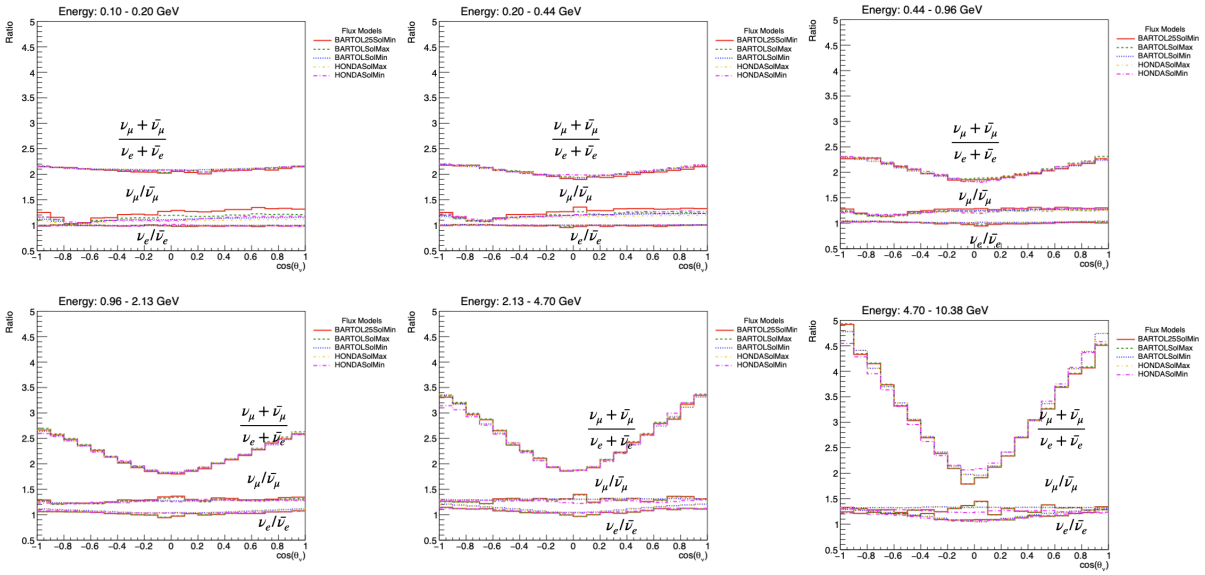

Figure 6.5: Neutrino-to-antineutrino flux ratios as a function of $\cos\theta_z$ in energy slices between 0.1 and 10 GeV. The curves show the $(\nu_\mu + \bar{\nu}_\mu)/(\nu_e + \bar{\nu}_e)$, $\nu_\mu/\bar{\nu}_\mu$, and $\nu_e/\bar{\nu}_e$ ratios predicted by the Honda and Bartol flux models under different solar-modulation conditions. The ratios show the expected increase with energy and toward horizontal directions, consistent with pion–kaon production asymmetries in the atmosphere.

6.1.2 Flux Uncertainty Estimation via Model Envelope

Unlike beam-based experiments, atmospheric analyses lack a near detector, and therefore rely entirely on theoretical flux predictions. To estimate the associated uncertainty, I compare independent flux calculations and define a model-spread envelope representing the maximal deviation across models, or maximum error envelope.

The nominal atmospheric neutrino flux model used in this analysis is the HondaSolarMinimum model [50] for solar-minimum conditions (the sun's eleven year activity cycle when solar activity is at its lowest, allowing more cosmic ray to enter solar system due to weaker magnetic field). To construct a robust uncertainty estimate, this baseline prediction is compared against two alternative models: the Bartol 2004 flux [32], based on earlier cosmic-ray fitting and hadronic production schemes, and a preliminary Bartol 2025 calculation currently under development.

Because these three flux models are made under independent simulations and physical assumptions, they provide a conservative and physically motivated uncertainty band. The resulting envelope is constructed by taking the maximum and minimum flux ratios (Model/Nominal) across all comparison models at each point in $(E_\nu, cos\theta_z)$ space. The angular dependence on the left panels of fig 6.6 and fig. 6.7 show consistent 10-11% deviation from nominal model. The energy on the right panels of fig 6.6 and fig. 6.7 can deviate to around 30% at sub-GeV regime, reflecting poor model accuracy at that energy range.

To use this flux systematic error envelope into the oscillation analysis, the error envelope is parameterized using ROOT TSpline3 interpolation function to obtain a smooth normalization. For each neutrino flavor and charge sign, the fractional deviation from the nominal Honda flux model is mapped as a smooth function of both energy and zenith angle.

These error envelope splines are used in MaCH3 [52] fitting framework (described below); they enter as a functional systematic parameter. At each step in the Markov Chain [47], the flux correction for a given event is evaluated by querying the appropriate spline at the event's true $(E_\nu, cos\theta_z)$ coordinates, and the resulting weight is applied as a multiplicative correction to the predicted event

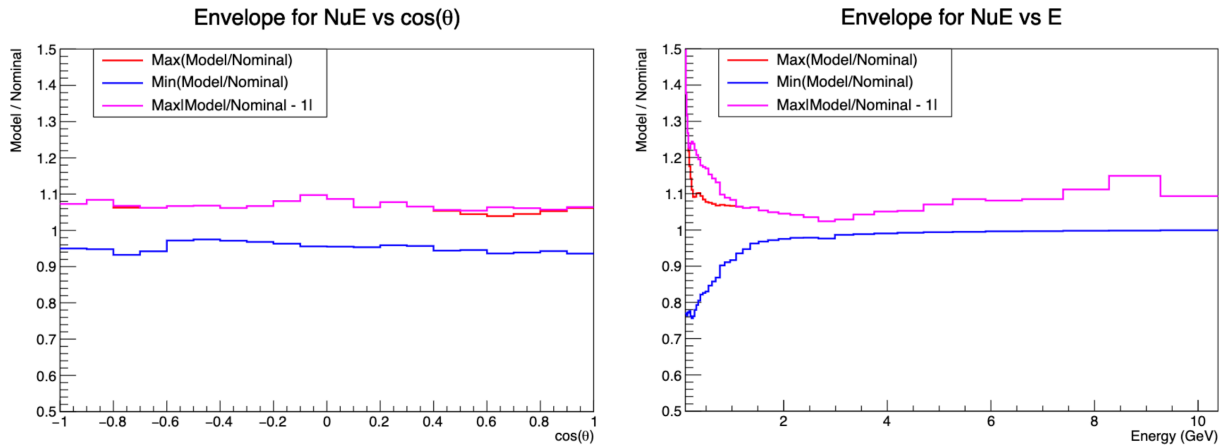

Figure 6.6: Flux error envelope for ν_e, as a function of $\cos\theta_z$(left) and neutrino energy(right). The red and blue lines indicate the maximum upward and downward deviations from the Honda nominal flux, while the magenta curve shows the maximum absolute deviation (MaxModel/Nominal - 1). The envelope reaches ∼20-30% at sub-GeV energies and narrows to ∼ 10% above 1 GeV

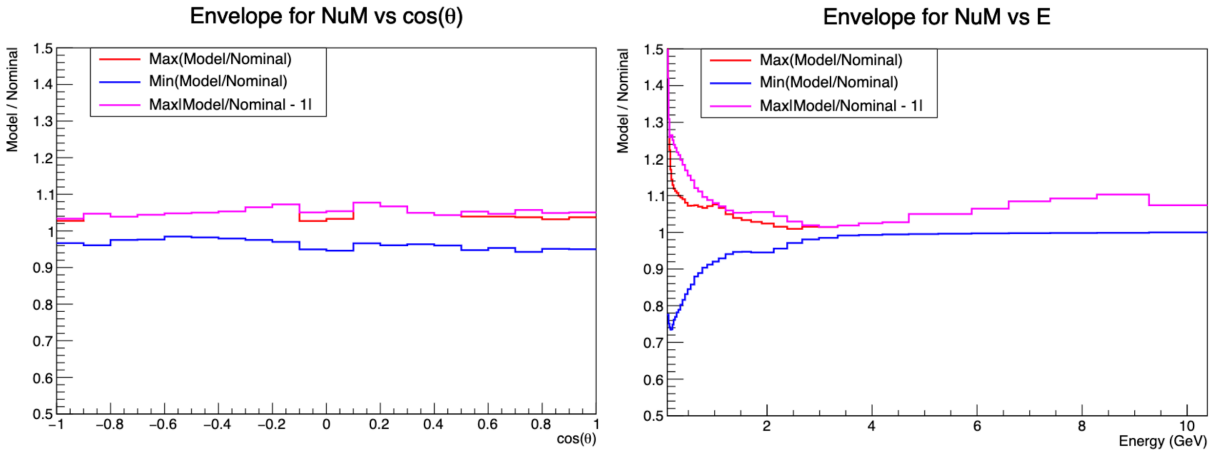

Figure 6.7: Flux error envelope for ν_μ, showing similar structure to the ν_e envelope with enhanced deviations in the sub-GeV region

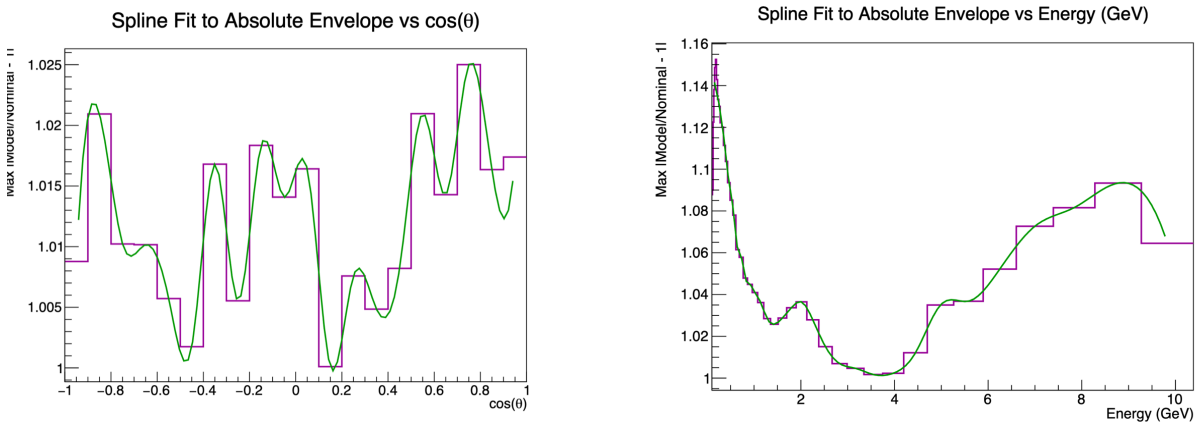

Figure 6.8: Parametrization of the maximum error envelope using TSpline3, over $cos\theta_z$ on the left panel and over energy on the right panel. The spline goes through the center of each bin. spline over zenith angle varies from 0.5% to 2%, where as energy spline reaches 14% at sub-GeV

rate. In addition to the energy and angle dependent spline corrections, a free normalization parameter $atmflux_0$ is utilized to capture an overall flux scale uncertainty common to all flavors. This parameter permits a uniform rescaling of the atmospheric flux across all energies and angles, and is constrained by a Gaussian prior. The prior width is configurable through the MaCh3 configuration files, typically set to reflect the $\sim 10-15\%$ absolute normalization uncertainty used by flux calculations. During the Markov Chain Monte Carlo (MCMC) sampling, which is covered in detail in Section 6.3.1, $atmflux_0$ is set to vary freely, with the Gaussian prior providing a penalty term that pulls the parameter toward its nominal value of 1.0 while still permitting data-driven adjustments to the overall flux scale. This treatment separates the spectral shape uncertainty (encoded in the spline and constrained by the error envelope) from the overall rate uncertainty (captured by $atmflux_0$). The flux systematic treatment implemented here represents a conservative approach that captures the current state of atmospheric flux modeling uncertainties, with the envelope based spline constraints preventing nonphysical spectral variations while allowing for realistic normalization flexibility.

6.2 NSI Signal Model

Before performing a full Bayesian analysis, it is important to verify that DUNE's atmospheric neutrino sample exhibits measurable sensitivity to NSI. This preliminary study evaluates whether NSI induced variations in the predicted event distributions exceed statistical uncertainties, therefore justifying the computational effort of a full systematic MCMC fit.

The analysis studies all NSI matter potential ε parameters. To assess observability, Monte Carlo predictions are generated for several representative NSI scenarios (ε = -0.1,0,0.1,0.2,0.3,0.5) and compared in the reconstructed L/E distributions in the DUNE far detector.

Figures 6.9 and 6.10 show the resulting variations for $\varepsilon_{e\tau}$ and $\varepsilon_{\mu\tau}$, respectively, in both ν_e and ν_μ event selections. The upper panels display absolute event rates, while the bottom ratio panels (normalized to $\varepsilon = 0.2$) quantify the fractional changes. For $|\varepsilon| \sim 0.5$, the variations reach 10-20% in the oscillation maximum region (L/E $\sim$ 500 km/GeV), well above the expected statistical uncertainties for a 10-year exposure of a 40 kton DUNE detector.

The key observation from these variations is that NSI effects produce L/E dependent distortions that are statistically significant and distinguishable from simple normalization uncertainties. This confirms that DUNE's atmospheric neutrino program has genuine sensitivity to flavor changing NSI parameters in the $|\varepsilon| \lesssim 0.3$ range, motivating the full systematic analysis described in the following sections.

6.3 Statistical Framework and Analysis Setup

6.3.1 Bayesian Method, MCMC

The search for NSI in DUNE's atmospheric neutrino sample uses Bayesian statistical framework implemented within the MaCh3 (Markov Chain 3-flavor) analysis package [28]. This approach

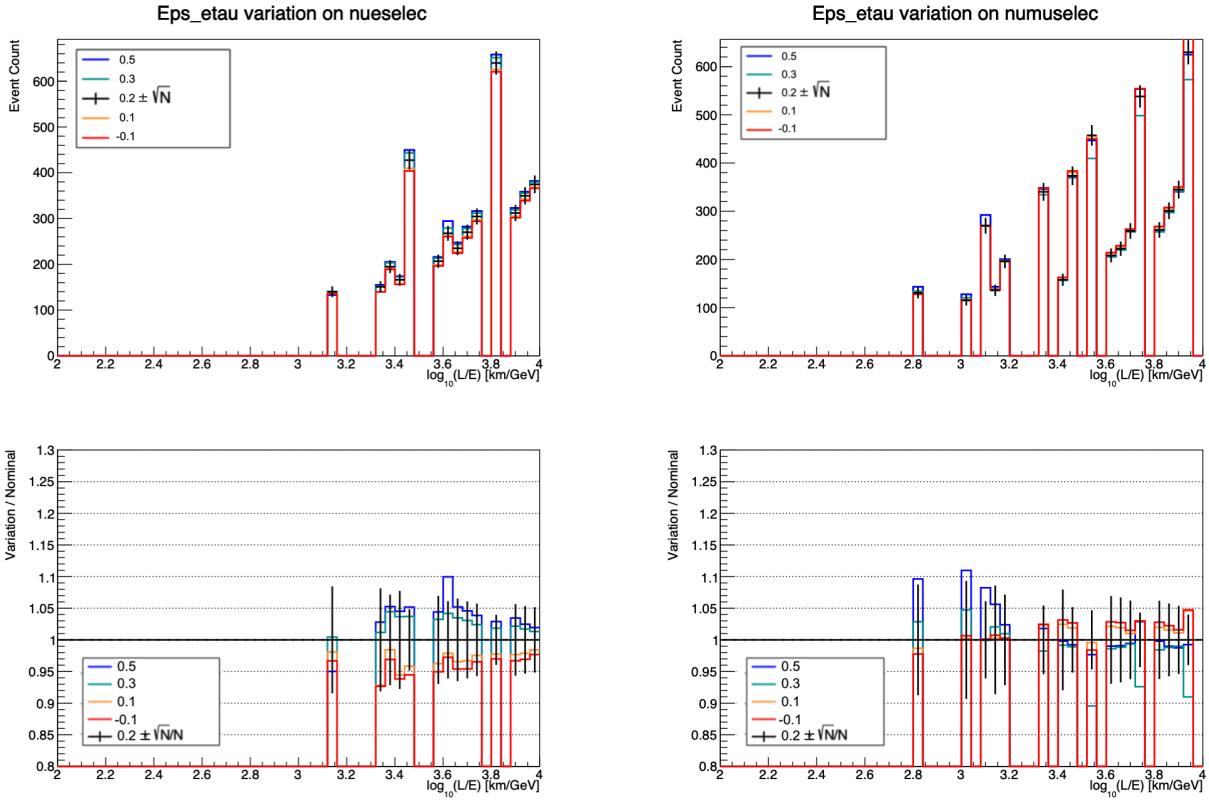

Figure 6.9: Event rate variation with $\varepsilon_{e\tau}$ set to -0.1, 0.1, 0.2, 0.3 and 0.5 (top panels), and variation divided by nominal $(\varepsilon_{e\tau}) = 0.2$ in ν_e (left) and ν_μ selections. Both ν_μ and ν_e channels show strong sensitivity, with clear L/E dependent structure in the ratio panels.

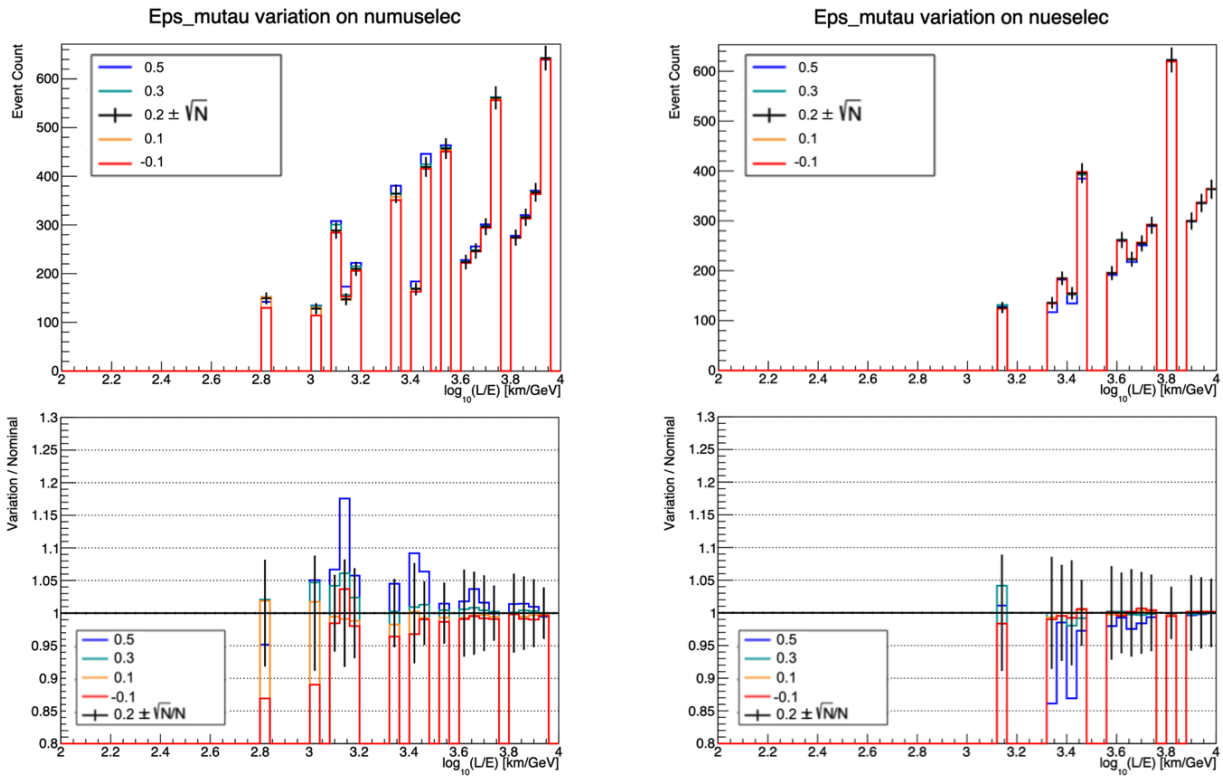

Figure 6.10: Event rate variation with $\varepsilon_{\mu\tau}$ set to -0.1, 0.1, 0.2, 0.3 and 0.5 (top panels), and variation divided by nominal ($\varepsilon_{\mu\tau}$) = 0.2 in ν_μ (left) and ν_e selections. The ν_μ channel shows particular strong sensitivity, with clear L/E dependent structure in the ratio panels.

enables simultaneous fitting of parameters of interest (NSI matter potential) and nuisance parameters, together with systematic uncertainties, with full propagation of parameter correlations and systematic constraints.

MaCh3 evaluates Bayes' theorem to perform model inversion. It tries to infer parameter $\vec{\theta}$ given a model that can predict the possible outcome of an experiment and an observed dataset $\vec{D}$.

$$P(\vec{\theta}|\vec{D}) = \frac{P(\vec{D}|\vec{\theta})P(\vec{\theta})}{P(\vec{D})} \tag{6.1}$$

Where $P(\vec{\theta}|\vec{D})$ is the joint posterior probability of the parameters $\vec{\theta}$ given the observed data $\vec{D}$. $P(\vec{D}|\vec{\theta}$ is the joint likelihood of observing the data given the model parameters, and $P(\theta)$ is the prior probability distribution of the parameters, and $P(\vec{D}$ is the marginal likelihood. The marginal likelihood is usually dropped because it is not dependent on the parameters $\vec{\theta}$. Therefore the MCMC method evaluates Bayes' theorem as a proportionality, and is sufficient for parameter inference and posterior sampling.

$$P(\vec{\theta}|\vec{D}) \propto P(\vec{D}|\vec{\theta}) \cdot P(\vec{\theta}), \tag{6.2}$$

6.3.2 Likelihood Construction

In this analysis, the observed data is the binned atmospheric neutrino event distribution in reconstructed L/E. The likelihood is calculated by comparing the Monte Carlo prediction for a given set of oscillation parameters with the data in each bin using a Poisson likelihood. Prior knowledge of systematic parameters are incorporated by modeling them as independent Gaussian variables with central values μ and prior width σ.

The posterior distribution is expressed in negative logarithmic space to reduce numerical volatility and computational cost.

$$\ln P(\vec{x}|\vec{\theta}) = -2\sum_{i=1}^{N}\left[E_i(\vec{\theta}) - O_i + O_i \ln\frac{O_i}{E_i(\vec{\theta})}\right] - \sum_j \frac{(\theta_j-\mu_j)^2}{\sigma_j^2}, \tag{6.3}$$

where O_i is the observed event count in bin i, $E_i(\vec{\theta})$ is the expected event rate in that bin given parameters $\vec{\theta}$, N is the total number of bins, and the second term represents independent Gaussian penalty constraints on the systematic parameters with prior widths σ_j. We sum over all bins in reconstructed energy and reconstructed zenith angle $(E_{reco}, cos\theta_{reco})$ for both ν_e and ν_μ atmospheric event selections.

The parameter $\vec{\theta}$ contains both NSI parameters of interest $(\varepsilon_{\mu\mu}, \varepsilon_{\mu\tau}, \varepsilon_{\tau\tau})$, standard oscillation parameters like $sin^2\theta_{23}$, and systematic nuisance parameters (atmospheric flux shape and normalization). For each Monte Carlo event, the predicted event rate is computed by applying oscillation probabilities with modification of NSI, atmospheric flux weights (including systematic variations), cross-section weights, and detector response corrections.

Markov Chain Monte Carlo Sampling

When the number of degrees of freedom is large, it becomes very difficult to calculate the posterior distribution of a given model and data. MaCh3 uses Markov Chain Monte Carlo (MCMC) sampling using the Metropolis-Hasting algorithm [47] to explore the posterior distribution efficiently. Metropolis-Hasting operates by constructing a Markov Chain where each step represents a point in parameter space $\vec{\theta}$, with transitions between states depending only on the current state.

At each MCMC step, a new parameter set $\vec{\theta}'$ is proposed form the current state $\vec{\theta}$ according to a proposal distribution. The proposal is then decided whether to be accepted with probability:

$$r(\vec{\theta}, \vec{\theta}') = \min\left(1, \frac{P(\vec{x}|\vec{\theta}')}{P(\vec{x}|\vec{\theta})}\right), \tag{6.4}$$

where $P(\vec{x}|\vec{\theta})$ is the posterior probability. If rejected, the chain remains at $\vec{\theta}$. This directed random

walk favors regions of higher posterior probability. After sufficient iterations, the chain converges to sampling from the target posterior distribution, allowing the extraction of credible intervals and marginalized parameter constraints.

Marginalization For the parameters of interest and nuisance parameters , the marginalized posterior for the parameters of interest is obtained by integrating over all nuisance parameters:

$$P(\vec{\theta}|\vec{x}) = \int P(\vec{\theta}, \vec{\delta}|\vec{x})\, d\vec{\delta}. \tag{6.5}$$

This Bayesian marginalization approach is different from the frequentist profiling method, which selects the maximum likelihood value for each nuisance parameter. Bayesian marginalization averages over the full parameter distribution. The Bayesian method projects the MCMC samples onto a single parameter axis, producing the marginalized posterior, with systematic uncertainties fully incorporated through the nuisance parameter variations explored during sampling.

Analysis Configuration

The analysis studies DUNE's sensitivity to flavor changing NSI parameters in the $\mu - \tau$ sector through Bayesian parameter estimation. The analysis tests the null hypothesis of standard three flavor oscillations by generating an Asimov dataset with all NSI parameters (except for ElecCoupling = 1 for NSI to be able to vary) to 0 ($\varepsilon_{\mu\mu} = \varepsilon_{\mu\tau} = \varepsilon_{\tau\tau} = 0$). NSI electric coupling parameter is fixed at standard value to enable NSI physics in the fit. The sensitivity is quantified by fitting this Asimov data and determining the posterior constraints on the NSI parameters. The posterior probability distribution over NSI parameter values is calculated given the observed (Asimov) data and prior beliefs. If the data support the null hypothesis, the posterior will peak near zero with narrow credible intervals. If NSI are present, the posterior will favor non-zero values.

The fit configuration is as follows:

- **NSI parameters ($\varepsilon_{\mu\mu}, \varepsilon_{\mu\tau}, \varepsilon_{\tau\tau}$)**: Free parameters with flat priors over the range [-0.5,+0.5][-0.3, +0.3][-0.5,+0.5].

- **Standard oscillation parameters**: Fixed to their NuFit 6.0 global best-fit values [13] (normal mass ordering assumed). except for $sin^2\theta_{23}$ which is free with central value at 0.451 and constraint of [0, 1].

- **Atmospheric flux systematics**: Free parameters with Gaussian priors as described in Section 6.1.2, including TSpline3 shape parameters and the `atmflux_0` global normalization.

The sensitivity is quantified through Bayesian credible intervals constructed from the marginalized posterior distributions. For NSI parameters ε, the 90% credible interval represents the range constraining 90% of the posterior probability mass when fitting the null hypothesis Asimov dataset, providing a measure of DUNE's constraining power on NSI with systematic uncertainties fully incorporated.

Standard MCMC convergence diagnostics were applied, including visual inspection of parameter trace plots to confirm proper mixing and stability, and examination of posterior distributions to ensure adequate sampling. Chains were run for 180,000 iterations with 30,000 burn-in steps discarded. The trace plots (e.g., Figure 6.11 for NSI parameters) show the characteristic horizontal band structure indicating good convergence and exploration of the parameter space. Additionally, split posterior comparisons (Figure 7.9) in section 7.2 shows consistent results between different segments of the chain (first half vs. second half, left vs. right), confirming the chain has reached equilibrium and is sampling the true posterior distribution.

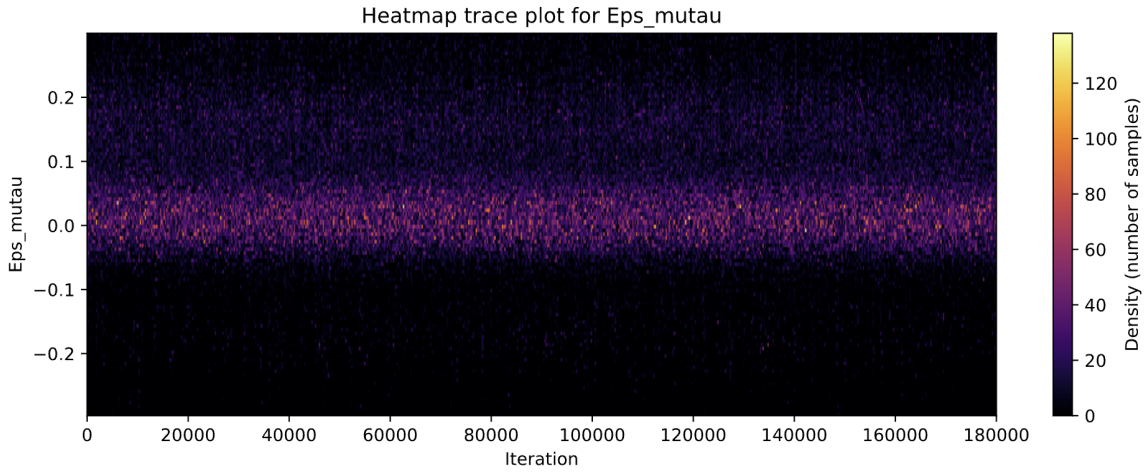

Figure 6.11: Trace plot for $\varepsilon_{\mu\tau}$, with 180,000 mcmc steps, and 30,000 burn in steps

Chapter 7

Results: Search for NSI with Atmospheric Neutrinos

7.1 NOvA Results

7.1.1 Part 1: Selection Efficiency

The atmospheric neutrino event selection was applied to eight years equivalent of NOvA far detector Monte Carlo, yielding 1062 total candidate events across both $\nu_e CC$ and $\nu_\mu CC$. In this analysis, two reconstruction strategies were used: one targeting electron neutrino interactions through electromagnetic shower identification, and another focusing on muon neutrino events via charged particle tracking.

The electron neutrino selection processed 2,748 simulated atmospheric events and achieved 7.3% selection efficiency, yielding 200 candidate events, with 1.9% neutral current contamination. The muon neutrino selection processed 2,642 simulated atmospheric events, and achieved 32.6% selection efficiency. It produced 862 candidates, with 3.7% neutral current contamination. Table 7.1 summarizes the selection efficiency performance and event yields for both neutrino flavors.

Table 7.1: Atmospheric neutrino event selection summary for 8 years of data taking

Parameter	ν_e CC	ν_μ CC
Expected Event Rates		
From flux $\times\sigma\times$ N $\times$ trigger	2,748	2,642
Simulated Events (before normalization)		
After NNBar trigger	3684	3549
Normalization factor	0.75	0.75
After Reconstruction Cuts and Containment Cut (with normalization)		
Signal events selected	200.0	861.8
NC contamination	3.8 (1.9%)	32.2 (3.7%)
Overall efficiency	7.3%	32.6%

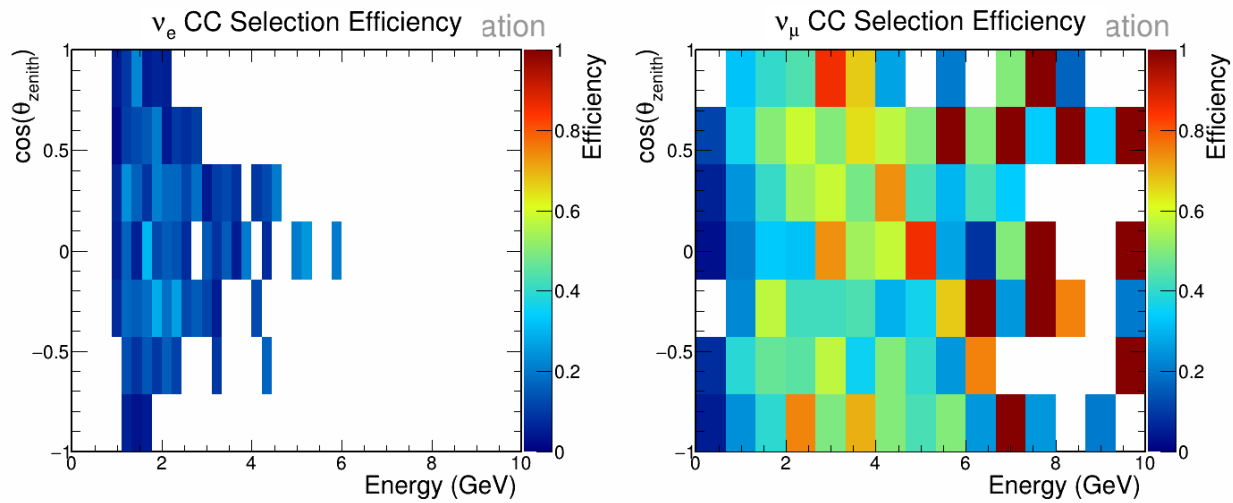

Figure 7.1: Left hand side shows the selection efficiency for $\nu_e CC$ atmospheric neutrinos. Right hand side shows the selection efficiency for $\nu_\mu CC$ events.

Figure 7.1 shows variations in selection efficiency across energy and zenith angle. The $\nu_e CC$ shows peak efficiency of approximately 15% selection efficiency at 1-2 GeV, which is more clearly shown on the 1D plot in Figure 7.2, dropping to less than 5% efficiency at higher energies, but it has a strong zenith angle dependence dependence as seen in Figure 7.3 left hand side, where efficiency is around 10% from $cos(\theta_{zenith})$ from -0.5 to 0.5, but drop to 1% for up coming neutrinos. The $\nu_\mu CC$ selection shows 30-40% efficiency across most energies, and exhibits little angular dependence, see Figure 7.3.

While the selection efficiencies demonstrate successful identification of atmospheric neutrino

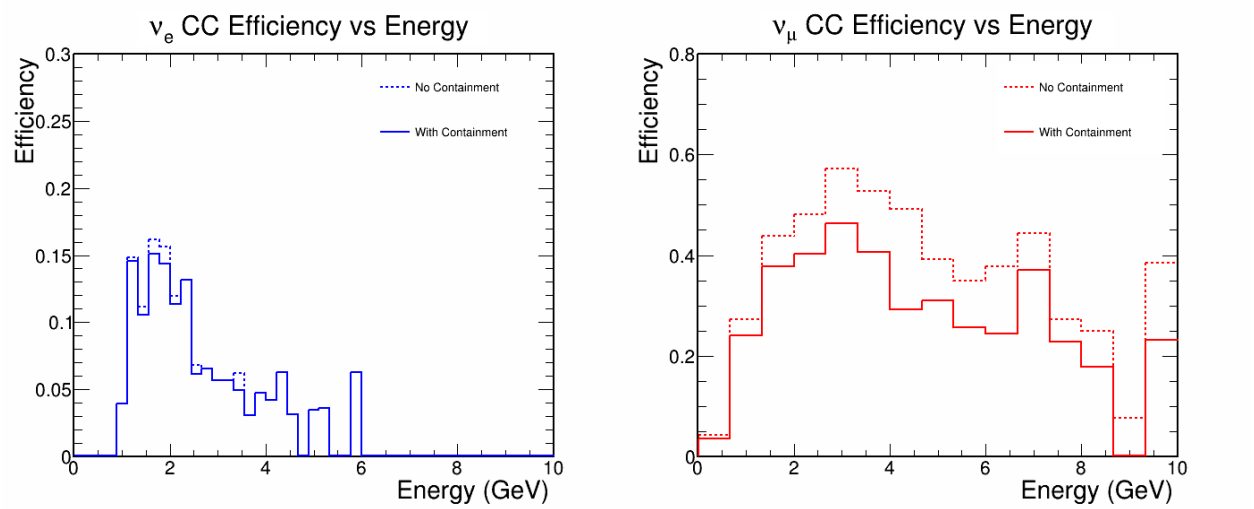

Figure 7.2: Left hand side shows $\nu_e CC$ selection efficiency projected to Energy axis. Right hand side shows $\nu_\mu CC$ selection efficiency projected to Energy axis

interactions, they do not account for the dominant challenge in surface level atmospheric neutrino detection: cosmic ray backgrounds. The cosmic ray flux at NOvA's FD surface location exceeds atmospheric neutrino rates by several orders of magnitude, making signal purity a critical factor in determining analysis feasibility.

7.1.2 Part 2: Purity

Using the cosmic background estimation method described in Section 5.4.2, the signal purity was evaluated for both neutrino selections. The cosmic background presents a fundamental limitation for atmospheric neutrino detection at NOvA far detector due to ground level setup with no shielding. Table 7.2 shows the dramatic impact of cosmic ray contamination on signal purity.

For ν_e-like events, the signal yields at 2.36% without the containment cut, and increases to 3.06% with the containment cut. The ν_μ-like events only have 0.0001% purity without the containment cut, and although they increase significantly to 0.0141% with the containment cut, they are still very low due to the number of cosmic muons that remain in the sample.

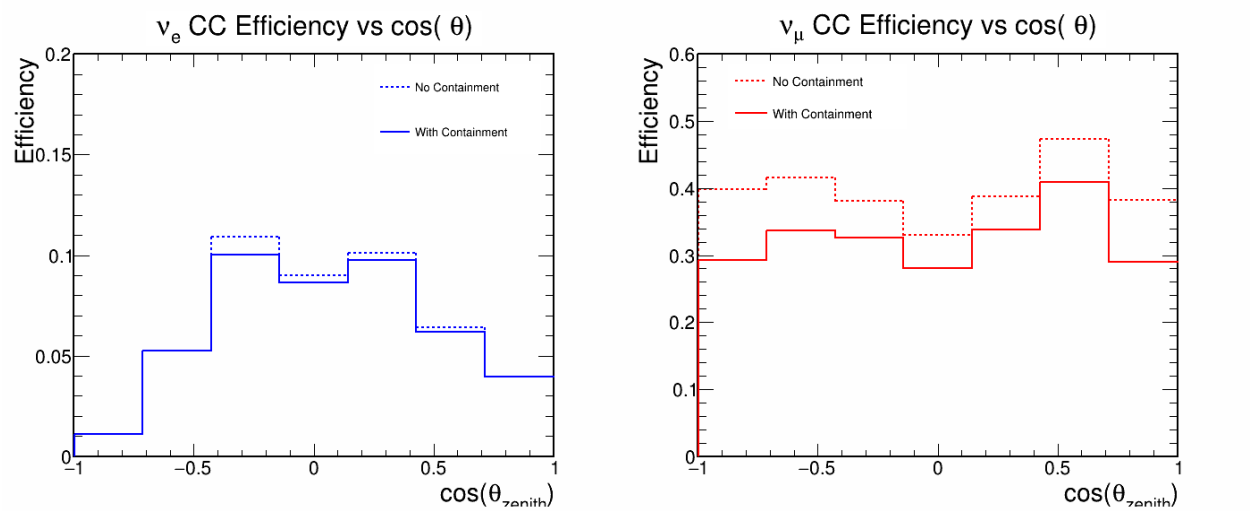

Figure 7.3: Selection efficiency for $\nu_e CC$ (left panel) and $\nu_\mu CC$ (right panel). ν_e CC shows more angular dependence , reaching 10% efficiency at $-0.25 < cos\theta_{zenith} < 0.5$. The $\nu_\mu CC$ has consistent selection efficiency around 30% through all angles, with little angular dependence.

These results show that, while atmospheric neutrino candidates can be identified, the large cosmic background strongly limits analysis sensitivity, particularly for the ν_μ channel, where purity remains below 0.02%.

Figure 7.4 shows neutrino signal purity for $\nu_e CC$ in a 2D distribution in reconstructed energy and $\cos\theta_{zenith}$ and fig. 7.5 shows signal purity for $\nu_\mu CC$. The left panels show purity without containment cuts, while the right panels include containment cuts. Purity is defined as the fraction of selected events that are true atmospheric neutrino signal rather than cosmic ray background. White bins indicate regions with insufficient Monte Carlo statistics due to limited event counts when binned in two dimensions.

For the $\nu_e CC$ selection (Figure 7.4), the purity shows strong energy dependence, reaching 70-100% in isolated bins above 2 GeV, where both signal and cosmic background are statistically limited. Below 2 GeV, the purity ranges from 10-40% in well-populated bins. The containment cut provides modest improvement, increasing the integrated purity from 2.4% up to 3.1%, primarily by reducing cosmic background at low energies. The angular dependence is relatively weak, with purity driven predominantly by the energy dependent cosmic rejection.

Table 7.2: Background composition and purity analysis

Component	ν_e**-like**	ν_μ**-like**
Signal Events (8 years)		
Atmospheric ν signal	200.0	861.8
Cosmic Ray Background		
No containment cut	9e+03	1e+09
With containment cut	6e+03	6e+06
Rejection factor	1.4×	172.1×
Purity		
Purity (no containment)	2.36%	0.0001%
Purity (with containment)	3.06%	0.0141%

For the $\nu_\mu CC$ selection (Figure 7.5), the purity is severely limited by the overwhelming cosmic ray background, with most populated bins showing purity below 1%. Regions of apparently high purity (yellow bins) reflect bins with 1-2 signal events and zero background rather than genuine signal dominance; these are statistical fluctuations rather than meaningful measurements, similar to the ν_e selection. The containment cut is essential, improving integrated purity from 0.001% to 0.014% through 172x cosmic rejection. Unlike the ν_e channel, the ν_μ channel has both energy and angular dependence, with upward-going events ($\cos\theta < 0$) showing slightly better purity as cosmic muons predominantly arrive from above.

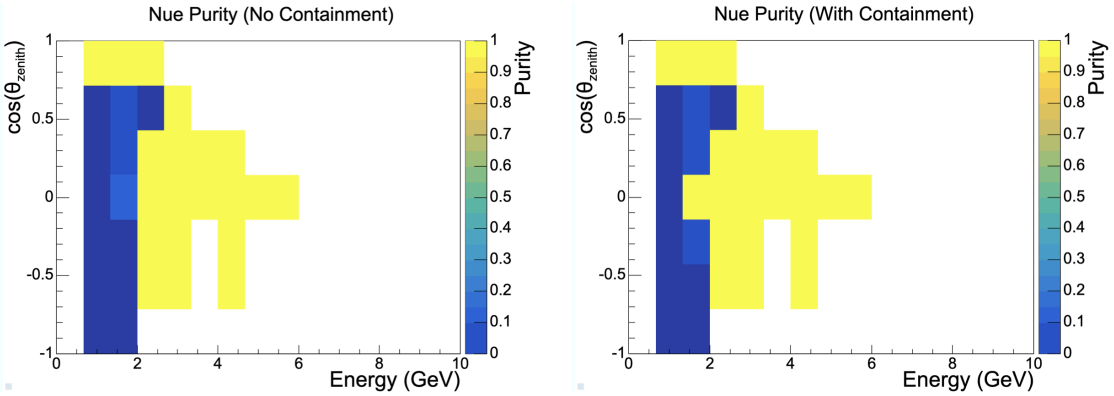

Figure 7.4: Left hand side shows $\nu_e CC$ purity without containment cut and right hand side shows the purity with containment cut (right)

The sparse population and prevalence of empty bins in these 2D distributions motivated the

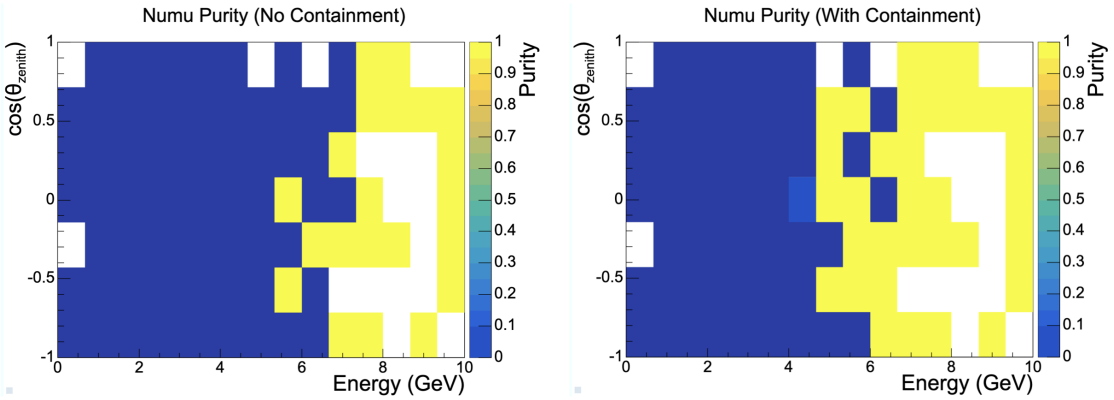

Figure 7.5: Left hand side shows $\nu_\mu CC$ purity without containment cut and right hand side shows the purity with containment cut (right)

use of 1D energy projections (7.6) to better visualize the signal to background relationship where statistics are sufficient.

Event rates are shown in figure 7.6 on a logarithmic scale for atmospheric neutrino signal and cosmic ray background as a function of reconstructed energy. Solid lines indicate selections with containment cuts applied, while dashed lines show selections without containment cuts. For the ν_e-like channel (left), the atmospheric neutrino signal (blue, $\approx$ 200 events) is suppressed by approximately two orders of magnitude relative to cosmic background (orange, $\approx$ 6,000 events), resulting in 3.1% purity with containment cuts. The containment requirement provides modest improvement, reducing cosmic background by 27% while retaining 96% of the signal. The selection cuts effectively suppress cosmic background above $\approx$2.3 GeV, leaving predominantly signal events at higher energies, though with limited statistics due to the steeply falling atmospheric neutrino flux. For the ν_μ-like channel (right), the signal to background rate is significantly worse. The atmospheric neutrino signal (red, $\approx$860 events) is overwhelmed by cosmic background (purple, $\approx$6 million events even after containment cuts), yielding only 0.014% purity. Therefore, the containment cut is essential, providing 172$\times$ cosmic rejection at the cost of 17% signal loss. The selection requirements become increasingly effective at rejecting cosmic background above 6 GeV, where

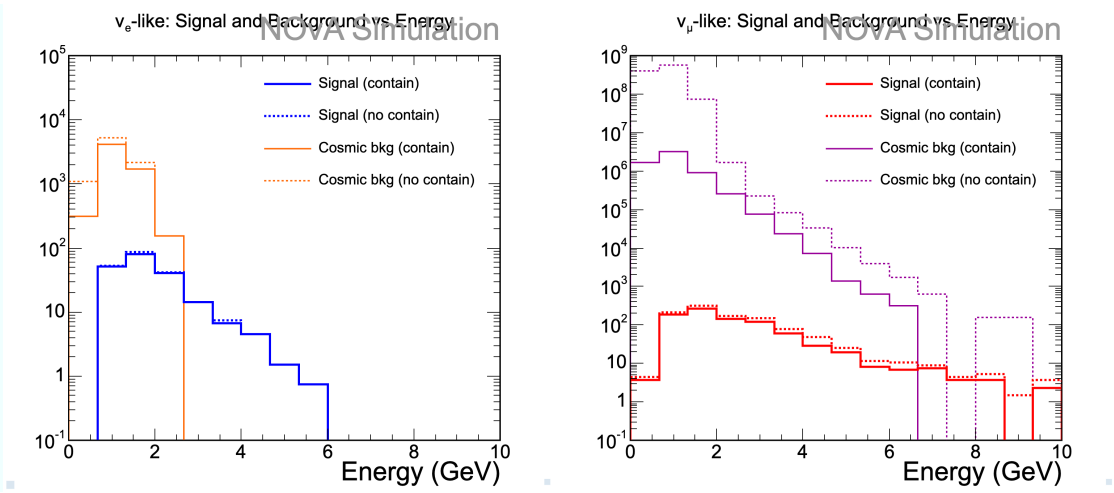

Figure 7.6: Left hand side plot shows ν_e like signal and background in log scale, with blue lines showing atmospheric neutrinos (signal) and orange lines showing cosmic background. Right hand side plot shows ν_e like signal and background in log scale, with red lines being neutrino signals, and purple lines being cosmic background.

signals begin to dominate, though absolute event rates remain limited. The energy dependent suppression of cosmic background demonstrates the effectiveness of the selection criteria, particularly at higher energies where reconstruction quality and particle identification become more discriminating.

These results demonstrate the key limitation for atmospheric neutrino analysis at surface level detectors. Although NOvA can achieve reasonable selection efficiency for both neutrino flavors, the analysis potential is severely constrained by cosmic ray contamination. For the electron neutrino sample, though the purity is only 3.1% purity, it may permit statistical analysis methods that can account for the substantial background contribution. However, the muon neutrino sample is more challenging to deal with: it has only 0.014% purity, 99.986% of selected events are cosmic rays. It would require advanced background subtraction techniques or alternative analysis approaches to deal with this level of contamination and to extract meaningful oscillation measurements. This selection is conducted using cosmic rejection developed for beam analysis, more refined cosmic rejection techniques could optimize signal purity for atmospheric neutrinos.

Table 7.3: Posterior summaries for the NSI parameters in the DUNE atmospheric neutrino analysis with flux systematics marginalized. For each parameter we quote the posterior mean, median, RMS width, and equal–tailed credible intervals at 68%, 90%, and 95% C.L. The corresponding one–sided 90% limits are $|\varepsilon_{\mu\mu}| < 0.394$, $|\varepsilon_{\mu\tau}| < 0.198$ and $|\varepsilon_{\tau\tau}| < 0.389$.

Parameter	Mean	Median	RMS	68% C.I.	90% C.I.	95% C.I.
$\varepsilon_{\mu\mu}$	0.010	0.019	0.238	[−0.256, 0.268]	[−0.394, 0.393]	[−0.439, 0.434]
$\varepsilon_{\mu\tau}$	0.060	0.041	0.094	[−0.020, 0.167]	[−0.060, 0.229]	[−0.120, 0.257]
$\varepsilon_{\tau\tau}$	0.0047	0.0148	0.235	[−0.259, 0.256]	[−0.396, 0.382]	[−0.438, 0.426]
$\varepsilon_{\tau\tau-\varepsilon_{\mu\mu}}$	-0.0062	-0.005	0.080	[−0.084, 0.074]	[−0.138, 0.119]	[−0.169, 0.141]

7.2 DUNE Results

This section presents the sensitivity of DUNE's atmospheric neutrino sample to non-standard neutrino interactions (NSI). Using a full Bayesian Markov Chain Monte Carlo (MCMC) analysis, constraints on the three NSI parameters $\varepsilon_{\mu\mu}$, $\varepsilon_{\mu\tau}$, and $\varepsilon_{\tau\tau}$ are obtained using Asimov data generated under the Standard Model hypothesis. Atmospheric neutrino events are oscillated using OscLib [29], with NSI strength parameters set to zero ($\varepsilon_{\mu\mu} = \varepsilon_{\mu\tau} = \varepsilon_{\tau\tau} = 0$); then MCMC fits are performed allowing NSI parameters to vary freely.

The MCMC fit then allows the 3 $\mu - \tau$ sector NSI parameters to vary freely, while the standard 3-flavor oscillation parameter $sin^2\theta_{23}$ is marginalized. This procedure yields the projected NSI sensitivity DUNE would obtain if real data showed no deviation from standard oscillations.

7.2.1 Constraints on NSI Parameters

Table 7.3 summarizes the 68%, 90% and 95% credible limits. The off-diagonal parameter $\varepsilon_{\mu\tau}$, which directly induces flavor-changing $\nu_\mu \leftrightarrow \nu_\tau$ interactions in matter, is the most strongly constrained:

- $|\varepsilon_{\mu\tau}| < 0.20$ (90% CL)
- $|\varepsilon_{\mu\mu}| < 0.39$ (90% CL)

- $|\varepsilon_{\tau\tau}| < 0.39$ (90% CL)

The diagonal parameters remain weakly constrained individually due to their intrinsic degeneracy: atmospheric neutrino oscillations depend primarily on the difference $(\varepsilon_{\mu\mu} - \varepsilon_{\tau\tau})$, yielding a one-dimensional allowed region in $(\varepsilon_{\mu\mu}, \varepsilon_{\tau\tau})$ space. This produces the observed strong correlation.

The atmospheric mixing angle is well recovered by the MCMC analysis,

$$\sin^2\theta_{23} = 0.477 \pm 0.038,$$

consistent with global oscillation fits. This demonstrates that allowing NSI parameters to vary does not bias the determination of standard oscillation parameters.

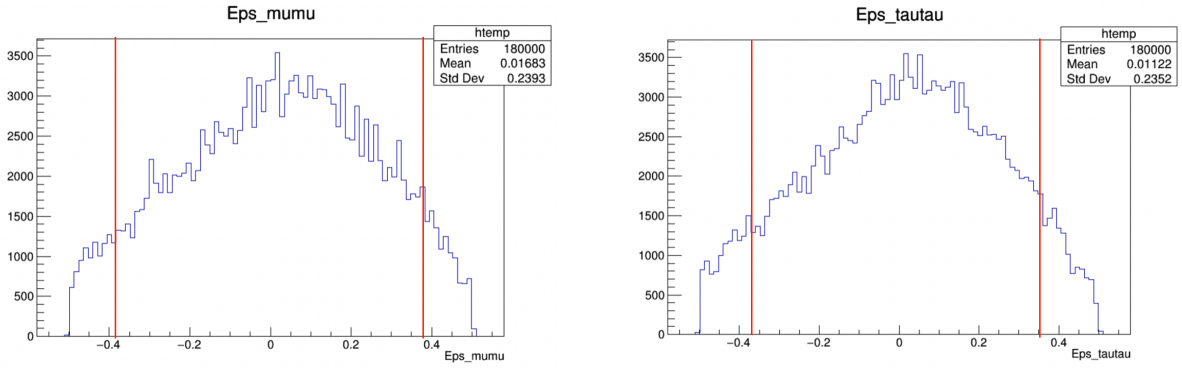

(a) $\varepsilon_{\mu\mu}$ posterior, with red lines representing 90% CL (b) $\varepsilon_{\tau\tau}$ posterior, with red lines representing 90% CL

Figure 7.7: $\varepsilon_{\mu\mu}$ and $\varepsilon_{\tau\tau}$ posterior, with red lines representing 90% CL

7.2.2 Correlation Structure and Parameter Degeneracies

A detailed analysis of the two-dimensional posteriors reveals the limiting degeneracies in atmospheric NSI measurements.

Strong $\varepsilon_{\mu\mu}$–$\varepsilon_{\tau\tau}$ correlation ($r = 0.94$). Only the difference $\varepsilon_{\mu\mu} - \varepsilon_{\tau\tau}$ enters the effective matter potential for atmospheric neutrinos. Consequently, the individual parameters are almost perfectly

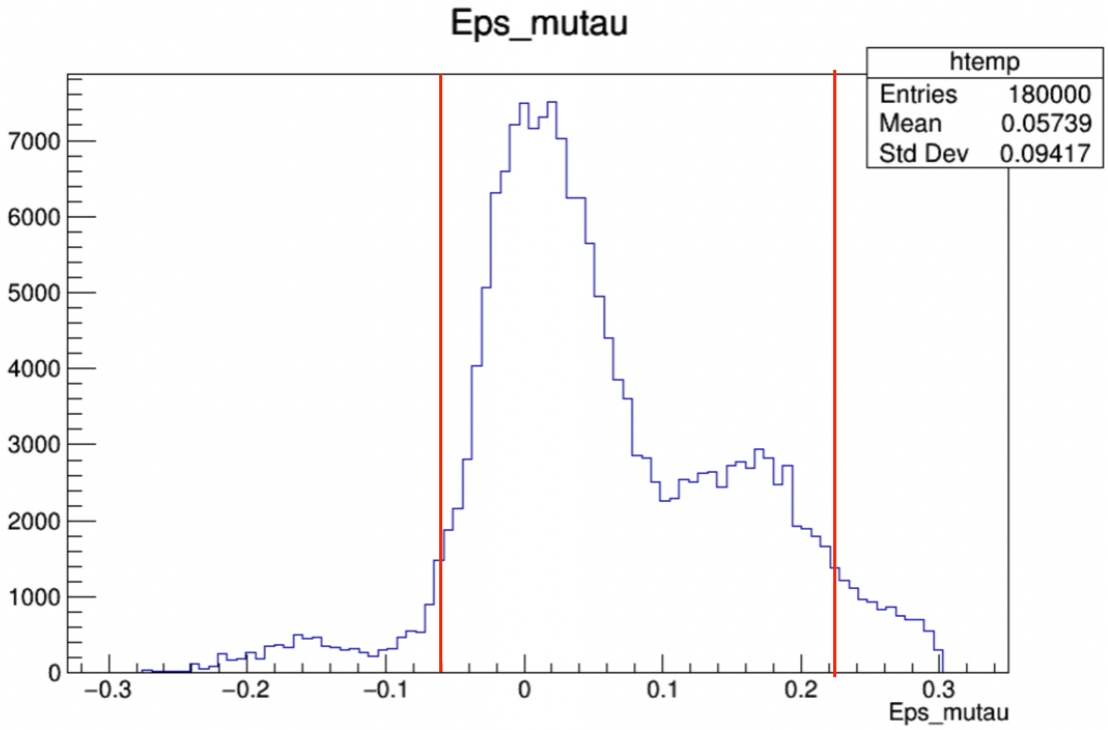

Figure 7.8: $\varepsilon_{\mu\tau}$ posterior, with red lines representing 90% CL

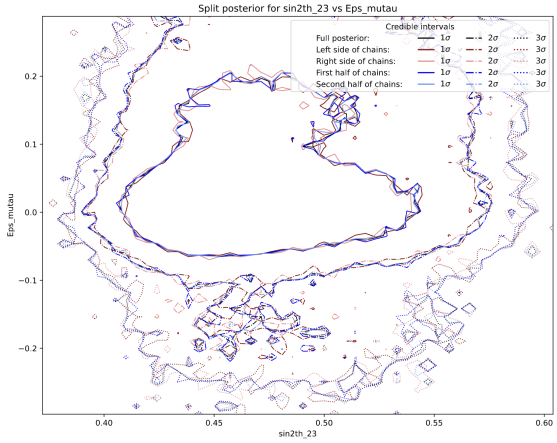

Figure 7.9: $sin^2\theta_{23}$ vs $\varepsilon_{\mu\tau}$ 2D posterior

correlated, and the diagonal NSI constraints are dominated by this degeneracy (Figure 7.10). Improving these constraints requires complementary data sets such as solar neutrinos or accelerator beams with different baselines.

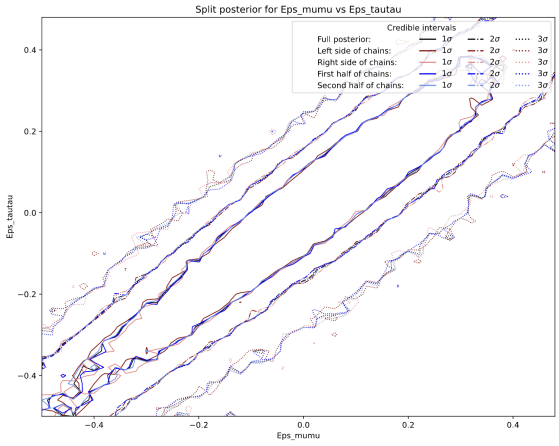

Figure 7.10: $\varepsilon_{\mu\mu}$ vs $\varepsilon_{\tau\tau}$ 2D posterior

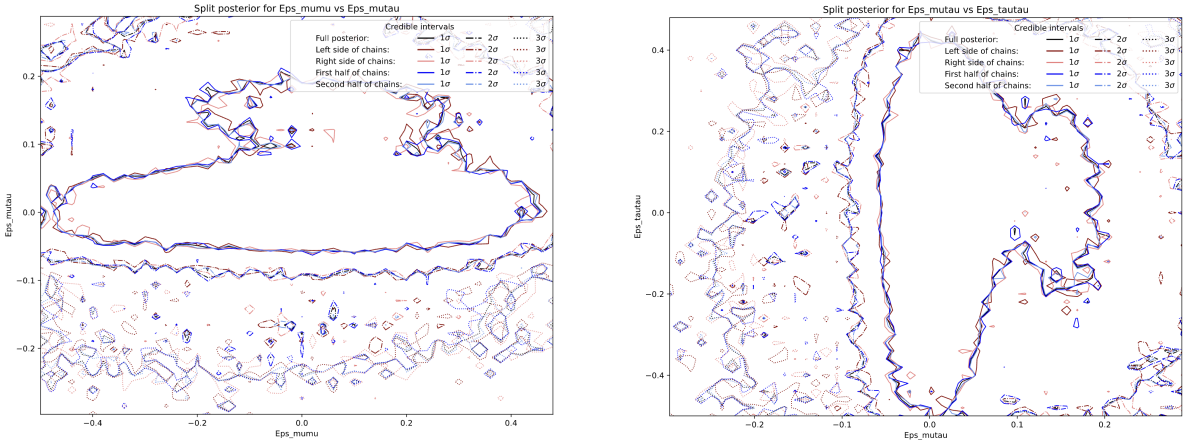

(a) $\varepsilon_{\mu\tau}$ vs $\varepsilon_{\mu\mu}$ posterior

(b) $\varepsilon_{\mu\tau}$ vs $\varepsilon_{\tau\tau}$ posterior

Figure 7.11: 2D posterior show negligible correlation between $\varepsilon_{\mu\tau} - \varepsilon_{\mu\mu}$ and $\varepsilon_{\mu\tau} - \varepsilon_{\tau\tau}$

Weak $\sin^2\theta_{23}$–$\varepsilon_{\mu\tau}$ correlation ($r = 0.15$). Both parameters affect the $\nu_\mu \to \nu_\tau$ transition probability, but atmospheric neutrino data largely disentangles their effects. The posterior shows a multi-lobe, non-Gaussian structure, yet the small linear correlation confirms that the constraint on $\varepsilon_{\mu\tau}$ is only mildly degraded (by $\sim$10%) due to this interaction.

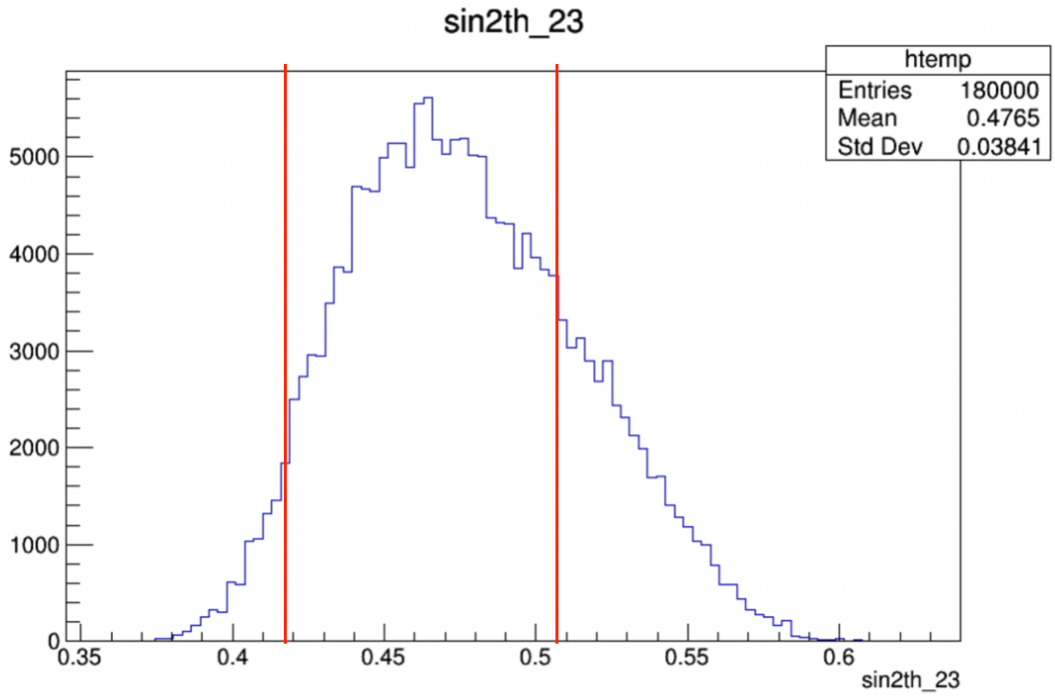

Figure 7.12: $sin^2\theta_{23}$ posterior, with red lines representing 90% CL

Negligible correlation between $\varepsilon_{\mu\tau}$ and diagonal NSI parameters. The correlations $r(\varepsilon_{\mu\mu}, \varepsilon_{\mu\tau}) = 0.016$ and $r(\varepsilon_{\tau\tau}, \varepsilon_{\mu\tau}) = 0.014$ indicate that the off-diagonal parameter varies independently from the diagonal terms. This explains why $\varepsilon_{\mu\tau}$ achieves a much stronger constraint than $\varepsilon_{\mu\mu}$ or $\varepsilon_{\tau\tau}$.

7.2.3 Impact of Systematic Uncertainties

To quantify the role of systematics, two MCMC analyses were performed: one with systematics fixed to nominal values, and one marginalizing over DUNE's current atmospheric flux systematics.

Table 7.4 shows that including systematics changes the posterior widths by only 1% (RMS) and less than 1% in the 90% credible region for all three parameters. This demonstrates that the NSI sensitivity could be statistics-limited, though other systematic effects have yet to be studied.

Table 7.4: Impact of atmospheric flux systematics on NSI parameter constraints. Shown are the RMS widths of the posterior distributions and the 90% credible interval one-sided limits, for analyses performed with systematics fixed to their nominal values (*No systematics*) and with flux systematics marginalized (*With systematics*).

	RMS Width			90% CL Limit		
Parameter	No Syst.	With Syst.	Change	No Syst.	With Syst.	Change
$\varepsilon_{\mu\mu}$	0.235842	0.238181	+1.0%	0.391406	0.393621	+0.6%
$\varepsilon_{\mu\tau}$	0.0928261	0.0937619	+1.0%	0.195977	0.197724	+0.9%
$\varepsilon_{\tau\tau}$	0.233105	0.234666	+0.7%	0.388237	0.389099	+0.3%

Table 7.5: Comparison of 90% credible/confidence intervals for NSI parameters from this work (DUNE 10-year projection) and current experimental constraints.

Parameter	DUNE Atm. (this work)	Super-K [53]	IceCube [54]	Global [18]
$\varepsilon_{\mu\tau}$	$[-0.060, +0.229]$	$[-0.046, +0.019]$	$[-0.0041, +0.0031]$	$[-0.0063, +0.016]$
$\varepsilon_{\mu\mu}$	$[-0.394, +0.393]$	—	—	$[-0.2, +0.1]$
$\varepsilon_{\tau\tau}$	$[-0.396, +0.382]$	—	—	$[-0.17, +0.093]$
$\varepsilon_{\tau\tau} - \varepsilon_{\mu\mu}$	$[-0.138, +0.119]$	$[-0.050, +0.138]$	—	$[-0.040, +0.047]$
Exposure	400 kton-yr	328 kton-yr	8 years livetime	Combined
Energy range	$<$10 GeV	Not mentioned	0.5–10 TeV	Multiple

7.2.4 Comparison with Existing Experimental Limits

To contextualize the DUNE atmospheric neutrino NSI sensitivity projections presented in this work, it is instructive to compare them with current experimental constraints from operating detectors and global analyses. Table 7.3 summarizes the 90% credible/confidence limits on key NSI parameters from this analysis alongside recent published results.

Super-Kamiokande Constraints

The Super-Kamiokande collaboration has reported constraints on flavor-diagonal and flavor-changing NSI parameters using 15 years of atmospheric neutrino data [53]. Their analysis yields 90% confidence limits of $\varepsilon_{\mu\tau} \in [-0.046, +0.019]$ and $\varepsilon_{\tau\tau} - \varepsilon_{\mu\mu} \in [-0.050, +0.138]$. The DUNE atmospheric sensitivity presented in this work yields 90% credible intervals of $\varepsilon_{\mu\tau} \in [-0.060, +0.229]$

and $\varepsilon_{\tau\tau} - \varepsilon_{\mu\mu} \in [-0.138, +0.119]$, which are comparable in magnitude though broader, particularly for $\varepsilon_{\mu\tau}$.

This difference is expected given that Super-Kamiokande's constraints benefit from 15 years of accumulated data, whereas the DUNE projections assume 10 years of exposure. Additionally, Super-Kamiokande uses neutrino energy over 10 GeV, providing higher event statistics than DUNE's atmospheric sample which only goes up to 10 GeV, though DUNE's liquid argon TPC technology is expected to offer excellent energy and angular resolution. The results are mutually consistent, with overlapping constraint regions.

IceCube High-Energy Constraints

The IceCube collaboration has reported significantly tighter constraints on $\varepsilon_{\mu\tau}$, with 90% confidence limits of $-0.0041 < \varepsilon_{\mu\tau} < 0.0031$ [54]. This analysis utilized 305,735 up-going ν_μ events spanning 500 GeV to $\sim$10 TeV, assuming universal NSI coupling to all first-generation quarks.

IceCube's superior sensitivity to $\varepsilon_{\mu\tau}$ arises from several factors. First, the enormous event statistics, more than two orders of magnitude greater than DUNE's projected atmospheric sample which provides substantially stronger statistical constraints. Second, at IceCube's high neutrino energies ($E_\nu \gtrsim 500$ GeV), matter effects accumulate over Earth through going baselines of up to 12,700 km, amplifying NSI-induced oscillation signatures. Third, the muon neutrino disappearance channel at these energies is particularly sensitive to $\varepsilon_{\mu\tau}$, which directly modifies $\nu_\mu \leftrightarrow \nu_\tau$ mixing in matter.

The DUNE atmospheric analysis presented here occupies a complementary energy regime (predominantly sub-10 GeV), where different systematic uncertainties dominate and where other NSI parameters may be more accessible. IceCube's high-energy constraints do not preclude the scientific value of measurements at lower energies, where oscillation physics and NSI effects manifest differently.

Global Fit Constraints

Recent global analyses combining results from atmospheric, accelerator, reactor, and solar neutrino experiments yield the current best constraints on NSI parameters [18]:

$$\varepsilon_{\mu\tau} \in [-0.0063, +0.016],$$
$$\varepsilon_{\mu\mu} \in [-0.2, +0.1],$$
$$\varepsilon_{\tau\tau} \in [-0.17, +0.093],$$
$$\varepsilon_{\tau\tau} - \varepsilon_{\mu\mu} \in [-0.040, +0.047].$$

The global fit constraints on $\varepsilon_{\mu\tau}$ are approximately an order of magnitude stronger than DUNE's projected atmospheric sensitivity. This is expected, as global fits leverage complementary information from multiple experiments spanning different energy regimes, baselines, and oscillation channels. The IceCube high energy constraints, in particular, strongly influence the global $\varepsilon_{\mu\tau}$ limit.

For the diagonal combinations $\varepsilon_{\mu\mu}$, $\varepsilon_{\tau\tau}$, and $\varepsilon_{\tau\tau} - \varepsilon_{\mu\mu}$, DUNE's projected constraints are comparable to global limits, indicating that DUNE atmospheric neutrinos could provide meaningful contributions to future global NSI analyses, particularly if exposure is extended beyond 10 years or if we can include the atmospheric sample over 10 GeV, or if the atmospheric flux systematic uncertainties can be further reduced.

Context and Future Prospects

The comparison reveals that DUNE's standalone atmospheric neutrino program, while not competitive with current leading constraints on $\varepsilon_{\mu\tau}$ from IceCube, provides complementary sensitivity at lower energies where systematic uncertainties and oscillation physics differ substantially.

Future improvements could arise from: (1) extended exposure beyond 10 years as DUNE accumulates data, (2) use of atmospheric neutrinos over 10 GeV, (3) refined atmospheric flux models with reduced model spread, (4) joint analyses combining DUNE's atmospheric and beam neutrino samples to constrain shared systematic parameters, or (5) incorporation of DUNE data into global NSI fits where complementarity between experiments strengthens combined constraints.

Chapter 8

Conclusion and Outlook

This dissertation presents the first full attempt to perform an atmospheric neutrino analysis using the NOvA Far Detector and provides a complete evaluation of the feasibility of atmospheric neutrino measurement in a surface level detector. Through detailed simulation, reconstruction studies and background modeling, I demonstrate that the overwhelming cosmic ray background at NOvA prevents atmospheric neutrino from being isolated with sufficient purity to enable competitive physics measurements. This negative results is itself an important finding, as it establishes a definitive understanding of the limitations of atmospheric neutrino studies in NOvA and clarifies why such analyses have not been pursued previously.

Building on the analysis framework developed for NOvA, this dissertation then performs a full sensitivity study for DUNE atmospheric neutrinos, where the deep underground environment eliminates the background limitations present in NOvA. Using the standard atmospheric neutrino analysis infrastructure for DUNE but extended to include NSI effects, I obtain the first full Bayesian constraints on NSI parameters for DUNE atmospheric neutrinos. These DUNE results represent the main physics outcome of this dissertation and demonstrate the powerful capability of DUNE's atmospheric sample for probing nonstandard interactions and possibly other beyond Standard Model signatures.

8.1 NOvA Conclusion

The NOvA atmospheric neutrino study carried out in this dissertation represents the first complete attempt to evaluate the feasibility of atmospheric neutrino measurements in the NOvA Far Detector. Through full Monte Carlo production with realistic cosmic overlay, a data-driven trigger model, and reconstruction tuned for atmospheric neutrino topologies, this work establishes a definitive understanding of the capabilities and limitations of performing atmospheric physics at a surface-level detector.

The analysis demonstrates that atmospheric neutrinos can be reconstructed with reasonable energy resolution for both electron and muon neutrinos, and that an adapted NNBar-based trigger is capable of identifying candidate events with non-negligible efficiency. However, the study also reveals two fundamental challenges that prevent NOvA from producing competitive atmospheric neutrino measurements:

- 1. Overwhelming cosmic background, which exceeds the atmospheric signal by $O(10^1)$ to $O(10^4)$ depending on channel, leading to final sample purities of only $\sim 3\%$ for ν_e candidates and $< 0.1\%$ for ν_μ candidates even after aggressive background rejection.

- 2. Intrinsic reconstruction limitations, most notably the directional bias affecting muon-neutrino events due to algorithms trained on forward-going beam neutrinos rather than isotropic atmospheric events. The resulting wrong-direction reconstruction for a large fraction of ν_μ interactions severely compromises the L/E resolution required for oscillation physics.

These results make it clear why atmospheric neutrino analyses have not been attempted in NOvA before. Given the detector's surface location and the way its reconstruction was designed, NOvA simply cannot reach the purity or resolution required for meaningful oscillation or NSI measurements with atmospheric neutrinos.

Even though the measurement isn't feasible at NOvA, the tools built here are still useful for DUNE and other experiments. The simulation chain, background modeling methodology, and

identification of reconstruction failure modes developed here offer concrete guidance for liquid-argon detectors and future near-surface experiments. This analysis is attempted to use all of the data NOvA has collected to improve NSI sensitivity before the next generation detectors like DUNE turns online.

8.2 DUNE Conclusion

Here I perform the first full sensitivity study for nonstandard neutrino interaction (NSI) using simulated DUNE atmospheric neutrino Monte Carlo and a full Bayesian Markov Chain Monte Carlo (MCMC) framework. Using a 15 million event atmospheric Monte Carlo sample corresponding to 400 kt·yr exposure, I obtained quantitative constraints on three NSI parameters and characterized the multi parameter structure governing DUNE's atmospheric NSI sensitivity.

8.2.1 Summary of Findings

The analysis yields the following 90% credible limits:

- $|\varepsilon_{\mu\tau}| < 0.2$
- $|\varepsilon_{\mu\mu}| < 0.39$
- $|\varepsilon_{\tau\tau}| < 0.39$

These constraints are derived under the Standard Model (SM) null hypothesis using Asimov atmospheric data oscillated with $\varepsilon_{\alpha\beta} = 0$. The Bayesian fit then allows all three $\mu - \tau$ sector NSI parameters to vary freely, with the standard NSI charge current coupling fixed to enable NSI propagation effects. These results therefore represent DUNE's projected sensitivity in the absence of true nonstandard interactions.

The off-diagonal parameter $\varepsilon_{\mu\tau}$ is well constrained shown in fig. (7.8). It directly induces flavor changing $\nu_\mu \leftrightarrow \nu_\tau$ interactions in matter, giving it a unique signature in the oscillation probability. I find that$\varepsilon_{\mu\tau}$ shows:

- weak correlation with the mixing angle $\sin^2\theta_{23}$, (r = +0.15) fig. 7.9
- negligible correlation with the diagonal NSI parameters (r$\approx 0.01-0.02$) fig. 7.2.2

allowing a measurement largely independent of other oscillations or NSI parameters.

The diagonal NSI parameters $\varepsilon_{\mu\mu}$ and $\varepsilon_{\tau\tau}$ fig. 7.2.2 are limited mainly by a well known degeneracy: $P_{\mu\mu}, P_{\tau\tau} \propto (\varepsilon_{\mu\mu} - \varepsilon_{\tau\tau})$, which produces a narrow band in $(\varepsilon_{\mu\mu}, \varepsilon_{\tau\tau})$ space. The correlation coefficient is very strong at $r(\varepsilon_{\mu\mu}, \varepsilon_{\tau\tau}) = +0.94$ fig. 7.10 As a result, the atmospheric sample cannot independently determine these two parameters, and their posteriors remain broad and nearly identical in width.

The posterior distribution of $\sin^2\theta_{23}$ fig. 7.12 is recovered as $\sin^2\theta_{23} = 0.477 \pm 0.038$, which is consistent with global oscillation fits. This result confirms that marginalizing over NSI parameters does not bias the atmospheric mixing angle determination.

8.2.2 Statistics Limited Sensitivity

From the comparison I find that the DUNE atmospheric NSI measurements is expected to be statistics limited, not systematics limited. I performed two full analyses: one without systematics, and another one with full marginalization over atmospheric flux systematics. The posterior width changes by only 1% in RMS, and less than 1% in the 90% CL limits. This demonstrates that the flux systematics considered here do not limit the sensitivity. However, I note that this study includes only the dominant class of atmospheric–flux uncertainties; additional sources of systematic uncertainty will need to be evaluated in future work.

The limiting factors are therefore:

- for $\varepsilon_{\mu\tau}$: finite atmospheric statistics

- for $\varepsilon_{\mu\mu}$ and $\varepsilon_{\tau\tau}$: the intrinsic parameter degeneracy.

This suggests what would help most in improving the measurement: For $\varepsilon_{\mu\tau}$, sensitivity will scale primarily with additional atmospheric exposure and can benefit from joint analysis with beam experiments that better separate $\sin^2\theta_{23}$ from NSI effects. For diagonal NSI parameters, it would require fundamentally new information, such as solar neutrino or accelerator experiments with different matter profiles to break the $\varepsilon_{\mu\mu}$–$\varepsilon_{\tau\tau}$ symmetry.

8.2.3 Outlook

Atmospheric neutrinos form a powerful, independent channel for probing new physics in DUNE. This analysis establishes a quantitative baseline for NSI searches and demonstrates that DUNE's atmospheric sample can provide competitive constraints on flavor changing NSI. As DUNE accumulates real data and combines atmospheric and beam samples, the sensitivity to $\varepsilon_{\mu\tau}$ can improve substantially, enabling a broad and robust physics program targeting nonstandard neutrino interactions and other beyond standard model effects.

Chapter 9

Appendix

9.1 Monte Carlo Production Details

This appendix provides technical details for reproducing the atmospheric neutrino Monte Carlo sample used in this analysis.

9.1.1 Software Environment

- NOvA software release: [version] - GENIE version: v3.04.00 - Spline set: AR2320i00000-k250-e1000 - GEANT4 version: [version]

9.1.2 Atmospheric Flux Files

Bartol atmospheric flux files are stored at:

`/cvmfs/nova.osgstorage.org/analysis/exotics/atmflux/v1.0.0`

9.1.3 Event Generation

Atmospheric neutrino events are generated using the `prodgenie_atmnu.fcl` configuration with the following key parameters:

- Maximum events per job: 1000
- Flux copy method: DIRECT
- Output format: artdaq

9.1.4 Cosmic Ray Overlay

Cosmic rays are overlaid using the `cosmic_overlay_detsim.sh` script with cosmic data from dataset `alister1_artdaq_fd_cosmics_p1235910_prod5p1`.
The reconstructed cosmic data used in this thesis is

`prod_caf_R20-11-25-prod5.1reco.q.t_fd_cosmic_fhcfd_cosmic_fhc_period10_v1_goodruns_nostale`

9.1.5 Grid Job Submission

Monte Carlo production was performed using the NOvA grid submission framework with the template `fd_genie_g4_prod6_atmnu.template.fcl`. A total of 100 grid jobs were submitted, each generating 1000 events.

9.1.6 Output Samples

Final Monte Carlo samples are stored in SAMweb definition: `muyuanh_atmnu_cosmic_100fcl`

Table 9.1: Selection efficiency as a function of neutrino energy and zenith angle

Kinematic Range	ν_e CC Eff.	ν_μ CC Eff.
Efficiency by Energy		
0.9–1.1 GeV	3.9%	27.3%
1.1–1.3 GeV	14.8%	27.3%
1.3–1.6 GeV	11.2%	43.8%
1.6–1.8 GeV	16.2%	43.8%
1.8–2.0 GeV	15.6%	43.8%
2.0–2.2 GeV	11.9%	48.2%
2.2–2.4 GeV	13.2%	48.2%
2.4–2.7 GeV	6.8%	48.2%
2.7–2.9 GeV	6.5%	57.1%
2.9–3.1 GeV	5.7%	57.1%
3.1–3.3 GeV	5.7%	57.1%
3.3–3.6 GeV	6.2%	52.8%
3.6–3.8 GeV	3.0%	52.8%
3.8–4.0 GeV	4.8%	52.8%
4.0–4.2 GeV	4.2%	49.2%
4.2–4.4 GeV	6.2%	49.2%
4.4–4.7 GeV	3.1%	49.2%
4.9–5.1 GeV	3.4%	39.3%
5.1–5.3 GeV	3.6%	39.3%
5.8–6.0 GeV	6.2%	34.9%
Efficiency by $\cos(\theta_{zenith})$		
-1.00 to -0.71	1.1%	39.9%
-0.71 to -0.43	5.3%	41.6%
-0.43 to -0.14	10.9%	38.1%
-0.14 to 0.14	9.0%	33.0%
0.14 to 0.43	10.1%	38.7%
0.43 to 0.71	6.4%	47.3%
0.71 to 1.00	4.0%	38.3%

Bibliography

[1] R. Davis, D. S. Harmer, and K. C. Hoffman. “Search for Neutrinos from the Sun”. In: *Phys. Rev. Lett.* 20 (1968), pp. 1205–1209.

[2] K. S. Hirata et al. “Observation of ^{8}B Solar Neutrinos in the Kamiokande-II Detector”. In: *Phys. Rev. Lett.* 63 (1989), p. 16.

[3] Y. Fukuda et al. “Evidence for Oscillation of Atmospheric Neutrinos”. In: *Phys. Rev. Lett.* 81 (1998), p. 1562.

[4] J. N. Abdurashitov et al. “Measurement of the Solar Neutrino Capture Rate by SAGE and Implications for Neutrino Oscillations in Vacuum”. In: *Phys. Rev. Lett.* 83 (1999), p. 4686.

[5] Q. R. Ahmad and et al. (SNO Collaboration). “Measurement of the rate of + d $\rightarrow$ p + p + e interactions produced by B solar neutrinos at the Sudbury Neutrino Observatory”. In: *Physical Review Letters* 87 (2001), p. 071301.

[6] Q. R. Ahmad and et al. (SNO Collaboration). “Direct evidence for neutrino flavor transformation from neutral-current interactions in the Sudbury Neutrino Observatory”. In: *Physical Review Letters* 89 (2002), p. 011301.

[7] K. S. Hirata, T. Kajita, T. Kifune, et al. “Experimental Observation of the Atmospheric Neutrino Anomaly”. In: *Physical Review Letters* 61 (1988), pp. 1537–1540.

[8] Y. Ashie et al. “Evidence for an oscillatory signature in the atmospheric neutrino oscillation”. In: *Phys. Rev. Lett.* 93 (2004), p. 101801.

[9] Z. Maki, M. Nakagawa, and S. Sakata. “Remarks on the Unified Model of Elementary Particles”. In: *Progress of Theoretical Physics* 28.5 (1962), pp. 870–880.

[10] B. Pontecorvo. “Inverse beta processes and nonconservation of lepton charge”. In: *Soviet Physics JETP* 7 (1958), pp. 172–173.

[11] L. Wolfenstein. “Neutrino oscillations in matter”. In: *Physical Review D* 17 (1978), pp. 2369–2374.

[12] S. P. Mikheyev and A. Yu. Smirnov. “Resonance amplification of neutrino oscillations in matter and solar neutrino spectroscopy”. In: *Soviet Journal of Nuclear Physics* 42 (1985), pp. 913–917.

[13] Ivan Esteban et al. “NuFIT-6.0: Updated global analysis of three-flavor neutrino oscillations”. In: *JHEP* 12 (2024), p. 216.

[14] Tommy Ohlsson. “Status of non-standard neutrino interactions”. In: *Rept. Prog. Phys.* 76 (2013), p. 044201.

[15] M. A. Acero et al. “Search for CP-Violating Neutrino Nonstandard Interactions with the NOvA Experiment”. In: *Phys. Rev. Lett.* 133.20 (2024), p. 201802.

[16] O. G. Miranda and H. Nunokawa. “Non standard neutrino interactions: current status and future prospects”. In: *New J. Phys.* 17 (2015), p. 095002.

[17] A. Blondel et al. “Electroweak parameters from a high statistics neutrino nucleon scattering experiment”. In: *Zeitschrift für Physik C – Particles and Fields* 45 (1990), pp. 361–379.

[18] Pilar Coloma et al. “Global constraints on non-standard neutrino interactions with quarks and electrons”. In: *JHEP* 11 (2023). Updates and extends arXiv:1805.04530 and arXiv:2204.03011, p. 033.

[19] Ivan Esteban et al. “Updated Constraints on Non-Standard Interactions from Global Analysis of Oscillation Data”. In: *Journal of High Energy Physics* 08 (2018), p. 180.

[20] Fermilab. *Fermilab Accelerator Complex*. Fermi National Accelerator Laboratory. Accessed: <your access date>. 2021.

[21] Travis Grant Olson. “Measurement of $d^2\sigma/d|\vec{q}|\,dE_{\text{avail}}$ and 2p2h contribution using charged-current ν_μ scattering in the NOvA Near Detector”. Ph.D. thesis. Fermi National Accelerator Laboratory (Fermilab), 2021.

[22] D. S. Ayres et al. “NOvA: Proposal to Build a 30 Kiloton Off-Axis Detector to Study $\nu_\mu \to \nu_e$ Oscillations in the NuMI Beamline”. In: (Mar. 2004).

[23] Dung Duc Phan. “A search for neutron-antineutron oscillation in the NOvA experiment”. PhD thesis. Texas U., Texas U., 2020.

[24] Babak Abi et al. “Deep Underground Neutrino Experiment (DUNE), Far Detector Technical Design Report, Volume I Introduction to DUNE”. In: *JINST* 15.08 (2020), T08008.

[25] Babak Abi et al. “Deep Underground Neutrino Experiment (DUNE), Far Detector Technical Design Report, Volume II: DUNE Physics”. In: (Feb. 2020).

[26] João Coelho et al. *OscProb: exact neutrino oscillation probability computation package (v2.0.12)*. Version 2.0.12. 2023.

[27] A. M. Dziewonski and D. L. Anderson. “Preliminary Reference Earth Model”. In: *Physics of the Earth and Planetary Interiors* 25 (1981), pp. 297–356.

[28] Author(s) Name. *Title of the Software/Package (version X.Y.Z)*. Zenodo record 14718756, available at https://zenodo.org/records/14718756. 2024.

[29] Daniel Barrow and collaborators. *NuOscillator: A unified framework for neutrino oscillation probability calculations*. Available at https://github.com/dbarrow257/NuOscillator. 2024.

[30] Joshua Barrow and Tyler Stokes. *Exploring Golden Channel Proton Decay in DUNE*. Presentation at Institute for Nuclear Theory Workshop on Baryon Number Violation. DUNE-doc-32628. 2024.

[31] Michael David Baird. “An Analysis of Muon Neutrino Disappearance from the NuMI Beam Using an Optimal Track Fitter”. PhD thesis. Sept. 2015.

[32] G. D. Barr and et al. “Three-dimensional calculation of atmospheric neutrinos”. In: *Phys. Rev. D* 70 (2004), p. 023006.

[33] C. Andreopoulos et al. “The GENIE Neutrino Monte Carlo Generator”. In: *Nucl. Instrum. Meth. A* 614 (2010), pp. 87–104.

[34] S. Agostinelli et al. “GEANT4 - A Simulation Toolkit”. In: *Nucl. Instrum. Meth. A* 506 (2003), pp. 250–303.

[35] et al A.J.Norman. *NOvA DAQ Data Formats - Definitions*. Tech. rep. NOvA Internal Document, DocDB 4390=v16, 2009.

[36] M. Tamsett A.J.Norman. *DDT blessed plots Neutrino*. Tech. rep. NOvA Internal Document, DocDB 11471-v1, 2014.

[37] Y. Ashie et al. “Measurement of the atmospheric neutrino oscillation parameters using neutrino-induced upward stopping muons and upward through-going muons”. In: *Phys. Rev. Lett.* 97 (2006), p. 171801.

[38] Leandro A. F. Fernandes and Manuel M. Oliveira. “Real-time line detection through an improved Hough transform voting scheme”. In: *Pattern Recognition* 41.1 (2008), pp. 299–314.

[39] M. Baird et al. “Event Reconstruction Techniques in NOvA”. In: *Journal of Physics: Conference Series*. Vol. 664. 7. 2015, p. 072035.

[40] J. C. Dunn. “A Fuzzy Relative of the ISODATA Process and Its Use in Detecting Compact Well-Separated Clusters”. In: *Journal of Cybernetics* 3.3 (1973), pp. 32–57.

[41] N. H. Kuiper. “Tests concerning random points on a circle”. In: *Proceedings of the Koninklijke Nederlandse Akademie van Wetenschappen, Series A* 63 (1960), pp. 38–47.

[42] R. E. Kalman. “A New Approach to Linear Filtering and Prediction Problems”. In: *Transactions of the ASME - Journal of Basic Engineering* 82.1 (1960), pp. 35–45.

[43] Joshua Porter. *ReMId 2019 Retraining: Report for the NOvA Experiment*. Internal Report NOvA DocDB 42277. Access restricted; internal to NOvA Collaboration. University of Sussex, Dec. 2019.

[44] S. Navas et al. “Review of Particle Physics”. In: *Phys. Rev. D* 110.3 (2024), p. 030001.

[45] Andrew Thomas Cleve Sutton. “Domain Generalization with Machine Learning in the NOvA Experiment”. PhD thesis. Florida State University, Tallahassee, FL, USA, GRID:grid.255986.5, Virginia U., 2023.

[46] NOvA Collaboration. *3-Flavour Event Selection for Ana2024 Analysis*. Tech. rep. Accessed via NOvA DocDB. NOvA Internal Document, DocDB 61640-v1, 2024.

[47] Nicholas Metropolis et al. “Equation of state calculations by fast computing machines”. In: *The Journal of Chemical Physics* 21.6 (1953), pp. 1087–1092.

[48] G. D. Barr et al. “Uncertainties in Atmospheric Neutrino Fluxes”. In: *Phys. Rev. D* 74 (2006), p. 094009.

[49] M. Honda et al. “Atmospheric neutrino flux calculation using the NRLMSISE-00 atmospheric model”. In: *Phys. Rev. D* 92.2 (2015), p. 023004.

[50] M. Honda. *Atmospheric neutrino flux tables (2014)*. http://www-rccn.icrr.u-tokyo.ac.jp/mhonda/public/nflx2014/. Accessed: 2025-10-02.

[51] M. Honda et al. “Calculation of atmospheric neutrino flux using the interaction model calibrated with atmospheric muon data”. In: *Physical Review D* 75 (2007), p. 043006.

[52] The MaCh3 Collaboration. *mach3-software/MaCh3: v1.3.4 (v1.3.4). Zenodo.* 2025.

[53] Mahdi Taani. “Non-Standard Neutrino Interaction Analysis with Atmospheric Neutrino Data in Super-Kamiokande I-IV and the Design of the Hyper-Kamiokande Outer Detector”. PhD thesis. Nagoya University/The University of Edinburgh, Edinburgh U., 2020.

[54] R. Abbasi et al. “Strong Constraints on Neutrino Nonstandard Interactions from TeV-Scale ν_μ Disappearance at IceCube”. In: *Phys. Rev. Lett.* 129.1 (2022), p. 011804.